

**Anwendung  
der hochauflösenden Laserspektroskopie zur  
Untersuchung der Energieniveaustuktur und  
der Elektron - Phonon - Wechselwirkung im  
lichtsammelnden Komplex II grüner Pflanzen**

DISSERTATION

zur Erlangung des akademischen Grades

doctor rerum naturalium

(Dr. rer. nat.)

im Fach Physik

eingereicht an der

Mathematisch - Naturwissenschaftlichen Fakultät I

der Humboldt - Universität zu Berlin

von

Diplom Physiker Jörg Pieper

geboren am 12. Oktober 1968 in Zossen

Präsident der Humboldt - Universität zu Berlin

Prof. Dr. Jürgen Mlynek

Dekan der Mathematisch - Naturwissenschaftlichen Fakultät I

Prof. Dr. Bernhard Ronacher

Gutachter:      1. Prof. Dr. Joachim Voigt  
                         2. Prof. Dr. Gernot Renger  
                         3. Dr. habil. Volkhard May

Tag der mündlichen Prüfung: 7. Dezember 2000

## Abstract

Spectral hole-burning (HB) is combined with fluorescence line-narrowing (FLN) experiments at 4.2 K and studies of temperature-dependent fluorescence spectra in order to investigate *low-energy level structure* as well as *electron-phonon coupling* of the LHC II antenna complex of green plants. Special attention has been paid to eliminate effects owing to reabsorption of fluorescence and to assure that the FLN spectra are virtually unaffected by hole-burning or scattering artifacts.

For the first time, analysis of the 4.2 K hole spectra reveals three low-energy  $Q_y$ -states at  $(677.1 \pm 0.2)$ ,  $(678.4 \pm 0.2)$  and  $(679.8 \pm 0.2)$  nm, respectively. The inhomogeneous width of their absorption bands is  $(80 \pm 10) \text{ cm}^{-1}$ . It is likely that each of these states is associated with the lowest energy state of one trimer subunit with the energetic separations of  $\sim 30 \text{ cm}^{-1}$  being due to structural heterogeneity. A weak satellite hole structure as well as low pressure shift rates indicate that each of the low-energy states is highly localized on a single Chl *a* molecule of the corresponding trimer subunit. The results are shown to be virtually free from aggregation effects.

The homogeneous width for the lowest state is  $0.073 \text{ cm}^{-1}$  at 4.7 K, which is predominantly due to pure dephasing. Widths of holes burned into the 650 nm absorption band correspond to Chl *b*→Chl *a* energy transfer times of 1 ps and  $\sim 240$  fs at 4.2 K while holewidths for the 676 nm absorption band lead to Chl *a*→Chl *a* energy transfer times in the 6-10 ps range.

The complexities associated with the interpretation of the phonon structure in HB and FLN spectra are discussed by theoretically analyzing the different phonon sideband contributions. On this basis, 4.2 K HB and FLN data can be consistently interpreted for the first time by weak electron-phonon coupling with a Huang-Rhys factor of  $\sim 0.9$  to protein phonons with a broad and strongly asymmetric one-phonon profile having a peak frequency of  $15 \text{ cm}^{-1}$  and a width of  $105 \text{ cm}^{-1}$ .

## Abstrakt

Hole-Burning (HB) und Fluorescence Line-Narrowing (FLN) bei 4.2 K sowie Experimente zur Temperaturabhängigkeit werden angewendet, um *Energieniveaustruktur* und *Elektron-Phonon-Wechselwirkung* im Antennenkomplex LHC II grüner Pflanzen zu untersuchen. Besondere Aufmerksamkeit gilt dabei der Vermeidung systematischer Meßfehler durch Reabsorption von Fluoreszenz oder durch Lichtstreuung und unerwünschtes Lochbrennen bei FLN-Experimenten.

Durch die Auswertung von Lochspektren können erstmals drei niederenergetische  $Q_y$ -Zustände bei  $(677.1 \pm 0.2)$ ,  $(678.4 \pm 0.2)$  und  $(679.8 \pm 0.2)$  nm nachgewiesen werden. Die inhomogene Breite der zugehörigen Absorptionsbanden beträgt  $(80 \pm 10) \text{ cm}^{-1}$ . Wahrscheinlich stellt jeder dieser Zustände das tiefste Energieniveau einer Untereinheit des LHC II-Trimers dar. Die energetische Differenz zwischen den drei Zuständen von je etwa  $30 \text{ cm}^{-1}$  kann durch strukturelle Heterogenität erklärt werden. Sowohl die schwache Resonanzstruktur als auch die Ergebnisse von Hochdruckexperimenten weisen darauf hin, daß die drei Zustände weitgehend an jeweils einem Chl *a*-Molekül einer Untereinheit des LHC II-Trimers lokalisiert sind. Es kann nachgewiesen werden, daß die Meßergebnisse praktisch frei von Effekten durch unerwünschte Aggregation sind.

Die homogene Linienbreite des energetisch tiefsten Zustandes beträgt  $0.073 \text{ cm}^{-1}$  bei 4.7 K und wird im Wesentlichen durch phasenerstörende Prozesse (pure dephasing) bestimmt. Die Lochbreiten innerhalb der 650 nm Absorptionsbande entsprechen Chl *b*→Chl *a* Energietransferzeiten von 1 ps und  $\sim 240$  fs bei 4.2 K, während Lochbreiten innerhalb der 676 nm Absorptionsbande Chl *a*→Chl *a* Energietransferzeiten in der Größenordnung von 6-10 ps ergeben.

In einer theoretischen Betrachtung werden die Beiträge zu Phonon-Seitenbanden bei HB und FLN separat analysiert. Auf dieser Grundlage können Ergebnisse von HB und FLN Experimenten an LHC II erstmals in einem konsistenten Modell durch schwache Elektron-Phonon-Wechselwirkung mit einem Huang-Rhys-Faktor von 0.9 und ein asymmetrisches Ein-Phonon-Profil mit einem Maximum bei  $15 \text{ cm}^{-1}$  und einer Breite von  $105 \text{ cm}^{-1}$  erklärt werden.

# Contents

<b>1 INTRODUCTION</b>	<b>7</b>
<b>1.1 The Light-Harvesting Complex II</b>	<b>9</b>
<b>1.2 Spectroscopic Properties of LHC II</b>	<b>13</b>
<b>2 LINE-NARROWING SPECTROSCOPIES</b>	<b>22</b>
<b>2.1 Inhomogeneous Broadening</b>	<b>22</b>
<b>2.2 Hole-Burning Spectroscopy</b>	<b>26</b>
2.2.1 Hole-Burning Mechanisms	26
2.2.2 Nonphotochemical Hole-Burning	27
<b>2.3 Fluorescence Line-Narrowing</b>	<b>29</b>
<b>2.4 Theoretical Background</b>	<b>30</b>
2.4.1 Basic Principles	31
2.4.2 Homogeneously Broadened Spectra	34
2.4.3 Non-Line-Narrowed Spectra	38
2.4.4 Line-Narrowed Spectra	40
2.4.5 Calculation Programs	49
<b>2.5 Selected Applications</b>	<b>50</b>
<b>3 MATERIALS AND EXPERIMENTAL METHODS</b>	<b>54</b>
<b>3.1 Sample Preparation</b>	<b>54</b>
3.1.1 Trimeric LHC II	54
3.1.2 Aggregated LHC II	55
3.1.3 CP29	55
<b>3.2 Experimental Methods and Instrumentation</b>	<b>56</b>
3.2.1 Spectral Hole-Burning	56
3.2.1.1 Hole-Burning Experiments	57
3.2.1.2 Fluorescence Excitation Mode	58
3.2.1.3 High-Pressure Apparatus	60
3.2.2 Fluorescence Experiments	61
3.2.2.1 Non-Line-Narrowed Fluorescence Spectra	63
3.2.2.2 Line-Narrowed Fluorescence Spectra	63
<b>4 EXPERIMENTAL RESULTS</b>	<b>64</b>
<b>4.1 Hole-Burned Spectra of LHC II</b>	<b>64</b>

4.1.1 Hole-Burning with Burn Wavelengths Lower than 674 nm	65
4.1.2 Constant Fluence Hole-Burning in the Low-Energy Region	65
4.1.3 Compatibility of the Low-Energy Hole Features	67
4.1.4 Phonon Sideband Holes	71
<b>4.2 Effects upon Aggregation of LHC II</b>	<b>72</b>
<b>4.3 Hole-Burned Spectra of CP29</b>	<b>76</b>
4.3.1 Hole-Burning with Burn Wavelengths Lower than 674.5 nm	76
4.3.2 Constant Fluence Hole-Burning in the Low-Energy Region	79
<b>4.4 Pressure-Dependent Spectra of LHC II</b>	<b>81</b>
<b>4.5 Fluorescence Spectra of LHC II</b>	<b>84</b>
4.5.1 The 4.2 K Fluorescence Spectrum	84
4.5.2 Effects Owing to Reabsorption	85
4.5.3 Temperature-Dependent Fluorescence Spectra	86
<b>4.6 Line-Narrowed Fluorescence Spectra of LHC II</b>	<b>86</b>
4.6.1 Artifacts Owing to Light Scattering	87
4.6.2 Effects Owing to Hole-Burning	87
4.6.3 Effects Owing to Reabsorption	88
4.6.4 Excitation Wavelength Dependence	90
<b>5 LOW-ENERGY LEVEL STRUCTURE OF LHC II</b>	<b>92</b>
5.1 Assignment of the Lowest $Q_y$ -State	92
5.2 Nature of the Low-Energy States	93
5.3 Pigment-Pigment Coupling Strengths	95
<b>6 EXCITATION ENERGY TRANSFER IN LHC II</b>	<b>99</b>
6.1 Chl b-Chl a Excitation Energy Transfer	99
6.2 Chl a-Chl a Excitation Energy Transfer	100
6.3 Pure Dephasing	101
<b>7 ELECTRON-PHONON COUPLING IN LHC II</b>	<b>103</b>
7.1 Analysis of Line-Narrowed Spectra	103
7.1.1 Analysis of Phonon Structure in Line-Narrowed Spectra	104
7.1.2 Calculated Line-Narrowed Spectra	109
7.1.3 The One-Phonon Profile	115
7.2 Temperature-Dependent Spectra	117
7.3 Effects at Temperatures above 120 K	120

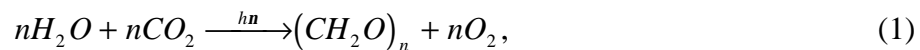
<b>8 CONCLUDING REMARKS</b>	<b>123</b>
8.1 Low-Energy Level Structure of LHC II	123
8.2 Excitation Energy Transfer in LHC II	124
8.3 Electron-Phonon Coupling in LHC II	124
<b>9 ZUSAMMENFASSUNG</b>	<b>127</b>
9.1 Energieniveaustuktur von LHC II	127
9.2 Energietransfer in LHC II	128
9.3 Elektron-Phonon-Wechselwirkung im LHC II	129

## Abbreviations

Chl	chlorophyll
CP29	chlorophyll-protein-complex having a molecular mass of 29 kDa (Chl <i>a/b</i> -binding antenna complex of green plants)
EET	excitation energy transfer
FLN	fluorescence line-narrowing
FWHM	full width at half maximum
HB	hole-burning
IDF	inhomogeneous distribution function
LHC II	light-harvesting complex of Photosystem II (Chl <i>a/b</i> -binding antenna complex of green plants)
NPHB	nonphotochemical hole-burning
PS II	Photosystem II
PSB	phonon sideband
PSBH	phonon sideband hole
TLS	two-level system
ZPH	zero-phonon hole
ZPL	zero-phonon line

# 1 Introduction

Photosynthesis is one of the most important physiological processes in nature. It enables photoautotrophic organisms like green plants, algae and cyanobacteria to transform light energy into storable chemical energy. In most general form, this photochemical process can be described by the equation



which represents the light-induced cleavage of water and fixation of carbon by formation of a carbohydrate  $(CH_2O)_n$  and free dioxygen  $O_2$ . The photosynthetic apparatus of green plants is located in separate cell organelles, the chloroplasts, and comprises highly specialized pigment-protein complexes incorporated into a lipid bilayer membrane, the thylakoid membrane (see e.g. G. Renger, 1992; K.-D. Irrgang, 1999).

According to their function, photosynthetic pigment-protein complexes can be classified as antennae or reaction centers. This functional subdivision has first been discovered by Emerson and Arnold (1932). They found that only one oxygen molecule is evolved per 2500 pigment molecules when exposing *Chlorella* cells to repetitive light flashes of about 10  $\mu$ s duration. Thus, only a small fraction out of the total number of pigments can be directly involved in photochemical processes. Rather, a number of antenna complexes surrounds each reaction center in order to enhance the optical cross section of the photosynthetic apparatus both, spectrally and spatially. Light absorption by antenna pigments results in the creation of an excited state, which is subsequently transferred to the photochemically active pigments in the reaction center. The latter process is called excitation energy transfer (EET) and may occur on timescales of less than a picosecond as was found for several antenna complexes (for a review see e.g. van Grondelle et al., 1994). In the reaction center the excitation drives the primary charge separation, which initiates a multistep reaction that leads to fixation of energy in organic compounds and the release of oxygen, *vide supra*. Moreover, photosynthetic EET is highly efficient. Up to 98 % of the absorbed photons induce a charge separation in the reaction center (Bassi et al., 1990). Both attributes, its

ultrafast dynamics as well as its high efficiency, have raised strong scientific interest in light-harvesting and EET in photosynthetic antenna complexes.

The major pigment molecule in oxygenic photosynthesis is the chlorophyll (Chl). In green plants Chl occurs in two different forms, Chl *a* and *b*, which differ in only one sidechain. Chl is a tetrapyrrol which is characterized by an extended, conjugated  $\pi$ -electron system, which mainly determines its optical properties. The absorption spectrum of Chl monomers in solution exhibits intense bands in the red ( $S_1$ -band) and blue ( $S_2$ - or Soret-band) due to strongly allowed  $\pi\pi^*$ -transitions (see e.g. G. Renger, 1999 and references therein). Other pigments include several types of carotenoids, such as  $\beta$ -carotene, lutein, violaxanthin, and neoxanthin. In photosynthetic antenna complexes pigments are bound to proteins by ligation or hydrogen bonding. Thus, the protein backbone determines the distance between and mutual orientation of pigment molecules which are relevant to the strength of the pigment-pigment interactions. In addition, the particular protein environment affects the transition frequency of a pigment molecule while the inherent structural heterogeneity of the protein leads to inhomogeneous broadening. Thus, complex pigment-pigment as well as pigment-protein interactions can be expected to govern the spectral shape of the absorption spectra of photosynthetic pigment-protein complexes.

Furthermore, the coupling of the purely electronic transition of a pigment to delocalized vibrations of the protein environment (phonons), also known as electron-phonon coupling, is of particular relevance for light-harvesting and EET in antenna complexes. The simultaneous creation or annihilation of a phonon during an optical transition permits the absorption of light quanta that do not match the transition frequency of a given pigment and, therefore, leads to a considerable increase of the spectral absorption cross section of a single pigment (see e.g. Rebane, 1970). Furthermore, interaction with phonons may induce relaxation of the excited states of an antenna complex and, thus, plays an important role in dissipation of excess energy during EET (see e.g. Kühn et al., 1998).

In the following chapters, the difficulties associated with the search for a

detailed understanding of the structure-function relationship for photosynthetic pigment-protein complexes are discussed in more detail for the light-harvesting complex of Photosystem II of green plants (LHC II). Chapter 1.1 focuses on the organization of the antenna system of Photosystem II and the present knowledge on the microscopic structure of LHC II, while Chapter 1.2 deals with the spectroscopic properties of LHC II as investigated by previous experimental and theoretical studies.

### ***1.1 The Light-Harvesting Complex II***

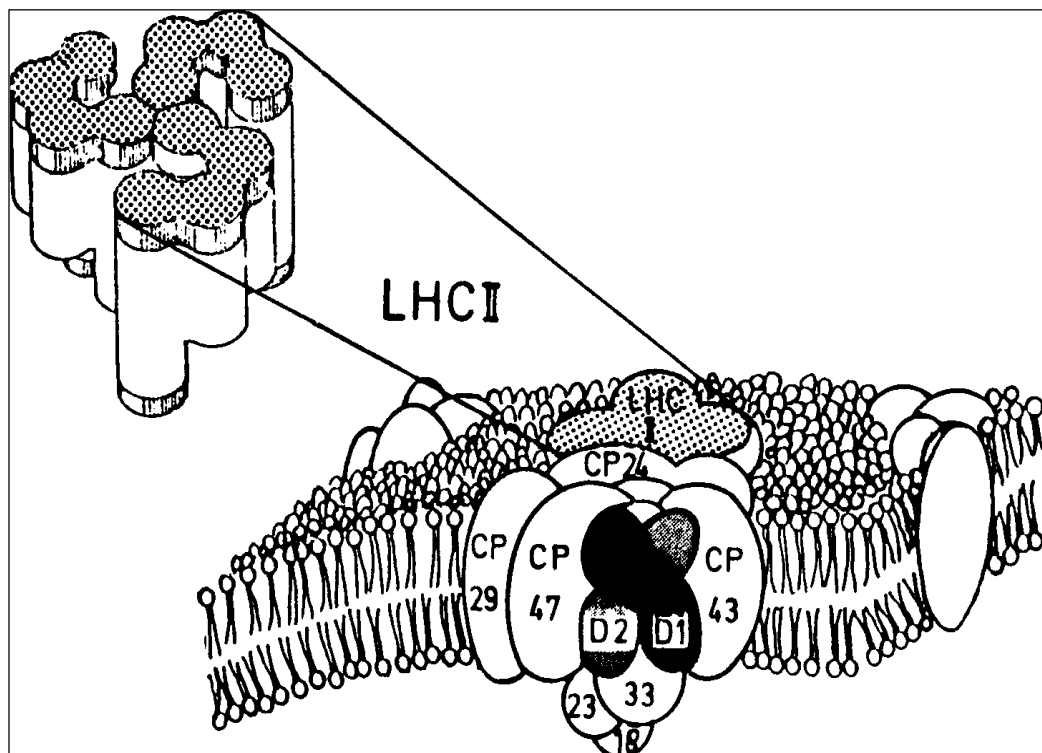


*Figure 1. Incorporation of antenna complexes LHC II, CP29, CP24, CP43, and CP47 into the thylakoid membrane of green plants according to G. Renger (1992). The PSII reaction center (D1-D2-heterodimer) is shown in black and gray. A magnification shows the trimeric organization of LHC II.*

The antenna system of Photosystem II (PS II) of green plants consists of a core antenna located close to the reaction center complex and the peripherally situated light-harvesting complex II (LHC II). The core antenna comprises two Chl *a* binding pigment-protein complexes, which are referred to as CP47 and CP43, respectively. In contrast to this, LHC II binds Chl *a*, Chl *b* and various xanthophylls (see e.g. Jansson, 1994; Paulsen, 1995). The latter light-

harvesting complex includes at least six different Chl *a/b* binding pigment-protein complexes denoted as Lhcb 1-6. Lhcb 1-3 constitute the major light-harvesting complex LHC II, while Lhcb4-6 are designated as minor antenna complexes. The latter are also known as CP24, CP26, and CP29, respectively, *vide infra*. The overall organization of PS II is shown in Fig. 1.

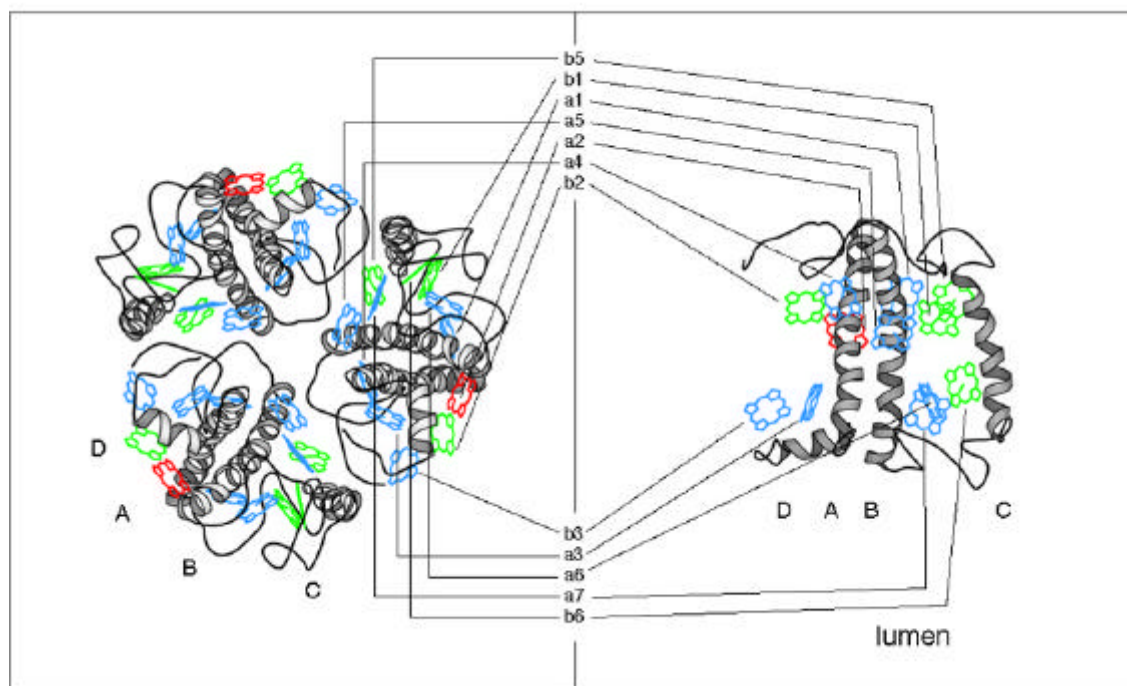


Figure 2. Schematic view of the LHC II structure according to Rogl and Kühlbrandt (1999). The left frame shows the LHC II trimer viewed from the luminal side. The right frame depicts the LHC II monomer. The Chl molecules and  $\alpha$ -helices are labeled according to Kühlbrandt et al. (1994). Chl *a* and *b* molecules are given in blue and green color, respectively. Chl *a2* is shown in red.

The major light-harvesting complex LHC II is the most abundant antenna complex of green plants, which binds approximately 65 % of the chlorophyll associated with PS II. Its structure has been analyzed by electron crystallography to a resolution of 3.4 Å (Kühlbrandt et al., 1994). The LHC II protein crystallizes as a trimer of subunits, each of which contains 12 - 13 Chl molecules arranged in two layers close to the upper and lower surfaces of the thylakoid membrane and two carotenoid molecules. The planes of the porphyrin rings are oriented almost perpendicularly to the plane of the thylakoid membrane. Within each of the two layers the shortest center to center distances between the Chl molecules are in the range of ~9-14 Å. The pigments appear to be symmetry inequivalent. Three membrane spanning  $\alpha$ -

helices and a fourth amphipathic helix located at the luminal side form the protein backbone. The pigments are non-covalently bound to the protein by amino acid side chains or hydrogen bonding. Fig. 2 shows the LHC II trimer viewed from the luminal membrane surface (left side) and a cross section view of a monomeric LHC II subunit (right side).

The structural resolution of 3.4 Å does not permit a distinction between Chl *a* and *b* molecules. However, a preliminary assignment of the seven Chl *a* molecules was based on the physiological criterion of efficient triplet state quenching of Chl *a* molecules by the carotenoid molecules of the subunit (Kühlbrandt et al., 1994). Briefly, Chl triplets are formed by intersystem crossing (spin inversion) from the first excited Chl singlet state and have lifetimes in the ms-range because relaxation into the singlet ground state is spin-forbidden. A reaction of Chl and oxygen in their triplet states forms the highly reactive singlet oxygen, which is a lethal poison to the cell. Oxygen, however, is produced by water cleavage in the PS II reaction center adjacent to LHC II. Thus, an efficient Chl triplet state quenching is important in order to prevent the creation of singlet oxygen and subsequent cell death. The necessary singlet-triplet transition is provided by an electron exchange mechanism between Chl and carotenoid molecules, which requires an overlap of the corresponding wavefunctions and, therefore, small intermolecular distances. Furthermore, Chl triplet state quenching is more important for Chl *a* because excitation energy is transferred from Chl *b* to Chl *a* within less than a few picoseconds, i.e. before triplet states are formed, while it remains at Chl *a* for about 4 ns at room temperature (see also Chapter 1.2). Thus, the seven Chls adjacent to the carotenoids were assigned as Chl *a* while the remaining five were identified as Chl *b*. In Fig. 2 Chl molecules are labeled accordingly. With this assignment, the center to center distances for five pairs of Chl *a* and Chl *b* molecules fall in the range of 8.3-10.5 Å, while the shortest Chl *a*-Chl *a* and Chl *b*-Chl *b* distances are ~ 11 Å.

The assignment of certain Chl molecules by Kühlbrandt et al. (1994) has recently been questioned by theoretical simulations of time-domain experiments. In their calculations, Trinkunas et al. (1977) replaced Chl *a*1 and

*a2* by Chl *b* and Chl *b1* and *b2* by Chl *a*. Gradinaru et al. (1998) proposed to exchange Chl *a6* and *b5*. Nevertheless, the identities of five Chl molecules (Chl *a1*, *a2*, *a3*, *b5*, and *b6*) could be confirmed by spectroscopic studies of LHC II-mutants lacking single pigments while Chl *b3* was found to be a Chl *a*. Moreover, the lowest (fluorescent) state was attributed to Chl *a2* (Rogl and Kühlbrandt, 1999).

The minor Chl *a/b* binding pigment-protein complexes, also referred to as CP29, CP26, and CP24, respectively, account for approximately 15 % of the Chl molecules of PS II (Jansson, 1994). The amino acid sequence of the latter complexes shows substantial homology to that of Lhcb1-3. Thus, they are predicted to form similar secondary structure elements as those of the major LHC II. In contrast to the trimeric LHC II, however, they occur in monomeric form (see e.g. Jansson, 1994; Paulsen, 1995; Bassi et al., 1996). Furthermore, the pigment compositions and stoichiometries of the Lhcb1-6 proteins differ significantly. The largest of the minor Chl *a/b* binding pigment protein complexes, CP29, has been shown to bind 6 Chl *a*, 2 Chl *b* and two to three carotenoid molecules (see e.g. Giuffra et al., 1997; Pascal et al., 1999). Despite the lack of direct information, a structural model for CP29 has been proposed (Bassi et al., 1996). It is based on the high sequence homology among the Lhcb1-6 proteins and the finding that most of the Chls present in CP29 adopt binding sites similar to those in LHC II (Jansson, 1994; Paulsen, 1995; Bassi et al., 1996). The protein backbone of CP29 is also expected to be similar to that of LHC II with three membrane spanning  $\alpha$ -helices and a fourth amphipathic helix. It has been proposed that the minor pigment-protein complexes are involved in light-harvesting and in EET from the peripherally located trimeric LHC II to the reaction center complex (see e.g. Jansson, 1994; Bassi et al., 1996) but also in the so-called quenching processes that protect the reaction center from excess excitation energy (Ruban et al., 1996).

## 1.2 Spectroscopic Properties of LHC II

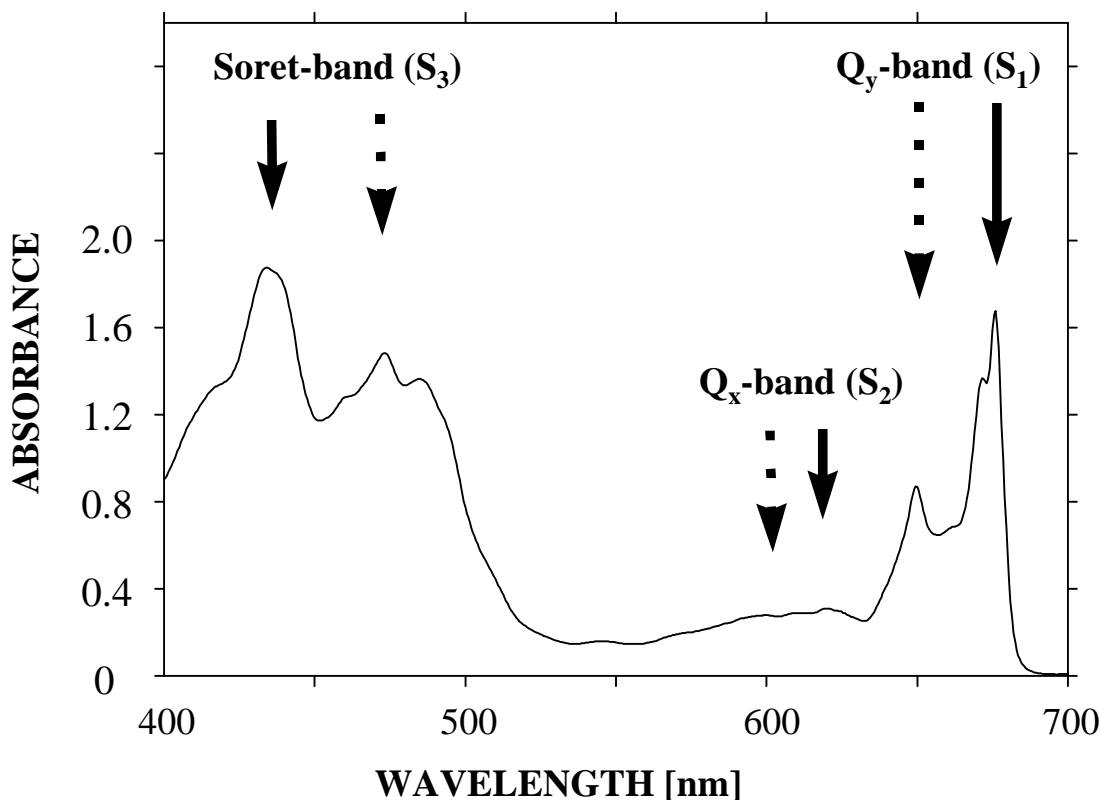


Figure 3. Low-temperature (4.2 K) absorption spectrum of trimeric LHC II. Full and broken arrows label the approximate positions of the Q<sub>y</sub>, Q<sub>x</sub>, and Soret-bands of Chl a and b, respectively. Carotenoids contribute to the absorption between 400 and 500 nm (not shown).

The availability of a structural model for trimeric LHC II prompted a variety of spectroscopic studies in the frequency as well as in the time domain, *vide infra*. Furthermore, the purification (isolation) procedure is highly developed (see Irrgang et al., 1988 and Chapter 3.1). Thus, trimeric LHC II is one of the best studied photosynthetic pigment-protein complexes. Nevertheless, a number of questions regarding its excited state energy level structure and EET still remain unanswered. Especially, the complexity of LHC II's microscopic structure including the inherent heterogeneity of the protein (see Chapter 2.1) as well as the uncertainty in identity and dipole moment orientation of the Chl molecules (see Chapter 1.1) has so far hindered the search for a consistent understanding of the relation between structural organization and light-harvesting function of LHC II.

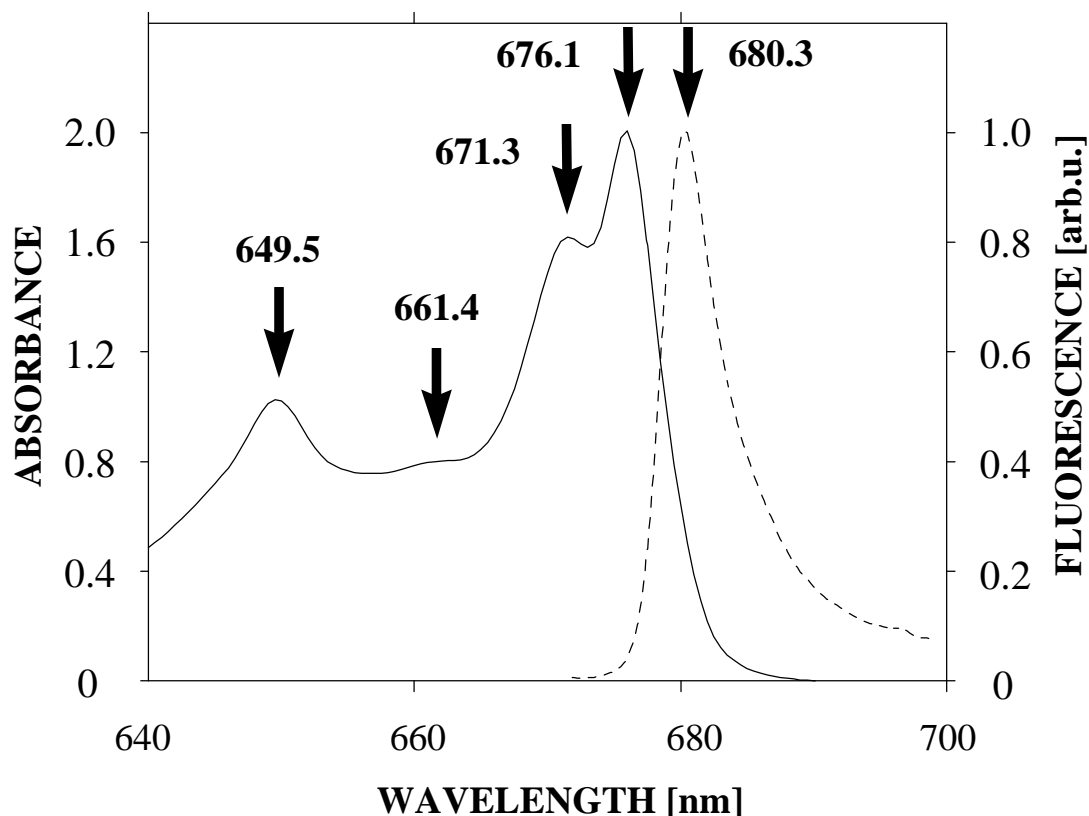


Figure 4. Low-temperature (4.2 K)  $Q_y$ -absorption and fluorescence spectra of trimeric LHC II obtained under non-line-narrowing conditions. Arrows label the positions of discernible bands.

The 4.2 K-absorption spectrum of the trimeric LHC II is shown in Fig. 3. At the first glance, the main absorption bands labeled by arrows basically reflect the  $Q_y$ - ( $S_1$ ),  $Q_x$ - ( $S_2$ ), and Soret- ( $S_3$ ) bands of Chl *a* and *b* monomers in solution as reported by Lichtenthaler (1987). Carotenoids contribute to the absorption in the 400 - 500 nm region (Siefermann-Harms, 1987), while their main function is efficient Chl triplet state quenching (see Chapter 1.1). A closer inspection of the 4.2 K  $Q_y$ -absorption spectrum of trimeric LHC II (see Fig. 4) reveals that it covers a wavelength range of several tens of nm, though it is contributed to by only two types of chromophores, i.e. Chl *a* and *b*. Four absorption bands are discernible in the  $Q_y$ -region, which are labeled by full arrows in Fig. 4 pointing to a complex  $Q_y$ -energy level structure. Based on the absorption spectra of Chl *a* and *b* monomers in solution, there is general agreement that the absorptions at 650 nm and ~ 670-680 nm are mainly due to Chl *b* and *a*, respectively.

The simple observations discussed above establish that the  $Q_y$ -absorption

spectrum of LHC II is not a simple superposition of those of its 12-13 Chl molecules. In view of the complex microscopic structure, pigment-pigment-, pigment-protein-, as well as pigment-vibration- interactions can be expected to affect spectral position and shape of the absorption spectrum of a certain pigment in LHC II:

*Chl-Chl interaction:* A pigment molecule in its excited state can be viewed as an oscillating dipole. This oscillation may represent a perturbation to a second, neighboring molecule in its ground state. Because of this perturbation, there is a probability that the second molecule becomes excited while the first returns into its ground state. Thus, an excitation may be localized at different pigment molecules during its lifetime. Such an excitation is called *exciton* (for a detailed discussion see Pearlstein, 1991). Briefly, the strength of the pigment-pigment-interaction depends on the mutual orientation of the dipole moments and the center-to-center distances of the interacting pigments. Excitonic interaction may split or shift the absorption frequencies and redistribute the oscillator strengths of the interacting pigments (see e.g. T. Renger, 1995, 1996, 2000). Regardless of the actual degree of delocalization of the corresponding wavefunctions, the resulting excitonic energy levels have to be viewed as energetic levels of the system of interacting pigments.

*Chl-protein interaction:* In LHC II the pigments are bound to the protein by ligation or hydrogen bonding. Bonding interactions as well as Coulombic interactions of a certain pigment with its specific, polarizable protein environment may represent a perturbation of the purely electronic transition and, therefore, lead to a shift of the absorption frequency of a pigment at a certain binding site. Furthermore, the inherent heterogeneity of the protein environment can lead to inhomogeneous broadening, i.e. a distribution of transition frequencies can be observed for pigments at a certain binding site in an ensemble of pigment-protein complexes (see Chapter 2.1).

*Chl-vibration interaction:* The purely electronic transitions of a pigment are coupled to a distribution of protein phonons as well as to localized, intramolecular vibrations of the Chl molecule itself. In contrast to the localized vibrations of the pigment molecule with pronounced modes between ~ 700 and

$\sim 1700\text{ cm}^{-1}$  (see e.g. Avarmaa and Rebane, 1985), the delocalized, low-frequency protein phonons form a quasi-continuum in the frequency range  $< 200\text{ cm}^{-1}$  (Hayes et al., 1988a). Thus, the absorption line corresponding to the electronic transition is accompanied by a broad phonon wing and vibrational satellites reflecting additional creation/ annihilation of vibrational quanta during an electronic transition. Briefly, electron-phonon coupling is characterized by the coupling strength or Huang-Rhys factor  $S$  and the density of states of the protein phonons as will be discussed in more detail in Chapter 2.4.

The first detailed investigation of the  $Q_y$ -energy level structure of trimeric LHC II was based on 77 K absorption, linear dichroism and circular dichroism spectra (Hemelrijk et al., 1991). Nine  $Q_y$ -states were assigned in the region between  $\sim 650$  and  $676\text{ nm}$ . The results indicated the existence of significant and complex excitonic couplings. The lowest energy state was assigned at  $676\text{ nm}$ , the position of the most intense absorption band. The presence of an additional, relatively weak transition at  $\sim 680\text{ nm}$  was reported based on hole-burning spectroscopy at  $4.2\text{ K}$  (Reddy et al., 1994) and pump-probe experiments at room temperature (Schrötter et al., 1994; Kehrberg et al., 1995). In the hole-burning study, the  $680\text{ nm}$ -state was found to be characterized by weak coupling to protein phonons with a mean frequency of  $\omega_m = 20\text{ cm}^{-1}$  and a Huang-Rhys factor of  $S = \sim 0.4-0.5$ . With the lowest energy state at  $680\text{ nm}$  and an optical reorganization energy of  $S\omega_m = 8\text{ cm}^{-1}$ , the  $6\text{ nm}$  red shift of the fluorescence origin band relative to the  $676\text{ nm}$  absorption band was reasonably well accounted for. Subsequently, reabsorption studies (Voigt et al., 1996) as well as fluorescence line-narrowing and temperature-dependent absorption spectroscopies (Peterman et al., 1997) confirmed the existence of a  $680\text{ nm}$  state whose absorption is not resolved from that of the  $676\text{ nm}$  band in Fig. 4. The results of femtosecond transient absorption measurements at  $12\text{ K}$  (Bittner et al., 1995) and  $77\text{ K}$  (Visser et al., 1996) are consistent with the existence of a  $680\text{ nm}$  state.

As to the electron-phonon coupling in trimeric LHC II, results of  $4.2\text{ K}$  hole-burning (Reddy et al., 1994) and fluorescence line-narrowing (Peterman et al.,

1997) experiments have already been reported. The hole-burning study found that the lowest  $Q_y$ -state of this complex is characterized by a somewhat asymmetric one-phonon profile with a mean phonon frequency of  $\omega_m = 20 \text{ cm}^{-1}$ , a width of  $\sim 25 \text{ cm}^{-1}$  and  $S = 0.4$ . Inspection of the line-narrowed fluorescence spectra yielded  $\omega_m = 22 \text{ cm}^{-1}$  and a strongly asymmetric one-phonon profile with a width of  $\sim 65 \text{ cm}^{-1}$ . Because the zero-phonon line was severely contaminated with scattered laser light in the line-narrowed fluorescence spectra, an  $S$  factor of  $\sim 0.6$  was determined by fitting the low-energy wing of temperature-dependent absorption spectra of LHC II using the latter one-phonon profile and assuming that the lowest state is located at 676 nm. Weak electron-phonon coupling with  $S < 1$  and  $\omega_m$  values of 20 - 30  $\text{cm}^{-1}$  are typically observed for photosynthetic antenna complexes (Reddy et al., 1992). Nevertheless, the shapes of the one-phonon profile reported from the above studies differ significantly.

EET in trimeric LHC II is often investigated by time-resolved pump-probe (Savikhin et al., 1994; Bittner et al., 1994; Connelly et al., 1997) or fluorescence upconversion techniques (Du et al., 1994). As discussed by Connelly et al. (1997), Chl  $b \rightarrow$  Chl  $a$  EET occurs with kinetic components of  $\sim 150$  fs, 600 fs and 10 ps at room temperature. Results obtained for monomeric LHC II indicate that these EET processes take place within each subunit of the LHC II trimer (Kleima et al., 1997), which is consistent with the large distances and, therefore, relatively weak interaction energies between Chl molecules belonging to different subunits (Voigt et al., 1996). Based on similar experiments at 77 (Visser et al., 1996) and 12 K (Bittner et al., 1995), it can be concluded that the time constants reported above are weakly temperature-dependent. Of particular interest to this study are the low-temperature (12 K) Chl  $b \rightarrow$  Chl  $a$  EET times of  $\sim 310$  fs and  $\sim 1$  ps (Bittner et al., 1995). Excitation energy transfer/ equilibration associated with states that contribute to the 670 and 676 nm absorption band occurs on a timescale of  $\sim 10$ -20 ps at 12 K (Savikhin et al., 1994). These kinetics are also weakly dependent on temperature.

A detailed understanding of the EET processes and  $Q_y$ -energy level structure

requires an accurate theoretical model based on the complex microscopic structure of trimeric LHC II. Despite of the lack of information about the identity of Chl *a* and *b* molecules as well as about the directions of their  $Q_y$ -transition dipoles, valuable insights can be gathered simulating time and frequency domain spectroscopic data under the constraints imposed by the current 3.4 Å resolution structure. Recent simulations of time-resolved pump-probe experiments assume that the LHC II  $Q_y$ -states can be viewed as being localized on individual Chl molecules (Bittner et al., 1994; Visser et al., 1996; Trinkunas et al., 1997). Within this picture, EET is understood as incoherent hopping of an excitation from molecule to molecule, which is governed by their mutual distance as well as by the spectral overlap of the respective fluorescence and absorption spectra (see e.g. Förster, 1948). An interpretation of non-linear fluorescence and transmission experiments favored a model of delocalized  $Q_y$ -states (see e.g. Schödel et al., 1996), i.e. EET was viewed as spectral relaxation within the common energy level system of strongly interacting pigments. Du et al. (1994) concluded that their data are consistent with both, Förster- as well as excitonic types of EET. Based on the 3.4 Å resolution structure and preliminary assignment of Chl *a* and *b* molecules (see Chapter 1.1) of Kühlbrandt et al. (1994), the first detailed theoretical calculations of the  $Q_y$ -level structure of LHC II within the density matrix formalism (T. Renger, 1995, 1996) revealed coupling strengths of up to  $\sim 150 \text{ cm}^{-1}$  for neighboring Chl *a* and *b* molecules. On the other hand, Chl *a*-Chl *a* and Chl *b*-Chl *b* interactions appeared to be considerably weaker. Because a coupling strength of  $150 \text{ cm}^{-1}$  is small relative to a Chl *b*-Chl *a* energy gap of  $\sim 600 \text{ cm}^{-1}$ , it was found that excitonic interactions between Chl molecules have a small effect on the  $Q_y$ -energy levels although they result in a significant redistribution of oscillator strengths. Thus, pigment-protein interactions seemed to be more important than excitonic interactions in determination of the  $Q_y$ -energy levels.

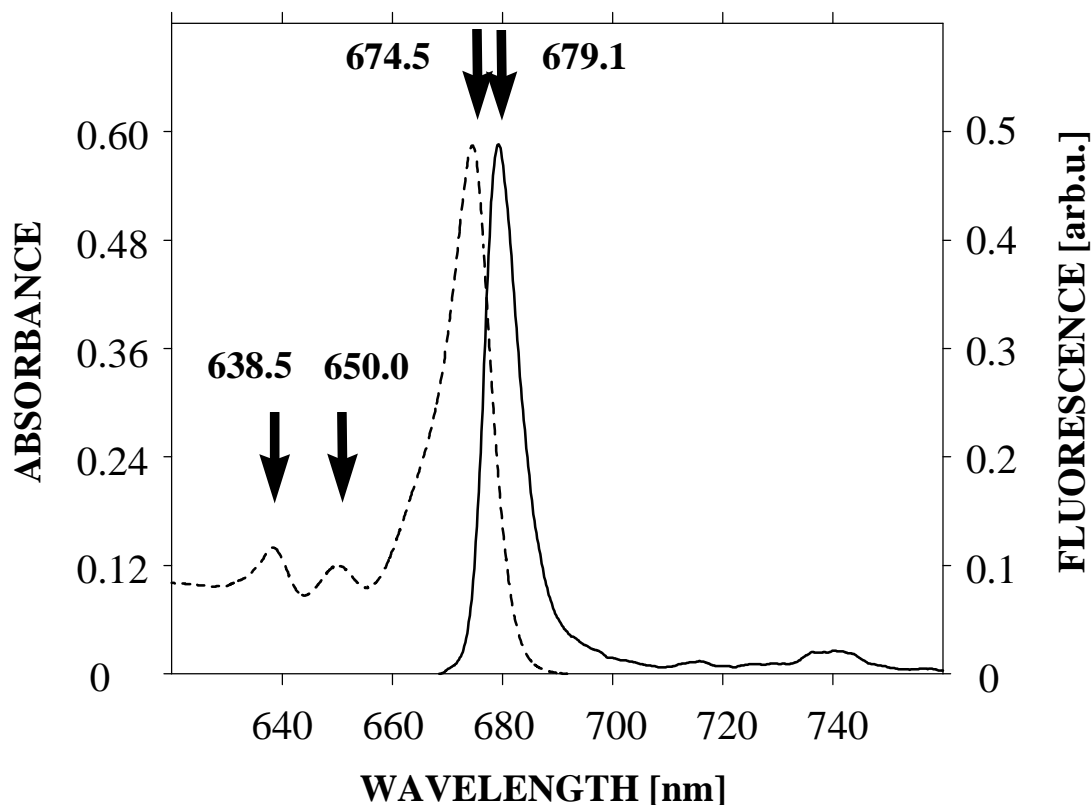


Figure 5. Low-temperature (4.2 K)  $Q_y$ -absorption and fluorescence spectra of CP29 obtained under non-line-narrowing conditions. Arrows label the positions of discernible bands.

Because of the smaller number of pigments as well as its monomeric form, the CP29 antenna of green plants is less complex than trimeric LHC II. In view of the similar secondary structure, experimental data obtained for CP29 may be of interest in interpretation of results gathered for the more complicated LHC II. CP29 has already been studied by absorption, and fluorescence spectroscopies as well as LD and CD spectroscopies (see e.g. Zucchelli et al., 1994; Pascal et al., 1999). The low-temperature  $Q_y$ -absorption spectrum shows two Chl *b* bands at 638 and 650 nm and a relatively broad band peaking at 674 nm in the Chl *a* region (see Fig. 5). Temperature-dependent absorption, LD and CD spectra of CP29 show similarities with those of the trimeric LHC II complex. Spectral features associated with the 670 nm-band of LHC II, however, are missing in the CP29 spectra. Time-resolved pump-probe spectroscopy of CP29 at 77 K (Gradinaru et al., 1998) revealed that excitation energy is transferred from Chl *b* absorbing at 638 nm to Chl *a* absorbing at ~676 nm in about 350 fs. EET from Chl *b* absorbing at 650 nm to Chl *a* absorbing at ~670 nm occurs in about 2.2 ps. In addition, fast 280 fs and

slower 10-13 ps time constants were found for equilibration among the Chl a molecules.

The scope of the present study is a detailed investigation of low-energy  $Q_y$ -level structure and electron-phonon coupling of the trimeric LHC II antenna complex of green plants by line-narrowing spectroscopies such as spectral hole-burning and fluorescence line-narrowing. In this regard, Chapter 2 provides a basic overview about line-narrowing spectroscopies as an experimental tool for studies of inhomogeneously broadened optical spectra of pigment-protein systems. The sample material as well as experimental methods and instrumentation are described in Chapter 3. Experimental results are reported in Chapter 4 including a detailed discussion of data quality and possible systematic errors. Finally, the experimental results are discussed in terms of low-energy  $Q_y$ -level structure (Chapter 5), excitation energy transfer dynamics (Chapter 6) as well as electron-phonon coupling (Chapter 7) in LHC II.

In summary, persistent nonphotochemical hole-burning experiments at low temperatures are used to *identify and characterize the low-energy  $Q_y$ -states of LHC II* in the near vicinity of 680 nm. These experiments are more detailed and of higher resolution than those of Reddy et al. (1994). In addition, it will be shown that the results are virtually free from effects owing to aggregation. Comparative hole-burning studies for the structurally similar but less complex, monomeric CP29 antenna system of green plants provide further insight into the nature of the low-energy  $Q_y$ -states of LHC II. The first high-pressure absorption and hole-burning results for trimeric LHC II are presented and used to characterize the strength of Chl-Chl interactions.

The optical dynamics of the low-energy  $Q_y$ -states as well as the EET dynamics of states associated with the 650 and 676 nm bands are discussed by comparison of hole-burning data with those of the time-resolved studies by Bittner et al. (1995) and Savikhin et al. (1994).

Spectral hole-burning is combined with fluorescence line-narrowing experiments at low temperatures in order to investigate the *electron-phonon coupling of the lowest energy state of LHC II* and, especially, to identify the

one-phonon profile, which characterizes the spectral density of the protein phonons. The complexities associated with interpretation of the phonon structure in hole-burned and line-narrowed fluorescence spectra are discussed by theoretically analyzing the different contributions to the spectra. Results are presented that appear to explain the discrepancy between the previous hole-burning and fluorescence line-narrowing results (Reddy et al., 1994; Peterman et al., 1997) and lead to a consistent model for the electron-phonon coupling of the lowest  $Q_y$ -state of the LHC II complex.

## **2 Line-Narrowing Spectroscopies**

It was shown in the preceding chapter that the (non-line-narrowed) absorption and fluorescence spectra of trimeric LHC II remain broad and widely structureless even at low temperatures. Information on homogeneous linewidths, excited state energetic structure and electron-phonon coupling appears to be hidden by significant inhomogeneous broadening ( $\delta \approx 100 \text{ cm}^{-1}$ ). This phenomenon is common for systems of pigments embedded in amorphous (disordered) solids (for a review see Hayes et al., 1988a) and, in particular, for photosynthetic pigment-protein complexes (for a review see Reddy et al., 1992). Using quasi-monochromatic laser excitation at low temperatures, line-narrowing spectroscopies such as spectral hole-burning (for reviews see e.g. Avarmaa and Rebane, 1985; Reddy et al., 1992; Jankowiak et al., 1993) and fluorescence line-narrowing (for reviews see e.g. Personov, 1983; Avarmaa and Rebane, 1985; Jankowiak and Small, 1991) provide an elaborate experimental tool to improve the resolution of optical spectra for such systems. The scope of the following chapters is to briefly summarize physical background and common terminology (see Chapters 2.2 and 2.3), theory (see Chapter 2.4) as well as selected applications (see Chapter 2.5) of line-narrowing spectroscopies. In advance, however, it is instructive to discuss the origin of homogeneous and inhomogeneous broadening mechanism effective in pigment-protein complexes.

### **2.1 Inhomogeneous Broadening**

Briefly, broadening mechanisms are considered to be *homogeneous* when affecting an optical transition of all molecules in an ensemble in the same way. In contrast to this, *inhomogeneous* broadening leads to a distribution of transition frequencies within an ensemble of molecules.

The homogeneous width of an optical transition is determined by the excited state lifetime and the pure dephasing time. For example, processes like EET or radiative decay (emission) may lead to a depopulation and, therefore, to a finite lifetime  $T_1$  of an excited state. Furthermore, elastic scattering with protein phonons may induce a decay in phase coherence rather than a population

decay. Such processes are reflected by the pure dephasing time  $T_2'$ . Both time constants determine the total dephasing time  $T_2$ , which is given by

$$(T_2)^{-1} = (2T_1)^{-1} + (T_2')^{-1}. \quad (2)$$

$T_2$  is related to the homogeneous width  $\gamma$  in  $\text{cm}^{-1}$  by

$$\gamma = (c\pi T_2)^{-1}, \quad (3)$$

where  $c$  is the speed of light. To give an example for the magnitude of homogeneous broadening, the fluorescence lifetime of the lowest state of LHC II was found to be  $\sim 5$  ns at 10 K having a weak temperature dependence (Seydack et al., 1995; Vasil'ev et al., 1997a). According to Eqs. 2 and 3 this  $T_1$ -value corresponds to a width of  $\sim 0.001$   $\text{cm}^{-1}$ . Low-temperature  $T_1$ -times due to EET in LHC II may vary from several hundreds of femtoseconds to a few picoseconds depending on the  $Q_y$ -state excited (cf. Chapter 1.2). For example, a  $T_1$ -value of 1 ps corresponds to a width of  $\sim 5$   $\text{cm}^{-1}$ . At the same time, it is well-established that the contribution to  $\gamma$  due to pure dephasing in amorphous solids like proteins may be  $\sim 0.1$   $\text{cm}^{-1}$  at 4.2 K (Völker, 1989). Comparison of the latter value with the former two widths due to fluorescence lifetime and EET, respectively, establishes that at 4.2 K pure dephasing may dominate the homogeneous width  $\gamma$  of the lowest (fluorescing) state of LHC II, while its contribution is negligible for  $T_1$ -values shorter than  $\sim 10$  ps. This conclusion is important because line-narrowing spectroscopies are utilized at low temperatures. Note, that in contrast to the  $T_1$ -times the pure dephasing time exhibits a pronounced temperature dependence. At low temperatures ( $\sim 10$  K)  $\gamma$  from pure dephasing is expected to follow a  $T^{1.3}$  dependence while at temperatures with significant thermal occupation of phonon modes  $\gamma$  is  $\sim kT$ . The latter case is determined by  $kT \gg \hbar\omega_m$  for a given phonon mode with a frequency  $\omega_m$ . Thus, at room temperature the pure dephasing contribution to  $\gamma$  may be as high as 200  $\text{cm}^{-1}$ .

As to inhomogeneous broadening, it was already mentioned at the beginning of Chapter 1.2 that the specific microenvironment affects the transition frequency of a pigment molecule bound to a protein matrix. If pigment molecules were embedded into a perfect crystal, the environment would be the same for molecules at equivalent binding sites. Thus, the optical transitions of all these

pigment molecules would be observed at the same frequency, i.e. the corresponding absorption or fluorescence spectrum is homogeneously broadened.

It is known, however, that the low-temperature properties of amorphous solids such as proteins differ significantly from those of perfect crystals. These differences are the result of their complex microscopic structure (see Hayes et al., 1988a and references therein): First, amorphous solids are characterized by an almost infinite number of potential minima each corresponding to a different conformation of the chemically equivalent matrix. Second, within the manifold of potential minima there are bistable (nearly isoenergetic) configurations, the so-called two-level systems (TLS). TLS are basically asymmetric double well potentials (see Fig. 6). Third, the two configurations represented by the TLS minima differ in the arrangement of only a small number of atoms, i.e. transitions between the minima (rearrangements) are highly localized.

Fig. 6 (from Hayes et al., 1988a) shows TLS of a pigment-protein system in the ground (TLS  $\alpha$ ) and in the excited electronic state (TLS  $\beta$ ) of the chromophore, respectively. Each TLS is characterized by a barrier height  $V$  and a zero-point energy splitting  $\Delta$  as well as a well separation  $d$  (not labeled for TLS $_{\beta}$ ). Appropriate distribution functions for the latter three parameters have to be assumed to account for the variety of TLS present in an amorphous solid (see e.g. Kenney et al., 1990). Note that experimental data indicate the presence of a subset of TLS, which is created by or interacts more strongly with the bound chromophore. The latter TLS are referred to as *extrinsic* (TLS $_{\text{ext}}$ ) to be distinguished from the *intrinsic* TLS (TLS $_{\text{int}}$ ) of the amorphous solid. Both differ in their parameters and the distributions thereof. TLS $_{\text{int}}$  serve to explain anomalous low-temperature properties of amorphous solids such as specific heat, thermal conductivity and optical dephasing, while TLS $_{\text{ext}}$  seem to be more important for the understanding of the hole-burning mechanism (see Jankowiak et al., 1993 and references therein). A further discussion is beyond the scope of the qualitative picture given in this work.

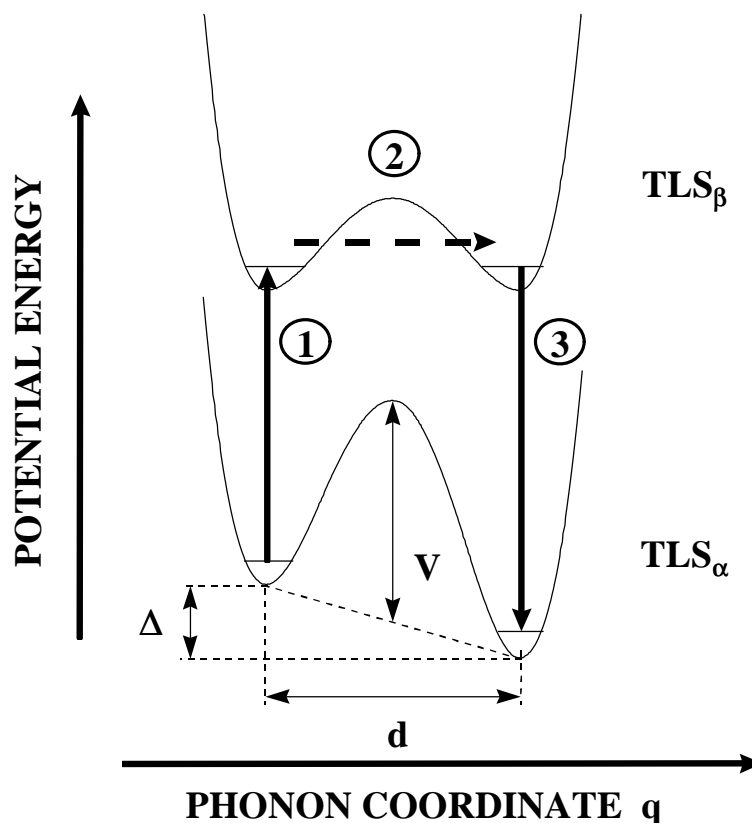


Figure 6. Asymmetric double-well potentials in the ground (TLS a) and excited electronic state (TLS b) of a pigment-protein system according to Hayes et al. (1988a).

It is apparent from Fig. 6 that the pigment-protein system can be trapped in either one of the two TLS  $\alpha$ -minima at low temperatures. Thermal equilibrium between the minima is then hindered by the barrier height  $V$ . Since the two minima correspond to different configurations of the protein matrix the environment of a certain pigment may vary from complex to complex resulting in a different transition frequency of the pigment in each case. Keeping in mind that the TLS represents two of an almost infinite number of potential minima, it is easily understood that there is broad distribution of transition frequencies in an ensemble of pigment-protein complexes that can be phenomenologically described by an inhomogeneous distribution function (IDF). Therefore, inhomogeneous broadening in pigment-protein complexes at low temperatures stems from the structural heterogeneity of the protein. The IDF is usually observed to be Gaussian with a width ( $\Gamma_{inh}$ ) of 100 - 500  $\text{cm}^{-1}$  (Hayes et al., 1988a).

Depending on the TLS-parameters  $V$ ,  $\Delta$  and  $d$ , there is a probability for phonon

assisted tunnel processes between the two TLS-minima corresponding to a spontaneous rearrangement of the protein matrix even at low temperatures. This process is called spectral diffusion, which is the frequency domain equivalent of pure dephasing.

To conclude this chapter it should be noted that the inhomogeneous width determines the spectral resolution of conventional (non-line-narrowed) spectroscopy. As will be shown in the next chapters, line-narrowing spectroscopies provide an opportunity to remove inhomogeneous broadening from optical spectra of pigment-protein complexes. The spectral resolution of these techniques is then limited by the homogeneous width  $\gamma$  of the optical transition or the corresponding total dephasing time  $T_2$ , respectively.

## **2.2 Hole-Burning Spectroscopy**

Spectral hole-burning (HB) utilizes quasi-monochromatic laser light to selectively bleach a particular transition frequency within an inhomogeneously broadened absorption band of a pigment-protein complex (burn process). In an experiment, it is sufficient that  $\Gamma_{\text{laser}} \ll \gamma$  to fulfill the requirement of „quasi-monochromatic“ excitation, i.e. the laser linewidth  $\Gamma_{\text{laser}}$  needs to be much narrower than the homogeneous linewidth  $\gamma$  of the optical transition. The change in the absorption spectrum produced during the burn process is subsequently tested by a second beam (read process). The difference spectrum between the absorption spectra recorded before and after the burn process is referred to as the „hole-burned“ spectrum. Because of excitation within the homogeneous linewidth  $\gamma$ , the hole-burned spectrum can be - more or less directly - related to the homogeneously broadened absorption spectrum (see Chapter 2.4 for a detailed discussion). The first observation of HB was reported almost simultaneously by Gorokhovski et al. (1974) and Kharlamov et al. (1974).

### **2.2.1 Hole-Burning Mechanisms**

Hole-burning processes can be distinguished, most general, by the timescale on which the change in absorption persists as well as by the mechanism that leads to the change in absorption. A hole is *transient* if the absorption change

is present only during the burn process, while it is *persistent* if the absorption change can be observed on a timescale much longer than the complete experiment. As to the mechanisms, these are generally referred to as photochemical, nonphotochemical or population bottleneck HB where the former two are generally assumed to yield persistent holes while the latter one produces transient holes. Briefly, HB is referred to as photochemical when the burn laser light induces a chemical reaction in the excited state of the pigment with the photoproduct absorbing at a different frequency. Therefore, the produced hole is usually considered to be persistent. In practice, the persistence of the hole-burned spectrum depends on the stability of the photoproduct. A detailed review on principles and applications of photochemical HB is given by Haarer (1989). In contrast to this, nonphotochemical hole-burning (NPHB) occurs in amorphous solids due to a rearrangement of the environment surrounding the (photochemically stable) chromophore as will be discussed in more detail in the following chapter. Finally, in population bottleneck HB the depletion of the ground state occurs because the excited state is coupled to a third, meta-stable state with typical lifetimes in the ms-range. Thus, the produced hole can be probed during (or within ms after) the burn process, only, and is, therefore, of transient nature. Transient HB was observed e.g. for the CP47 antenna complex of green plants where the Chl triplet state served as the bottleneck (Chang et al, 1994). Though the distinction given above appears to be clear and reasonable several intermediate cases and exceptions are known (see e.g. Hayes et al., 1988a).

### ***2.2.2 Nonphotochemical Hole-Burning***

Because the inhomogeneous broadening observed in optical low-temperature spectra of the LHC II pigment-protein complex stems from the amorphous nature of its protein backbone, it is the nonphotochemical HB mechanism that is of interest to this study. NPHB uses the bistability of the protein configurations to produce a loss of absorption at a certain frequency within the inhomogeneously broadened absorption band and is, therefore, best described in the framework of the TLS-model introduced in Chapter 2.1.

An explanation of nonphotochemical HB on the basis of TLS in amorphous

solids has first been given by Hayes and Small (1978) and was later refined by Shu and Small (1990). Fig. 6 shows the TLS of a pigment-protein system in the ground (TLS  $\alpha$ ) and in the excited state (TLS  $\beta$ ) of the chromophore. In simplest terms, it is assumed that the barrier height  $V$  between the two wells is altered upon excitation of the chromophore from the ground to the excited state (process (1) in Fig. 6). If the barrier height  $V$  is sufficiently lowered, matrix rearrangements, i.e. tunnel processes between the two minima of TLS  $\beta$ , become probable in the excited state, which are assumed to be mediated by electron-phonon coupling (process (2) in Fig. 6). Finally, de-excitation into the other ground state of TLS  $\alpha$  prepares an optical transition of different frequency (process (3) in Fig. 6). The higher barrier of TLS  $\alpha$  prevents the system from tunneling back into the initial ground state, *vide infra*. As mentioned at the beginning of Chapter 2.2 the loss in absorption associated with the selectively bleached transition can be tested by a second laser beam resulting in a partial removal of inhomogeneous broadening from the optical spectra of the pigment-protein system. It is apparent that *low temperatures* are required for NPHB to prevent thermally induced transitions within TLS  $\alpha$ . Raising the temperature after the burn process erases the hole.

The *burn efficiency* can be defined as the hole depth attained for a certain burn intensity. The *hole growth* is governed by the term  $\exp(-I\sigma\tau\Phi) L(\omega_B - \Omega_0)$  where  $I$  is the burn intensity,  $\sigma$  the absorption cross section,  $\tau$  the burn time,  $\Phi$  the NPHB quantum yield and  $L(\omega_B - \Omega_0)$  the lineshape of the absorbing electronic transition (Kenney et al., 1990). Within this exponential law, two factors carry an implicit dependence on the excited state lifetime: a) the efficiency of the tunnel process in TLS  $\beta$  represented by  $\Phi$  and b) the induced absorption profile  $L(\omega_B - \Omega_0)$ . As to the first, the efficiency of the tunnel process in TLS  $\beta$  is determined by the parameters  $V$ ,  $\Delta$ ,  $d$  and the distributions thereof, but can be conveniently expressed by the NPHB rate  $k_{\text{NPHB}}$ , which is typically in the order of  $(1 \text{ ns})^{-1}$  (Kim et al., 1995). Since the tunnel process competes with other processes depopulating the excited state, such as EET or radiative decay, one defines the NPHB quantum yield  $\Phi$ . In terms of rate constants,  $\Phi$  is proportional to  $k_{\text{NPHB}}/(T_1)^{-1}$  with  $T_1$  being the excited state lifetime. As to the

second, the burn laser beam selects (induces absorption by) those pigments absorbing at the burn frequency. The induced absorption of these pigments is determined, however, by a lineshape with a finite, homogeneous width  $\gamma$ , which cannot be removed by line-narrowing spectroscopies (see Chapter 2.1). Therefore, a higher burn intensity is needed to obtain the same depth for a broader hole and the hole depth becomes proportional to the total dephasing time  $T_2$  (see Eq. 2). In summary, there are two reasons for the burn efficiency of an optical transition becoming lower for shorter lifetime  $T_1$ . First, the excited state is depopulated faster compared to the timescale on which HB occurs and, second, a higher burn intensity is needed to obtain the same depth for a broader hole. The exponential law governing the hole growth implies that the selected electronic transitions can be almost entirely depleted, i.e. the hole becomes *saturated*.

It was illustrated that NPHB produces a loss of absorption at the burn frequency due to a rearrangement of the protein matrix. As a result the pigment-protein system absorbs at a different frequency producing a gain of absorption. The spectral feature associated with the gain of absorption is called *anti-hole*. It is usually blue-shifted from the burned hole and exhibits an asymmetric tailing towards higher energies. At the same time, the integrated intensity of the anti-hole equals that of the hole in NPHB (Hayes et al., 1988a).

Despite of the relatively high barrier  $V$  in TLS  $\alpha$  tunnel processes between the potential wells may also occur in the ground state (spectral diffusion). If such tunnel processes decrease the hole depth, they are referred to as *spontaneous hole filling*. Note that hole filling may also be due to secondary laser radiation, e.g. due to the test beam or white light. Such *laser-induced hole filling* may be understood as a „backward hole-burning“, i.e. it is a re-conversion of anti-hole states into pre-burn states via the excited state TLS. The efficiency of all hole filling processes determines the persistence of the NPHB spectrum (see Jankowiak et al., 1993 and references therein).

### **2.3 Fluorescence Line-Narrowing**

Fluorescence line-narrowing (FLN) spectroscopy employs quasi-monochromatic laser light to selectively excite emission from a certain

transition within an inhomogeneously broadened fluorescence band of a pigment-protein complex. As for spectral HB in absorption, the resulting line-narrowed fluorescence spectrum can be related to the homogeneously broadened fluorescence spectrum (see Chapter 2.4 for details). Thus, HB and FLN are complementary line-narrowing techniques, which may, in principle, provide equivalent information. The first observation of line-narrowing in fluorescence spectra was reported by Personov et al. (1973).

## ***2.4 Theoretical Background***

When theoretically describing the spectral properties of a pigment embedded in an amorphous protein matrix in the low-temperature limit basically two effects have to be taken into account: a) the electronic transition of each pigment is coupled to delocalized vibrations (phonons) of the protein matrix, and b), as discussed in Chapter 2.1, the differences of the microenvironment surrounding each pigment give rise to inhomogeneous broadening. An appropriate theory was developed for impurities disturbing the perfect structure of crystals and has later been extended for (isolated) pigments in amorphous hosts (see e.g. Rebane, 1970; Personov, 1983 and references therein). On the basis of these works, theories evolved to simulate hole profiles (Hayes et al., 1988b; Lee et al., 1989; Hayes et al., 1994) and line-narrowed fluorescence spectra (Personov, 1983; Mc Colgin, 1975). The following chapters provide a short summary of the theory used to analyze electron-phonon coupling of the lowest  $Q_y$ -state(s) of LHC II in this study. Proceeding from the basic assumptions (Chapter 2.4.1) and the optical spectra of a single pigment in an amorphous host (Chapter 2.4.2), the experimentally accessible inhomogeneously broadened spectra (Chapter 2.4.3) will be related to the corresponding line-narrowed spectra (Chapter 2.4.4) of a pigment-protein complex. For ease of comparison all model calculations illustrating theoretical expressions and dependencies on selected parameters are carried out for the same model system (see Table 1). In the presented approach, (excitonic) Chl-Chl interactions within the LHC II complex (see e.g. T. Renger, 2000 and references therein) are not taken into account. This seems to be justified for the purpose of this work because the lowest  $Q_y$ -state appears to be quite highly

localized on one Chl a molecule per LHC II trimer at 4.2 K (see Chapter 5).

### 2.4.1 Basic Principles

The most general form of the low-temperature absorption or fluorescence spectrum for an electronic transition of a single pigment embedded in an amorphous protein matrix is given by (see e.g. Personov, 1983)

$$G(\mathbf{w}, T) = \sum_n p_n(T) \sum_m \left| \langle fm | \hat{D} | in \rangle \right|^2 \mathbf{d}(E_{fm} - E_{in} - \hbar \mathbf{w}), \quad (4)$$

where the initial and final electronic states  $i$  and  $f$  are coupled to vibrational states  $n$  and  $m$ , respectively.  $E_{i,n}$  and  $E_{f,m}$  are the corresponding energetic positions. The transition probability for each set of  $n$  and  $m$  is given by the square of the transition matrix element

$$\langle fm | \hat{D} | in \rangle \quad (5)$$

containing the dipole moment operator  $\hat{D}$  as well as the initial and final state wavefunctions of the pigment-protein system. The entire spectrum is obtained by summation over the initial and final vibrational states  $n$  and  $m$  where the former are weighted by the thermal occupation probability  $p_n(T)$  for each  $n$ .

Concepts for a calculation of the transition matrix element (Eq. 5) and the complete spectrum (Eq. 4) were reviewed in detail in Pieper (1996). Briefly, all expressions discussed in the following chapters are valid for linear, harmonic Franck-Condon coupling (see e.g. Rebane, 1970). This situation is illustrated in Fig. 7 for an arbitrary vibrational frequency  $\omega_k$ . In simplest terms, the vibrations of the pigment-protein system are viewed as harmonic oscillators, i.e. the vibrational motion is governed by parabolic potentials in the ground and excited electronic state, respectively (harmonic approximation). Furthermore, it is assumed that the vibrations undergo no frequency change upon an electronic transition but only a shift  $a_k$  of their equilibrium position (linear approximation). Finally, within the Franck-Condon approximation the transition matrix element (Eq. 5) is given by

$$\langle fm | \hat{D} | in \rangle = \hat{D}_0 \prod_k \langle m_k | n_k \rangle, \quad (6)$$

i.e. the simple product of a purely electronic transition matrix element  $\hat{D}_0$  and a

phonon contribution, which is determined by the overlap of vibrational wavefunctions in the ground and excited electronic state, respectively. More graphically, this means that the pigment-protein system can be divided into a „fast“ electronic and a „slow“ vibrational subsystem. Then, the Franck-Condon principle requires that there is no vibrational motion nor a change of its momentum during an electronic transition. This simplification appears to be justified considering that the electronic motion is much faster than that of the heavier system of nuclei ( $m_{\text{electron}}/M_{\text{nucleus}} = 1836$  for the H-atom).

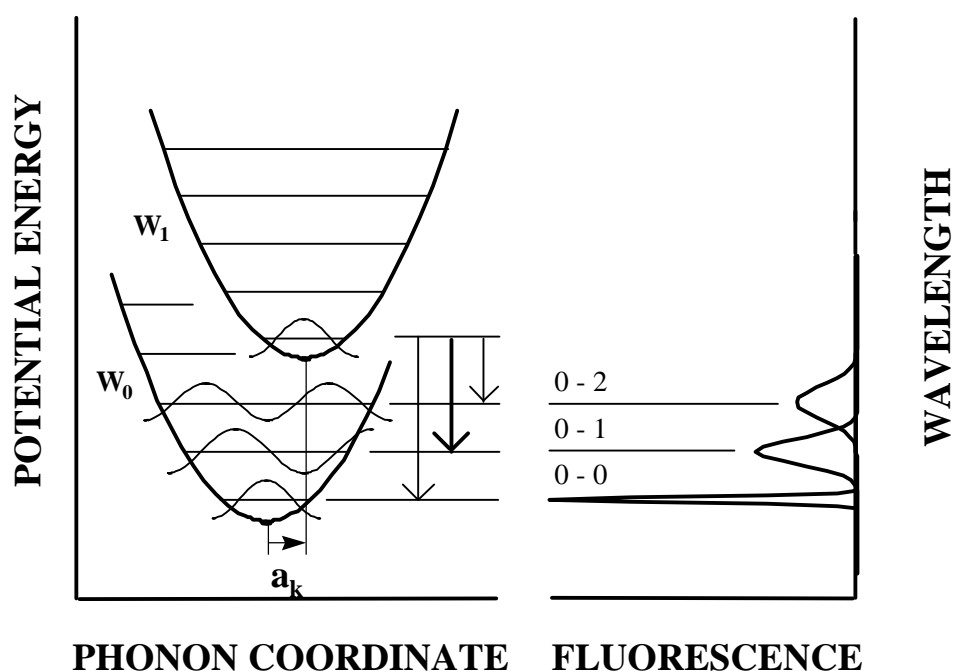


Figure 7. Potential energy diagram (left) of a pigment coupled to delocalized protein vibrations (phonons).  $W_0$  and  $W_1$  denote the parabolic potentials of the protein vibrations in the ground and excited electronic state of the pigment, respectively. The shift of their equilibrium position is marked by  $a_k$ . Thick and thin arrows label the intense and weak transitions between the discrete vibrational levels according to the Franck-Condon principle at low temperatures, respectively (simplified vibrational wavefunctions are given for illustrative purpose). The right scheme depicts the corresponding zero- (0-0), one- (0-1) and two-phonon (0-2) transitions of the fluorescence spectrum.

In general, the validity of the linear, harmonic Franck-Condon approximation does not depend on the actual degree of delocalization or localization of the vibrations considered. In the following, however, it will be assumed that the electronic transition is coupled to a distribution of delocalized vibrations of the

protein matrix (phonons). Then, the number of normal modes  $N$  of the matrix is  $N = 3n - 6$ , where  $n$  is the number of atoms constituting the oscillating system. In addition, the displacement  $a_k$  is of the order of  $N^{-1/2}$ , i.e.  $a_k$  is infinitely small for sufficiently delocalized vibrations (see e.g. Rebane, 1970; Hayes et al., 1988b).

For further illustration of linear, harmonic Franck-Condon coupling to a given phonon frequency  $\omega_k$ , the right part of Fig. 7 shows simplified wavefunctions for some of the discrete phonon levels in the ground and excited electronic state of a pigment-protein system, respectively. A corresponding schematic fluorescence spectrum is given in the left part of Fig. 7. At low temperatures only the lowest phonon level of the excited state is occupied after excitation and subsequent thermal equilibrium, i.e. no phonons are excited. Its wavefunction overlaps that of the lowest phonon level of the ground state so that there is a probability for an electronic transition without creation of phonons. An optical transition without a change in population of phonon levels is called zero-phonon transition and leads to the formation of zero-phonon lines (ZPL) in optical spectra (see schematic fluorescence spectrum to the right of the potential energy diagram in Fig. 7). All other transitions induce the creation of a certain number of phonons and are, therefore, referred to as one-, two-,..., multi-phonon transitions. Thus, the emitted photons are of lower frequency than those of the zero-phonon transition and the corresponding spectral features appear at the low-energy side of the ZPL. Spectral features associated with a change in population of phonon levels constitute the phonon sideband (PSB). Fig. 7 shows only the one- and two-phonon transitions for simplicity. It is obvious from the overlap of the phonon wavefunctions that the one-phonon transition is the most intense. The transition probabilities in absorption (not shown) are easily derived assuming that the lowest phonon level of the ground state is populated and considering the overlap with the excited state phonon wavefunctions. In this case, higher photon frequencies than those absorbed by the zero-phonon transition have to be employed to excite multi-phonon transitions and the corresponding spectral features appear at the high-energy side of the ZPL. Thus, within linear, harmonic Franck-Condon coupling, there is perfect mirror symmetry between absorption and fluorescence spectra. For theory and experimental evidence of a breakdown of

this relation within quadratic electron-phonon coupling see Osadko (1983).

**2.4.2 Homogeneously Broadened Spectra**

For simplicity of the following discussion, one may define the low-temperature limit by  $kT \ll \hbar\omega_m$  where T is the temperature, k the Boltzmann constant and  $\omega_m$  a given phonon frequency. At such temperatures thermal population of phonon levels is negligible.

In the low-temperature limit, the result of Hayes et al. (1988b) for homogeneously broadened absorption and fluorescence spectra  $L(\omega)$  in the case of linear, harmonic Franck-Condon coupling to a distribution of delocalized phonons<sup>1</sup> with a mean frequency  $\omega_m$  is

$$L(\omega) = \underbrace{e^{-S} I_0(\omega - \Omega_0)}_{ZPL} + \underbrace{\sum_{R=1}^{\infty} S^R \frac{e^{-S}}{R!} I_R(\omega - \Omega_0 \mp R\omega_m)}_{PSB}, \quad (7)$$

where  $-R\omega_m$  and  $+R\omega_m$  correspond to absorption and fluorescence, respectively. The Lorentzian ZPL  $I_0(\omega - \Omega_0)$  peaks at  $\Omega_0$  and carries a homogeneous width  $\gamma$ . The intensity distribution within the spectrum is determined by a Poisson type weighting factor for every R, which is governed by the Huang-Rhys factor S. In particular, the intensity of the ZPL is  $\exp(-S)$ . Note in this regard, that all lineshape functions have to be properly normalized. The phonon side band (PSB) consists of all R-phonon transitions ( $R=1,2,\dots$ ) with lineshapes  $I_R(\omega - \Omega_0 \mp R\omega_m)$  peaking at  $\Omega_0 \pm R\omega_m$ . The one-phonon profile  $I_1(\omega - \Omega_0 \mp \omega_m)$  represents the product  $g(\omega)D(\omega)$  with  $g(\omega)$  being the density of states of the phonon modes and  $D(\omega)$  an electron-phonon coupling term. Each profile  $I_R$  ( $R>1$ ) is completely determined by the shape of  $I_1$  and obtained by folding  $I_1$  R times with itself. Especially, for  $I_1$  being a Gaussian (Lorentzian) with a full width at half maximum (FWHM)  $\Gamma_G$  ( $\Gamma_L$ ) the profile  $I_R$  becomes a Gaussian (Lorentzian) with FWHM  $\sqrt{R} \Gamma_G$  ( $R \Gamma_L$ ) (Hayes et al., 1988b).

---

<sup>1</sup> By coincidence, the same expression is obtained for coupling to localized vibrations (cf. Chapter 2.4.1) in the low-temperature limit (see e.g. Rebane, 1970). The difference, however, is the physical meaning of the one-phonon profile, which mainly reflects the density of phonon states for delocalized vibrations but a homogeneous (lifetime limited) width in the case of localized vibrations. Thus, Eq. 7 permits an inclusion of localized vibrations.

Guided by the work of Hayes et al. (1994) and the references given therein the one-phonon profile  $I_1$  can be assumed to be asymmetric with a Gaussian shape at its low-energy wing and a Lorentzian shape at its high-energy wing. Then, the full profile has a peak frequency of  $\omega_m$  and a width of  $\Gamma = \Gamma_G/2 + \Gamma_L/2$ .

Table 1 Parameters of the model calculations shown in Figs. 9 - 14.

temperature	T [K]	5
position of IDF	$\omega_C$ [ $\text{cm}^{-1}$ ]	0
homogeneous width	$\gamma$ [ $\text{cm}^{-1}$ ]	2.0
inhomogeneous width	$\Gamma_{\text{inh}}$ [ $\text{cm}^{-1}$ ]	80
Huang-Rhys factor	S	1.0
peak phonon frequency	$\omega_m$ [ $\text{cm}^{-1}$ ]	20
FWHM of Gaussian wing	$\Gamma_G$ [ $\text{cm}^{-1}$ ]	10
FWHM of Lorentzian wing	$\Gamma_L$ [ $\text{cm}^{-1}$ ]	30
FWHM of one-phonon profile	$\Gamma$ [ $\text{cm}^{-1}$ ]	20

It follows from the discussion of Eq. 7 that electron-phonon coupling of a pigment-protein system is completely determined by the one-phonon profile  $I_1$  given by  $\omega_m$ ,  $\Gamma_G$  and  $\Gamma_L$  as well as by the Huang-Rhys factor S. The shape of the one-phonon profile mainly reflects the density of states of the protein phonons. The Huang-Rhys factor S represents the strength of electron-phonon coupling. In terms of ZPL ( $I_{\text{ZPL}}$ ) and PSB intensity ( $I_{\text{PSB}}$ ), S can be defined as (see Eq. 7)

$$e^{-S} = I_{\text{ZPL}} / (I_{\text{ZPL}} + I_{\text{PSB}}). \quad (8)$$

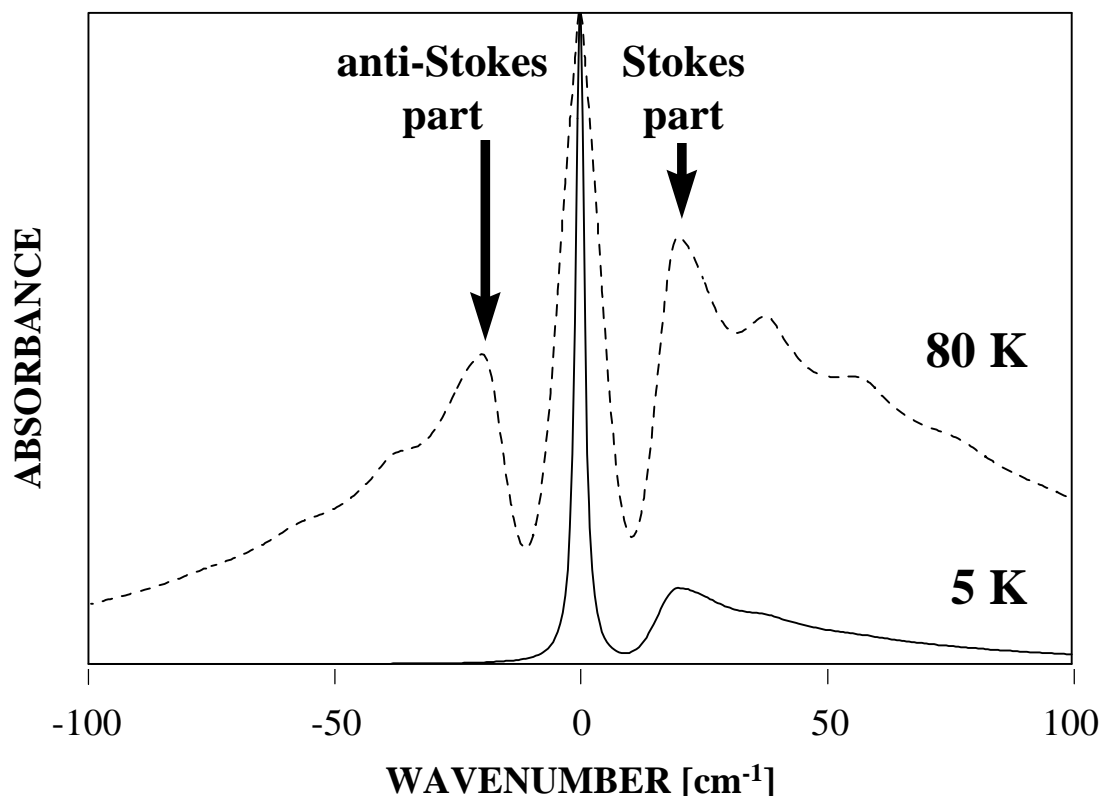


Figure 8. Homogeneously broadened absorption spectra calculated according to Eqs. 7 and 9 for the model system defined in Table 1 and temperatures of 5 and 80 K, respectively.

The lower spectrum shown in Fig. 8 is a homogeneously broadened absorption spectrum of a pigment embedded in an amorphous host in the low-temperature limit. It was calculated according to Eq. 7 for a model system defined by  $\omega_C = 0 \text{ cm}^{-1}$ ,  $\Gamma_{inh} = 80 \text{ cm}^{-1}$ ,  $S = 1.0$ ,  $\omega_m = 20 \text{ cm}^{-1}$ ,  $\Gamma_G = 10 \text{ cm}^{-1}$ ,  $\Gamma_L = 30 \text{ cm}^{-1}$  and  $\gamma = 2 \text{ cm}^{-1}$  (see Table 1). Clearly visible are the narrow ZPL, i.e. absorption at a distinct frequency due to the purely electronic transition, and the broad PSB, i.e. absorption at higher frequencies due to phonon-assisted transitions. Note, that the PSB is not identical with the one-phonon profile  $I_1$  but reflects the sum of all R-phonon transitions. The dependence of the homogeneously broadened spectrum of a pigment-protein system on  $S$  and  $\omega_m$  has already been discussed in Pieper (1996).

Considering arbitrary temperatures thermal population of phonon levels according to the Bose-Einstein statistics has to be taken into account. In this case the expression of Hayes et al. (1994) for the homogeneously broadened absorption and fluorescence spectra takes the form

$$L(\mathbf{w}) = e^{-\sum_k S_k (2\bar{n}_k + 1)} \prod_k \sum_{R=0}^{\infty} \sum_{r=0}^R \frac{[S_k (\bar{n}_k + 1)]^{R-r} [S_k \bar{n}_k]^r}{(R-r)! r!} \times l_{R,r} \left[ \mathbf{w} - \Omega_0 \mp \sum_k (R-2r) \mathbf{w}_k \right], \quad (9)$$

where

$$\bar{n}_k = [\exp(\hbar \mathbf{w}_k / kT) - 1]^{-1} \quad (10)$$

denotes the thermal occupation number of phonons of a frequency  $\omega_k$  and - and + correspond to absorption and fluorescence, respectively. The product over  $k$  allows for inclusion of different phonon modes. The factors  $S_k (\bar{n}_k + 1)$  and  $S_k \bar{n}_k$  represent phonon creation and annihilation, respectively. As in Eq. 7,  $R$  ( $R=1,2,\dots$ ) denotes the total number of phonon transitions (creation and annihilation) while  $r$  gives the number of annihilated phonons ( $0 \leq r \leq R$ ). Accordingly, optical transitions with more phonons being created than annihilated ( $R-r > r$ ) give rise to the Stokes-part while those with more phonons being annihilated than created ( $R-r < r$ ) constitute the anti-Stokes part of the PSB. In absorption, these spectral features appear on the high- and low-energy side of the ZPL, respectively. Those transitions with the same number of created and annihilated phonons ( $R-r = r$ ) are coincident with the ZPL. By analogy to Eq. 7, the profile  $I_{R,r}$  ( $R>1$ ) is obtained by folding the one-phonon profile  $I_{1,0}$   $|R-2r|$ -times with itself. Then, for  $I_{1,0}$  being a Gaussian with a width of  $\Gamma_G$  the profile  $I_{R,r}$  becomes a Gaussian with a width of  $|R-2r|^{1/2} \Gamma_G$ . If  $I_{1,0}$  is a Lorentzian with a width of  $\Gamma_L$  the profile  $I_{R,r}$  becomes a Lorentzian with a width of  $|R-2r| \Gamma_L$  (Hayes et al., 1994). In the low-temperature limit ( $T \rightarrow 0$  K)  $\bar{n}_k$  tends to zero and Eq. 9 reduces to Eq. 7.

The temperature dependence of the homogeneously broadened spectrum of a pigment-protein system is also illustrated in Fig. 8. In addition to the 5 K spectrum discussed above, Fig. 8 shows a homogeneously broadened absorption spectrum calculated according to Eq. 9 for the model system of Table 1 and a temperature of 80 K (normalized peak intensity). At 80 K the Stokes- and the anti-Stokes part of the PSB are clearly visible at the high- and low-energy side of the ZPL, respectively. Because of the considerable thermal

population of phonon levels at 80 K Stokes- and anti-Stokes part carry almost equivalent absorption intensities while the relative intensity of the ZPL is significantly smaller than in the low-temperature limit. The most striking observation is, however, that at 80 K a single pigment may absorb light in a broad frequency range due to electron-phonon coupling.

### 2.4.3 Non-Line-Narrowed Spectra

The absorption and fluorescence spectra for an ensemble of pigments embedded in an amorphous protein matrix is obtained by convolution of the homogeneously broadened spectrum (Eqs. 7 and 9) with the IDF  $N(\Omega_0 - \omega_c)$  (see Chapter 2.1) peaking at  $\omega_c$  that is assumed to exhibit Gaussian shape and is characterized by its FWHM  $\Gamma_{inh}$ . As discussed in Chapter 2.1,  $\Gamma_{inh}$  can be viewed as a measure for the inherent heterogeneity of the protein matrix. In the low-temperature limit these spectra are given by

$$L(\omega) = \sum_{R=0}^{\infty} \left( S^R \frac{e^{-S}}{R!} \right) \int d\Omega_0 N(\Omega_0 - \omega_c) l_R(\omega - \Omega_0 \mp R\omega_m), \quad (11)$$

where  $-R\omega_m$  and  $+R\omega_m$  correspond to absorption and fluorescence, respectively.

The lower part of Fig. 9 shows homogeneously broadened absorption spectra in the low-temperature limit (see full and dashed lines), which were calculated according to Eq. 7 for the model system defined in Chapter 2.4.2 (see Table 1). The intensities of the ZPL are distributed according to a Gaussian IDF with  $\Gamma_{inh} = 80 \text{ cm}^{-1}$  (see dashed-dotted line). The upper part of Fig. 9 shows the resulting inhomogeneously broadened absorption and fluorescence spectra calculated according to Eq. 11 in the low-temperature limit. As known from experiments performed under non-line-narrowing conditions, these spectra are widely structureless (cf. Chapter 1.2). When  $\omega_m < \Gamma_{inh}$ , the separate ZPL and PSB features are masked by the relatively broad IDF, which determines the spectral resolution of conventional spectroscopy. The only apparent manifestations of electron-phonon coupling are the slight asymmetry of the spectra as well as the Stokes shift between the absorption and fluorescence maxima (cf. Chapter 2.4.1). This shift is given by (Hayes et al., 1988b)

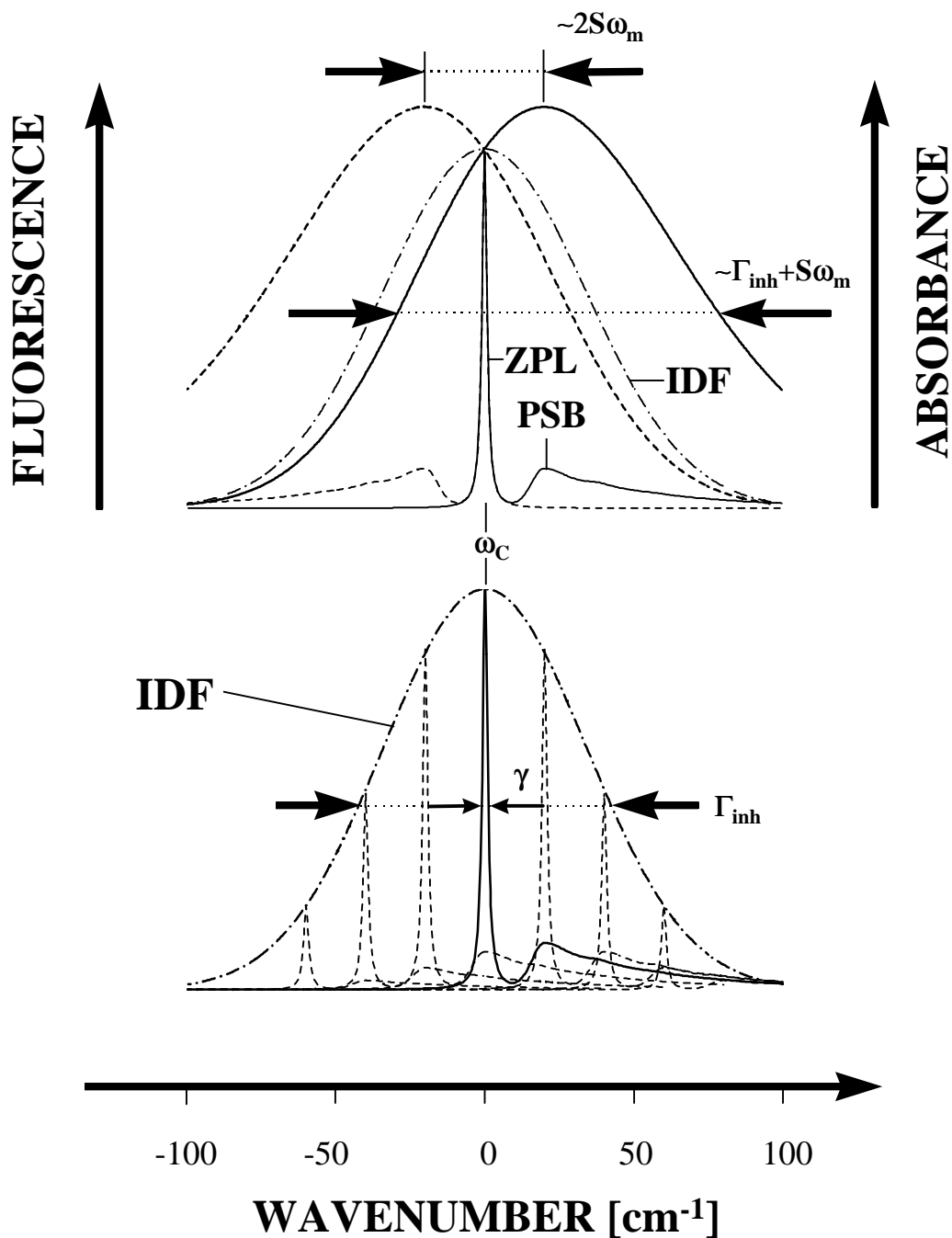


Figure 9. Low-temperature homogeneously broadened and non-line-narrowed spectra for the model system defined in Table 1. Lower part: homogeneously broadened absorption spectra (full and dashed lines) calculated according to Eq. 7 and distributed according to the IDF (dashed-dotted line). Upper part: resulting (experimentally accessible) non-line-narrowed absorption (full line) and fluorescence spectra (dashed line) calculated according to Eq. 11. The corresponding homogeneously broadened spectra and IDF are given for comparison.

$$\Delta \mathbf{w} = \sum_k 2S_k \mathbf{w}_k, \quad (12)$$

which reduces to

$$\Delta \omega \sim 2S\omega_m \quad (13)$$

in the mean phonon frequency approximation. At the same time the width of the non-line-narrowed spectra is approximately (Hayes et al., 1988b)

$$\Gamma_{\text{non-line}} \sim \Gamma_{\text{inh}} + S\omega_m. \quad (14)$$

Note the perfect mirror symmetry between absorption and fluorescence spectra, which is the result of linear Franck-Condon coupling.

The inhomogeneously broadened absorption and fluorescence spectra for arbitrary temperatures are obtained by convolution of the IDF with Eq. 9, which is given by

$$L(\mathbf{w}) = e^{-\sum_k S_k (2\bar{n}_k + 1)} \prod_k \sum_{R=0}^{\infty} \sum_{r=0}^R \frac{[S_k (\bar{n}_k + 1)]^{R-r} [S_k \bar{n}_k]^r}{(R-r)! r!} \times \int d\Omega_0 N(\Omega_0 - \mathbf{w}_C) J_{R,r} \left[ \mathbf{w} - \Omega_0 \mp \sum_k (R-2r) \mathbf{w}_k \right] \quad (15)$$

In summary, Eqs. 11 and 15 permit a calculation of non-line-narrowed absorption and fluorescence spectra in the low-temperature limit and for arbitrary temperatures, respectively. Calculations have to be based on given parameters ( $S$ ,  $\gamma$ ,  $\omega_m$ ,  $\Gamma_G$ ,  $\Gamma_L$ ,  $\Gamma_{\text{inh}}$ ) characterizing inherent properties of the pigment-protein system, *vide supra*. In this study, Eqs. 11 and 15 are used to verify the validity of parameters obtained by line-narrowing spectroscopies (see next chapter).

#### **2.4.4 Line-Narrowed Spectra**

In a next step, expressions for line-narrowed spectra of a pigment-protein system shall be developed in the low-temperature limit. As for HB, the preburn (absorption) spectrum  $A(\tau=0, \omega)$  is given by Eq. 11 (Hayes et al., 1988b) where  $\tau$  is the burn time, *vide infra*. In Chapter 2.2.2 it was demonstrated how quasi-monochromatic laser radiation may produce a persistent loss of absorption for a distinct electronic transition within an inhomogeneously broadened absorption band. For a theoretical calculation of the hole profile it is necessary

to go beyond that approach and consider a finite width  $\gamma$  of the ZPL ( $\Gamma_{\text{laser}} \ll \gamma$ ) and coupling of the electronic transitions to protein phonons as already implied by Eq. 11. Then, exposition of the pigment-protein system to burn laser light of a frequency  $\omega_B$  for a burn time  $\tau$  modifies the IDF as given by (Hayes et al., 1988b)

$$N(\mathbf{t}, \Omega_0 - \mathbf{w}_C) = N(\Omega_0 - \mathbf{w}_C) \exp[-\sigma I \Phi \mathbf{t} L(\mathbf{w}_B - \Omega_0)], \quad (16)$$

where the exponential term describes the hole growth due to tunnel processes in the excited state TLS of the system as discussed in Chapter 2.2.2. The lineshape  $L(\omega_B - \Omega_0)$  is given by Eq. 7 and represents those electronic transitions within the IDF, which are resonantly (i.e. through their ZPL) and non-resonantly (i.e. through their PSB) bleached at the burn frequency, *vide infra*. Each of the purely electronic transitions bleached according to Eq. 16 carries a finite width  $\gamma$  of the ZPL and is accompanied by a PSB. Therefore, the homogeneously broadened absorption spectrum (Eq. 7) has to be convoluted with the modified IDF (Eq. 16) to yield the entire absorption spectrum after a burn time  $\tau$ , which is given by (Hayes et al., 1988b)

$$A(\mathbf{t}, \mathbf{w}) = \sum_{R=0}^{\infty} \left( S^R \frac{e^{-S}}{R!} \right) \int d\Omega_0 N(\Omega_0 - \mathbf{w}_C) \times \exp[-\sigma I \Phi \mathbf{t} L(\mathbf{w} - \Omega_0)] l_R(\mathbf{w} - \Omega_0 - R\mathbf{w}_m) \quad (17)$$

The hole-burned spectrum  $\Delta A(\omega)$  is obtained subtracting Eq. 11 from Eq. 17

$$\Delta A(\omega) = A(\tau, \omega) - A(\tau=0, \omega). \quad (18)$$

A physically more transparent form of the HB-spectrum can be obtained in the short burn time limit, which is defined by  $\sigma I \Phi \tau \ll 1$ . Then, expressing the exponential by its Taylor-series, neglecting second and higher order terms as well as replacing  $L(\omega_B - \Omega_0)$  by Eq. 7, Eq. 18 reduces to (Hayes et al., 1988b)

$$\Delta A(\mathbf{w}) = \sum_{R,P=0}^{\infty} \left( S^R \frac{e^{-S}}{R!} \right) \left( S^P \frac{e^{-S}}{P!} \right) \int d\Omega_0 N(\Omega_0 - \mathbf{w}_C) \times l_P(\mathbf{w}_B - \Omega_0 - P\mathbf{w}_m) l_R(\mathbf{w} - \Omega_0 - R\mathbf{w}_m) \quad (19)$$

where  $l_P$  represents the electronic transitions bleached during the burn process. For simplicity, the prefactor  $\sigma I \Phi \tau$  was set equal to unity.

The low-temperature FLN spectrum  $F(\omega)$  can be deduced directly from Eq. 19.

Assuming that laser light of a frequency  $\omega_E$  selectively excites electronic transitions within the IDF as given by Eq. 16 as well as low excitation intensities to justify the series expansion that led to Eq. 19, the only necessary modification is to use the lineshape  $l_R$  of the homogeneously broadened fluorescence spectrum. Thus,  $F(\omega)$  is given by

$$F(\omega) = \sum_{R,P=0}^{\infty} \left( S^R \frac{e^{-S}}{R!} \right) \left( S^P \frac{e^{-S}}{P!} \right) \int d\Omega_0 N(\Omega_0 - \omega_C) \times \quad , (20)$$

$$l_P(\omega_E - \Omega_0 - P\omega_m) l_R(\omega - \Omega_0 + R\omega_m)$$

which resembles the expressions of Mc Colgin (1975) and Personov (1983). However, Eq. 20, uses the lineshape functions of Hayes et al. (1988b), which implicitly account for damping (broadening) of multi-phonon transitions (see Chapter 2.4.2). Thus, Eqs. 18, 19 and 20 permit an analysis of phonon structure in HB and FLN spectra on the basis of a consistent theoretical model.

For illustration of the abstract expressions given above, Fig. 10 shows line-narrowed spectra calculated for the model system defined in Chapter 2.4.2 (see Table 1) and  $\Gamma_{inh} = 80 \text{ cm}^{-1}$ . Thus, the results are directly comparable to the homogeneously broadened absorption and non-line-narrowed spectra discussed in Chapters 2.4.2 and 2.4.3, respectively (see also Fig. 9). The full line in the lower part of Fig. 10 is a hole-burned spectrum calculated for  $\omega_B = 0 \text{ cm}^{-1}$  according to Eq. 19, i.e. HB in the center of the IDF. The full line in the upper part of Fig. 10 is a line-narrowed fluorescence spectrum calculated for  $\omega_E = 0 \text{ cm}^{-1}$  according to Eq. 20. For comparison, the central part of Fig. 10 shows corresponding homogeneously broadened absorption spectra and the Gaussian IDF (see also Fig. 9).

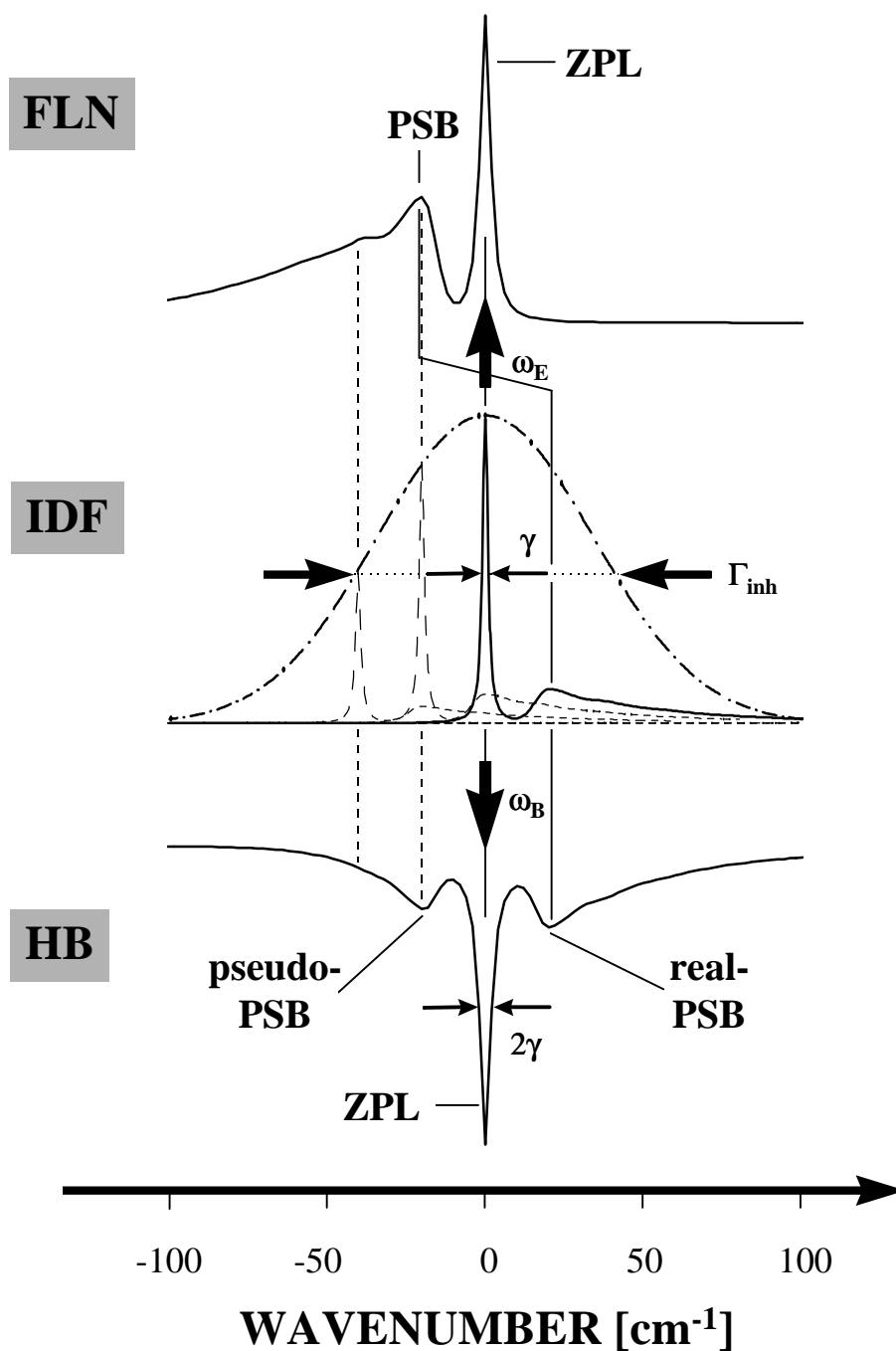


Figure 10. Low-temperature line-narrowed spectra for an excitation/ burn frequency of  $w_E/w_B = 0 \text{ cm}^{-1}$  (see arrows) and the model system defined in Table 1. Central part: homogeneously broadened absorption spectra calculated according to Eq. 7 and distributed according to the IDF (dashed-dotted line). Absorption spectra of resonantly and non-resonantly excited pigments are shown as full and dashed lines, respectively. Absorption spectra of pigments which are not excited were omitted for ease of inspection. Upper part: resulting line-narrowed fluorescence spectrum calculated according to Eq. 20. Lower part: resulting hole-burned spectrum calculated in the short burn time limit according to Eq. 19.

The hole-burned spectrum exhibits a sharp zero-phonon hole (ZPH) coincident with the burn frequency  $\omega_B$  and phonon sideband holes (PSBH) on both sides of the ZPH. The ZPH is due to electronic transitions, which are resonantly bleached, i.e. their ZPL overlap the burn frequency  $\omega_B$ . Because of the finite ZPL width  $\gamma$  and the continuous distribution of ZPL within the IDF, electronic transitions close to  $\omega_B$  contribute to the ZPH when absorbing through their Lorentzian wings. Thus, the resulting ZPH width<sup>2</sup> is  $2\gamma$ . The feature at the high-energy side of the ZPH is the real-PSBH, which is due to the phonon wings that build on the ZPH. ZPH and real-PSBH correspond to ZPL and PSB of the homogeneously broadened absorption spectrum, respectively. In addition, there are electronic transitions at lower energy than  $\omega_B$ , which are excited through their phonon wings. These transitions form the pseudo-PSBH, which is the mirror image of the real-PSB. The selection of homogeneously broadened absorption spectra by HB is further illustrated in the central part of Fig. 10. The spectrum represented by the full line is resonantly bleached and leads to formation of ZPH and real-PSBH. The spectra given by dashed lines are non-resonantly bleached via their PSB and contribute to the pseudo-PSBH. Electronic transitions at higher energy than  $\omega_B$  do not contribute to the hole-burned spectrum. The composition of the FLN spectrum is quite similar to that of the HB spectrum discussed above. The only exception is that the real-PSB lies on the low-energy side of the ZPL and is, therefore, superimposed on the pseudo-PSB. Thus, the FLN spectrum exhibits less structure than the HB spectrum. A more detailed discussion of the composition of line-narrowed spectra will be given in Chapter 7.

---

<sup>2</sup> The theory discussed in the present chapter does not account for finite laser linewidth nor spectral resolution. If either of the latter two parameters is of the same magnitude as the homogeneous width  $\gamma$ , the ZPH width is given by  $\Gamma_{ZPH} = 2\gamma + \delta$ , where  $\delta$  accounts for an additional contribution.

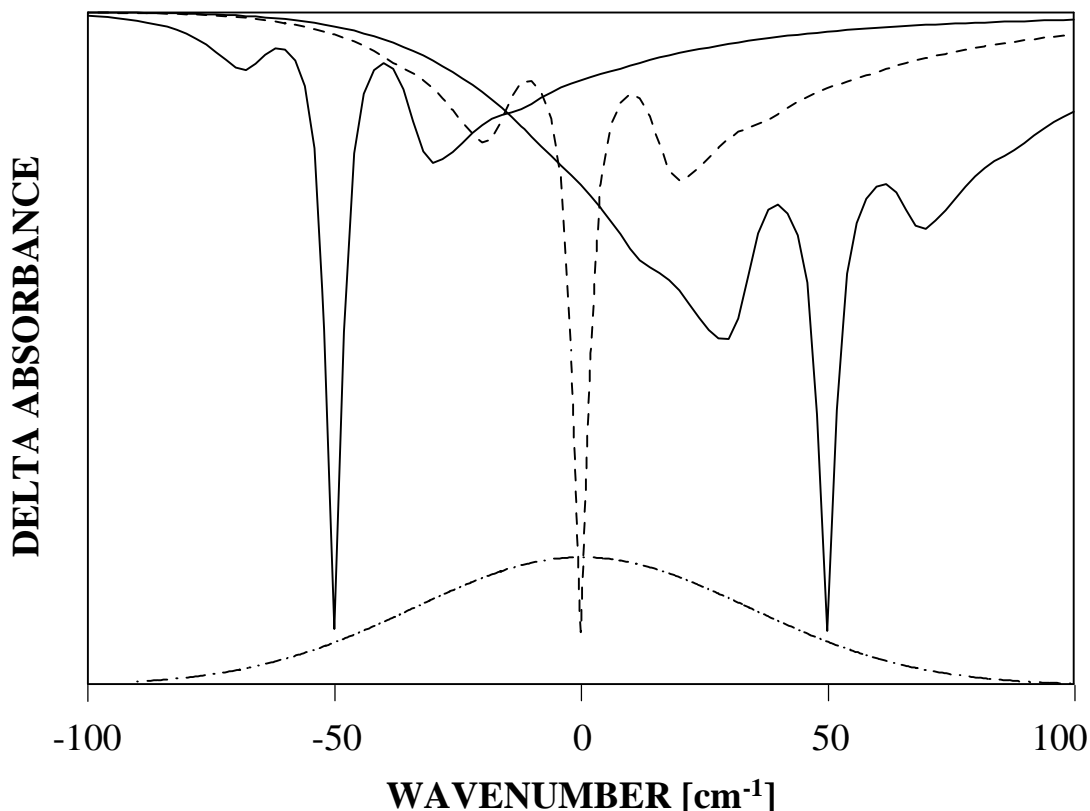


Figure 11. Low-temperature hole-burned spectra calculated in the short burn time limit according to Eq. 19 for the model system defined in Table 1 and burn frequencies  $\omega_B$  of  $-50$ ,  $0$ , and  $+50 \text{ cm}^{-1}$  within the IDF profile. The IDF profile (dashed-dotted line) is shown for comparison. The hole-burned spectrum for a burn frequency  $\omega_B$  of  $0 \text{ cm}^{-1}$  is given by a dashed line for ease of inspection.

Hole-burned spectra (normalized hole depth) calculated for different burn frequencies within the IDF are shown in Fig. 11. The shape of the IDF is given at the bottom for comparison. The mirror symmetry of the PSBH shapes appears to be maintained for every  $\omega_B$ . Most striking, however, is the burn frequency dependence of the PSBH intensities. Especially, the intensity of the pseudo-PSBH decreases drastically if  $\omega_B$  is tuned to lower energies. This is the result of a decreasing number of electronic transitions within the IDF that can be bleached non-resonantly. At the same time, the intensity of the real-PSB remains almost constant. The slight increase in intensity of the real-PSBH for  $\omega_B = 50 \text{ cm}^{-1}$  is mainly due to an overlap with the high-energy wing of the quite intense pseudo-PSBH. On the basis of similar calculations, Hayes et al. (1988b) concluded that the Huang-Rhys factor  $S$  can always be obtained from the ratio of real-PSB to ZPH intensity according to the simple Eq. 8. If the pseudo-PSB is employed,  $\omega_B$  should be located in the low-energy wing of the

IDF in order to reduce the contribution from non-resonantly bleached electronic transitions. In this case, the pseudo-PSB intensity equals approximately that of the real-PSB.

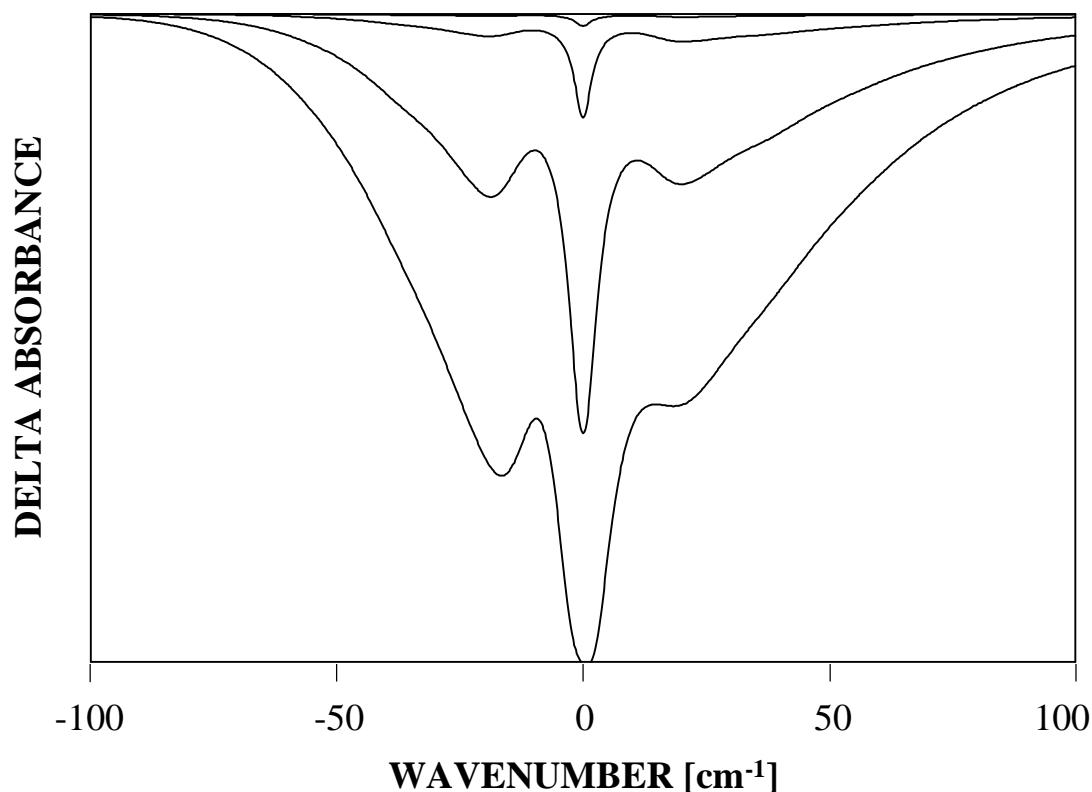


Figure 12. Low-temperature hole-burned spectra calculated according to Eq. 18 for the model system defined in Table 1,  $w_B = 0 \text{ cm}^{-1}$ , and  $sIFt$  -values of 0.00001, 0.0001, 0.001 and 0.005 (from top to bottom). The resulting hole depths are 2, 14, 57, and 98 % of the saturated depth, respectively.

It is apparent from Eq. 17 that the hole-burned spectrum may also depend on burn intensity ( $I$ ) or on burn time ( $\tau$ ). Because the effect of variation of either parameter is similar, one defines the term burn fluence ( $I\tau$ ). The burn fluence dependence of hole-burned spectra is illustrated in Figs. 12 and 13. The hole-burned spectra are calculated according to Eq. 17 for the model system defined in Chapters 2.4.2 and 2.4.3 as well as  $\omega_B = 0 \text{ cm}^{-1}$ . The fractional hole depths  $\Delta A/A$  of the ZPH in the spectra of Fig. 12 correspond (from top to bottom) to 2, 14, 54, and 98 % of its saturated depth for  $\sigma I\Phi\tau$  -values (representing the burn fluence  $I\tau$  for fixed  $\sigma\Phi$ ) of 0.00001, 0.0001, 0.001 and 0.005, respectively. In Fig. 12 the top spectrum represents the short burn time limit, i.e. it is comparable to the spectra shown in Fig. 11. The spectrum at the bottom of

Fig. 12 is close to saturation, i.e. the holes have attained maximal depth because the electronic transitions overlapping  $\omega_B$  are completely depleted. According to Hayes et al. (1988b) the saturated fractional hole depth of the ZPH is given by

$$\Delta A/A_{\text{saturated}} = \exp(-S). \quad (21)$$

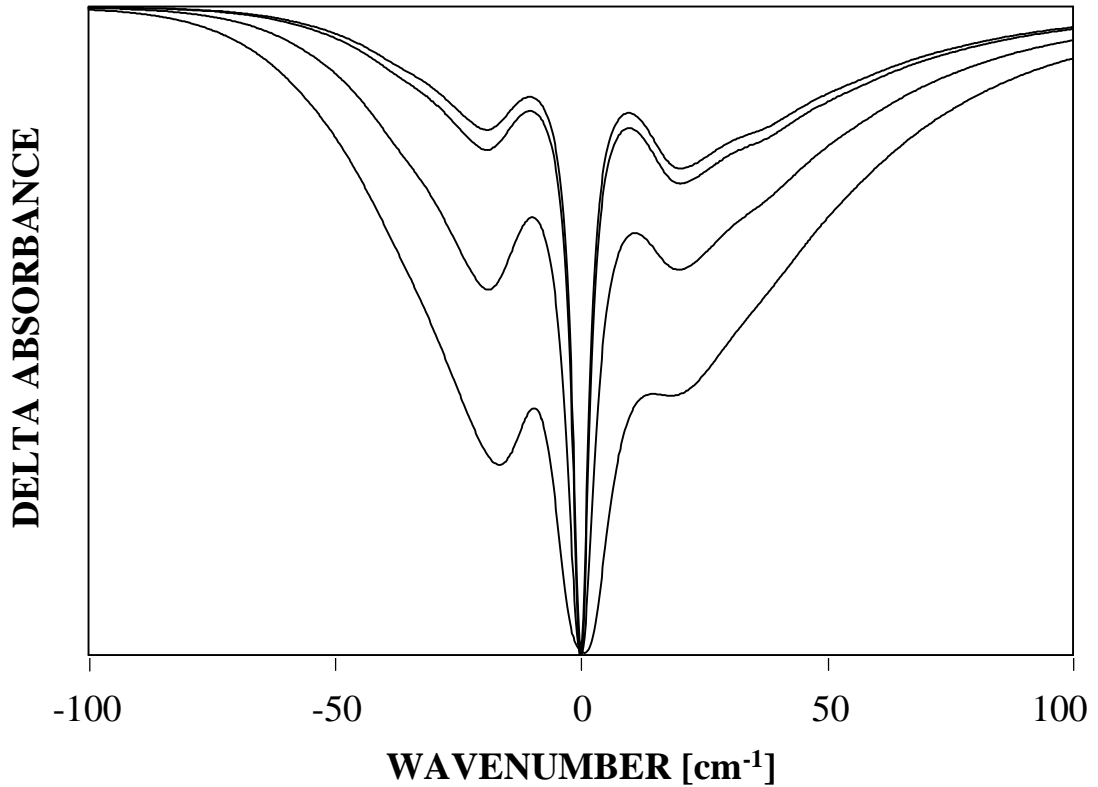


Figure 13. Low-temperature hole-burned spectra of Fig. 12 normalized to the same hole depth. Spectra were calculated according to Eq. 18 for the model system defined in Table 1,  $w_B = 0 \text{ cm}^{-1}$ , and  $sIFt$  -values of 0.00001, 0.0001, 0.001 and 0.005 (from top to bottom).

The burn fluence dependence of the shape of hole-burned spectra is more apparent in Fig. 13 where the spectra of Fig. 12 are normalized to the same hole depth. In the short burn time limit, the ZPH width was  $2\gamma$ , which is also observed for the spectra corresponding to ZPH depths of 2 and 14 %. The ZPH of the spectra obtained for higher burn fluences are significantly broader. This effect is called saturation broadening and occurs when electronic transitions at  $\omega_B$  are significantly bleached and HB of electronic transitions close to  $\omega_B$  (i.e. those absorbing via their Lorentzian wings) becomes more effective. Thus, determination of ZPL linewidth  $\gamma$  should be based on shallow holes with a fractional hole depth  $< 10 \%$  (Lee et al., 1989). Furthermore, for

lower burn fluences the intensities of real- and pseudo-PSBH are almost comparable. With increasing burn fluence, however, there is a considerable gain in intensity for the pseudo-PSBH while its shape remains unchanged. This effect may lead to some uncertainty when determining the Huang-Rhys factor  $S$  from PSBH intensity of hole-burned spectra, especially, because PSBH may not be discernible in the short burn time limit for weak coupling (see upper two spectra in Fig. 12). Nevertheless,  $S$  can be obtained from the saturated hole depth and / or from a thorough theoretical analysis of the burn fluence dependence.

Normalized line-narrowed fluorescence spectra calculated for different excitation frequencies within the IDF are shown in Fig. 14. The shape of the IDF is given on top for comparison. As observed for the corresponding hole-burned spectra in Fig. 11, the shape and intensity of the phonon wing of the FLN spectrum exhibits a remarkable excitation frequency dependence. This effect was first reported by Kikas (1978) and must not be interpreted as a variation of the Huang-Rhys factor  $S$  with  $\omega_E$ . The phonon wing of the spectrum with  $\omega_E = 50 \text{ cm}^{-1}$  is broad and quite structureless compared to the PSBH of the corresponding hole-burned spectra shown in Fig. 11. In contrast to this, the phonon wing is clearly resolved in the spectra with  $\omega_E$  of 0 and  $-50 \text{ cm}^{-1}$ . Despite the overlap of real- and pseudo-PSB on the low-energy side of the ZPL, the shape of the phonon wing in FLN spectra is similar to the PSBH shape if  $\omega_E$  is located within the low-energy wing of the IDF. As for HB, this is the result of a decreasing number of electronic transitions within the IDF that can be excited non-resonantly. Unfortunately, the ZPL possessing a width of  $2\gamma$  is usually significantly contaminated with scattered laser light in experimentally obtained FLN spectra because it is coincident with  $\omega_E$ . This shortcoming precludes a thorough determination of the Huang-Rhys factor  $S$  while FLN spectroscopy may provide valuable information on the one-phonon profile if  $S$  is known from independent experiments. Note, that in theoretical simulations an increase/ decrease in  $S$  can always be compensated for by a narrowing/ broadening of the one-phonon profile if analysis is simply based on the phonon wing.

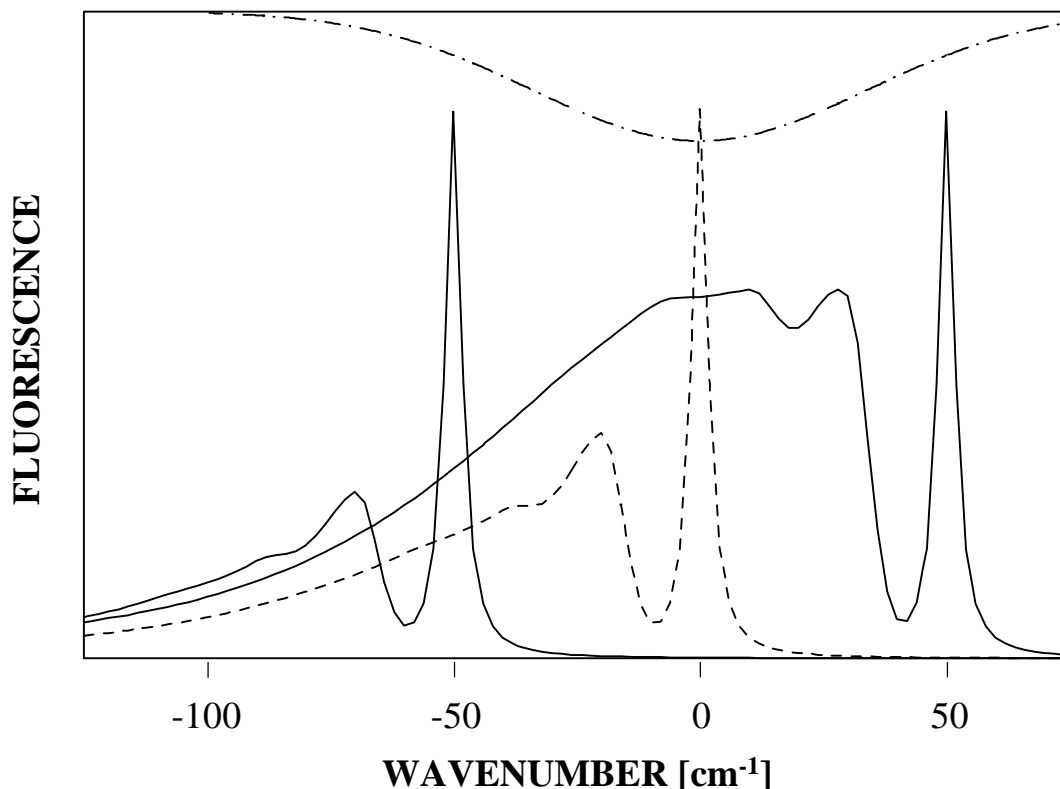


Figure 14. Low-temperature line-narrowed fluorescence spectra calculated according to Eq. 20 for the model system defined in Table 1 and excitation frequencies  $w_E$  of  $-50$ ,  $0$ , and  $+50$   $\text{cm}^{-1}$  within the IDF profile. The IDF profile (dashed-dotted line) is shown for comparison. The line-narrowed fluorescence spectrum for an excitation frequency  $w_E$  of  $0$   $\text{cm}^{-1}$  is given by a dashed line for ease of inspection.

In summary, it was demonstrated that line-narrowing spectroscopies permit a quantitative assessment of homogeneous linewidths as well as parameters of electron-phonon coupling, which are masked by inhomogeneous broadening in conventional (non-line-narrowed) spectra of pigment-protein systems. Model calculations establish, however, that the shape of line-narrowed spectra depends on a number of experimental parameters. Therefore, the experimental conditions have to be carefully chosen in order to prevent systematic errors. Nevertheless, a combination of different types of line-narrowing experiments, theoretical analysis and verification of the results using non-line-narrowing spectroscopies appears to be the most reliable approach for a thorough characterization of electron-phonon coupling in pigment-protein complexes.

#### 2.4.5 Calculation Programs

Calculation programs to simulate the low-temperature non-line-narrowed

fluorescence (Eq. 11), HB (Eqs. 18 and 19) and FLN spectra (Eq. 20) as well as the inhomogeneously broadened fluorescence spectrum at arbitrary temperatures (Eq. 15) were written in Mathematica 2.2.1. The infinite sums were cut at R-values sufficient to account for at least 99 % of the full absorption and fluorescence intensity at a given temperature, respectively. Most calculations of this study were carried out for a temperature of 4.2 K where a summation up to R=5 for S=0.9 (see Chapter 4) assured that 99.99 % of the full intensity is considered. In Eqs. 11 and 15 the proper folding of the narrow ZPL is omitted. Rather, the inhomogeneously broadened ZPL is taken to be a Gaussian having a width of  $\Gamma_{inh}$ . This approximation requires that  $\Gamma_{inh} \gg \gamma$ . This appears to be justified for values of  $\gamma=0.073 \text{ cm}^{-1}$  and  $\Gamma_{inh} \sim 80 \text{ cm}^{-1}$  for the lowest (fluorescing) state of LHC II at 4.2 K as determined in Chapter 4. When calculating FLN spectra (Eq. 20), only terms for R>0 are considered because the ZPL is obscured by scattered laser light in the experimental data (see Chapter 4). Finally, guided by the previous work of Hayes et al. (1994) and the experimental data of this study (see Chapter 4) the one-phonon profile  $I_1$  is generally assumed to be asymmetric with a Gaussian shape at its low-energy wing and a Lorentzian shape at its high-energy wing. Then, the full profile has a peak frequency of  $\omega_m$  and a width of  $\Gamma = \Gamma_G/2 + \Gamma_L/2$ .

## **2.5 Selected Applications**

HB has been used to determine the inhomogeneous and homogeneous broadenings of the  $Q_y$ -absorption bands of many photosynthetic complexes (for a review see Reddy et al., 1992). As to the homogeneous widths and corresponding total dephasing times  $T_2$ , it has already been discussed in Chapter 2.4.4 that the homogeneous width is directly related to the holewidth of shallow holes with fractional absorption changes of less than 10 %. For example, Rätsep et al. (1999) studied the temperature dependence of the widths of holes burned into the lowest three (823, 825 and 827 nm) absorption bands of the Fenna-Mathews-Olson (FMO) complex of *Chlorobium tepidum*. According to their analysis, the former two bands are characterized by lifetimes ( $T_1$ ) of 37 and 117 ps due to downward EET while the homogeneous width of the lowest (827 nm) band is dominated by pure dephasing due to coupling to

the heterogeneous protein environment. The latter results are in good agreement with those of time-resolved experiments using the technique of accumulated photon echo (Louwe and Aartsma, 1997).

Inhomogeneous broadening can be studied using zero-phonon hole (ZPH) action spectroscopy, i.e. a series of ZPH is burned across an absorption spectrum of a pigment-protein complex applying constant burn fluence. As discussed in Chapter 2.2.2, the HB efficiency increases with increasing excited state lifetime  $T_1$ . Thus, for a constant burn fluence HB is most efficient for ZPH associated with the energetic level having the longest lifetime  $T_1$ , i.e. the lowest state. As a result, the ZPH action spectrum basically reflects the inhomogeneously broadened zero-phonon absorption profile of the lowest state of a given pigment-protein complex. For example, ZPH action spectroscopy led to identification and characterization of the lowest energy levels of the LH2 (B800-850) antenna complex of *Rhodospseudomonas acidophila* (Wu et al., 1997) as well as of the LH1 (B875) antenna complex of *Rhodobacter sphaeroides* (Wu et al., 1998). In particular, the lowest state of the latter complex was found to be located at 896 nm and to carry an inhomogeneous width of  $\sim 150 \text{ cm}^{-1}$ . The location of the lowest energy level can serve as a benchmark for theoretical calculations of the excited state electronic structure (see e.g. Wu et al., 1997; T. Renger et al., 2000).

HB spectroscopy can also be used to gauge the strength of Chl-Chl interactions. In this case, analysis can be based on satellite hole structure as well as on the pressure dependence of absorption bands and hole features. As to the first, it has already been discussed in Chapter 2.2.2 that NPHB involves a more or less persistent structural change of the pigment-protein system induced upon electronic excitation. Thus, in systems of strongly coupled pigments, HB in any excitonic level should elicit responses from the other exciton levels. These responses would appear as persistent satellite holes at the energetic positions of the excitonic levels. This effect has been observed, for example, for the FMO complex of *Prosthecochloris aestuarii* (Johnson and Small, 1991). Furthermore, HB of the lowest energy  $Q_y$ -state (P.) of the special pair of BChl *b* molecules of *Rhodospseudomonas viridis* (Reddy et al., 1993)

produces a large response from the upper special pair state ( $P_+$ ), which is visible as an intense hole. As a consequence, the satellite hole structure could be used to assign the position and relative intensity of the absorption band of  $P_+$ . Quite recently, high pressure has been combined with low-temperature absorption and HB spectroscopies in order to assess the strength of excitonic couplings in photosynthetic complexes (see e.g. Reddy et al., 1996 and references therein). Briefly, pressure shift rates for the  $S_1$ -states of isolated chromophores in glass, polymer and protein hosts are observed in the range of  $-0.05$  to  $-0.15$   $\text{cm}^{-1}/\text{MPa}$  (isotropic compressibilities ( $\kappa$ ) for glasses and proteins are as low as  $0.1$   $\text{GPa}^{-1}$ ). If such shift rates are observed for photosynthetic complexes, pigment-protein interactions are expected to be the dominant factor for the pressure dependence. It can be assumed, however, that pressure alters the center-to-center distances of strongly interacting pigments resulting in an increase in excitonic splitting with increasing pressure. Thus, a shift rate with absolute values higher than  $\sim 0.2$   $\text{cm}^{-1}/\text{MPa}$  for a photosynthetic complex indicates that excitonic interactions may affect the pressure dependence.

The electron-phonon coupling of a number of photosynthetic complexes has already been investigated by HB. In general, it has been shown that the electron-phonon coupling of antenna complexes is weak with Huang-Rhys factors  $S \ll 1$  and mainly associated with delocalized protein vibrations with frequencies in the  $\sim 20$ - $30$   $\text{cm}^{-1}$  range (for a review see e.g. Reddy et al., 1992). In particular, the theory discussed in Chapter 2.4 has been successfully applied to simulate 4.2 K hole spectra of a bacterial reaction center (Lyle et al., 1993) as well as the temperature dependence of absorption profiles up to 200 K (Hayes et al., 1994).

FLN can, in principle, provide the same information as spectral HB. As discussed in Chapter 2, however, the analysis of line-narrowed fluorescence spectra is often hindered by the fact that the ZPL is significantly contaminated with scattered laser light. For example, Avarmaa and Rebane (1985) determined the intramolecular vibrational frequencies of Chl but not their coupling strengths  $S$  using FLN spectroscopy. Later, Gillie et al. (1989) obtained the corresponding  $S$ -factors in spectral HB experiments. Comparison

of the results of both studies establishes that most of the intramolecular vibrational frequencies of Chl obey mirror symmetry in absorption and fluorescence, respectively (see Chapter 2.4.1).

## **3 Materials and Experimental Methods**

### **3.1 Sample Preparation**

Most of the experiments reported in this study were performed using samples of solubilized (dissolved) trimeric LHC II. Comparative measurements were carried out using samples of aggregated LHC II and purified CP29. All samples and buffer solutions were prepared by Dr. K.-D. Irrgang and coworkers.

#### **3.1.1 Trimeric LHC II**

LHC II preparations were isolated by solubilization of salt washed PS II membrane fragments of spinach in the presence of  $\beta$ -dodecyl maltoside ( $\beta$ -DM) and separation by sucrose density gradient centrifugation as described by Irrgang et al. (1988). The  $Q_y$ -absorption spectrum at room temperature exhibited two bands with maxima at  $(652 \pm 1)$  nm and  $(675 \pm 1)$  nm. The room temperature CD spectrum was identical to that of the trimer complex reported by Peterman et al. (1996). A Chl *a*/Chl *b* ratio of  $1.35 \pm 0.05$  was determined using the method of Porra et al. (1989).

The polypeptide composition was checked by SDS / urea / PAGE using the procedure of Irrgang et al. (1988) in combination with silver staining and immunoblotting experiments as described in detail by Vasil'ev et al. (1997a). Besides the LHC  $b_{1-3}$  gene products of the major light-harvesting complex, the  $\beta$ -DM solubilized LHC II also contains the minor Chl *a/b* binding proteins CP 14/15, CP 22, CP 24 and CP 26 known to be associated with the antenna system of photosystem II. According to densitometrical scanning of silver-stained poly-acrylamide gels, 87.4 % of the apoproteins could be ascribed to Lhcb 1-3 proteins and 12.6 % to the minor pigment-protein complexes, mainly CP 24 and CP 26.

To ensure good optical quality for low-temperature measurements the samples were diluted in a glass forming buffer solution containing 0.025 % w/v  $\beta$ -DM and 70 % w/v glycerol as well as 30 mM MES-NaOH, pH 6.5, 15 mM NaCl, 5 mM  $MgCl_2$ . In addition, the amount of detergent in the latter buffer solution is sufficiently high to prevent non-desirable aggregation of trimeric LHC II as was

shown by Vasil'ev et al. (1997b).

As an example, a total chlorophyll concentration of 0.2 mg Chl/ ml resulted in an optical density (OD) of 2 at 676 nm and 4.2 K for a sample contained in a 1 mm cuvette.

### **3.1.2 Aggregated LHC II**

Aggregation of trimeric LHC II complexes was induced by dialyzing solubilized samples for 48 h at 4 °C in the dark against a detergent-free buffer solution containing 30 mM MES-NaOH, pH 6.5, 15 mM NaCl, 5 mM MgCl<sub>2</sub>. The procedure was described in detail by Vasil'ev et al. (1997a; 1997b).

Pigment concentration and polypeptide composition was checked as described for (solubilized) trimeric LHC II in the preceding chapter. As for the latter complex, 87.4 % of the apoproteins could be ascribed to Lhcb 1-3 proteins and 12.6 % to the minor pigment-protein complexes CP 14/15, CP 22, CP 24 and CP 26.

For low-temperature experiments aggregated LHC II was diluted in a (detergent-free) glass forming buffer solution containing 70 % w/v glycerol as well as 30 mM MES-NaOH, pH 6.5, 15 mM NaCl, 5 mM MgCl<sub>2</sub>. As for solubilized LHC II, a total chlorophyll concentration of 0.2 mg Chl/ ml resulted in an optical density (OD) of 2 at 676 nm and 4.2 K for a sample contained in a 1 mm cuvette.

### **3.1.3 CP29**

PS II membrane fragments were isolated from spinach chloroplasts according to the procedure described by Berthold et al. (1981) with modifications as in M. Völker et al. (1985) followed by resuspension and dilution to 0.2 mg Chl/ml in 0.8 M TRIS-HCl, pH 8,35 under room light for 30 min. CP29 was then isolated and purified following a modified protocol of Henrysson et al. (1989) in the presence of 2 mM benzamidine (Sigma) and 1 mM Pefabloc (Merck) as protease inhibitors. Sulfobetaine 12 (SB 12) was used instead of Sulfobetaine 14 (SB 14) and the column equilibration and gradient buffers contained 0.1 % w/v SB 12 and 0.05 % w/v β-DM. Chromatography was run with a CM-Sepharose Fast Flow column under dim green light at 4°C. One to

two rechromatographies were necessary to obtain purified CP29. The purified pigment-protein complex was concentrated by centrifugation in Centriprep 10 tubes to the desired Chl concentration.

The purity of the pigment-protein complex was analyzed by SDS / urea / PAGE using a 6 % polyacrylamide stacking and a 14 % polyacrylamide separating gel. Both gels contained 0.1 % w/v SDS and 5 M urea and the buffer system of Laemmli (1970) was applied. Western blotting was carried out as described previously (Towbin et al., 1979) using monoclonal antibodies (Pascal et al., 1999). Gels were stained with silver as in Heukeshoven and Dernick (1985). The analysis revealed that at least 98 % of the total protein can be ascribed to CP29 while a contribution of 1-2 % may be due to CP 24 and CP 26 (Pascal et al., 1999).

Chlorophyll *a* and *b* were determined according to Porra et al. (1989) in 80 % v/v acetone. Carotenoids were spectroscopically analyzed by measuring the absorbance at 470 nm using the extinction coefficients of Wellburn and Lichtenthaler (1984) and Davis (1976). Furthermore, the pigment composition was analyzed by RP-HPLC. The Chl *a*/Chl *b* ratio was found to be  $2.85 \pm 0.04$ . Based on a total of eight chlorophylls (Giuffra et al., 1996) each CP29 protein contains 5.9 Chl *a*, 2.1 Chl *b*, 0.6 lutein, 0.6 neoxanthin and 0.7 violaxanthin.

### **3.2 Experimental Methods and Instrumentation**

The following chapters describe the basic methods and equipment of HB and fluorescence experiments as they were routinely performed. Results concerning sample and data quality are discussed in Chapter 4.

#### **3.2.1 Spectral Hole-Burning**

Absorption and HB experiments were carried out in three different modes: a) HB with detection of absorption and absorption changes up to a resolution of  $0.2 \text{ cm}^{-1}$  (Chapter 3.2.1.1), b) HB in the fluorescence excitation mode, i.e. burning and scanning with highly monochromatic laser light (linewidth of  $0.001 \text{ cm}^{-1}$ ) and broad band detection of the excited fluorescence signal (Chapter 3.2.1.2), as well as c) absorption and HB experiments with a resolution of up to  $0.2 \text{ cm}^{-1}$  combined with high pressures up to 500 MPa

(Chapter 3.2.1.3).

### 3.2.1.1 Hole-Burning Experiments

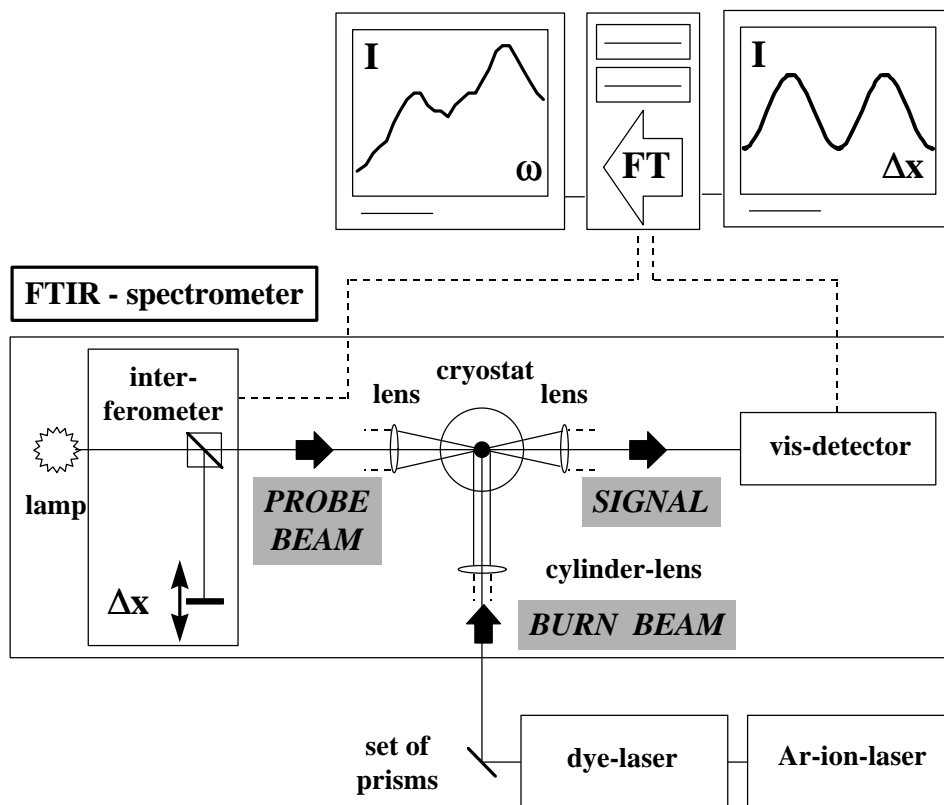


Figure 15. Setup for lower resolution hole-burning experiments.

The HB experiments for lower resolution ( $> 0.2 \text{ cm}^{-1}$ ) measurements were first described by Reddy et al. (1993). The setup used is schematically shown in Fig. 15. A Coherent CR 699-21 ring dye laser pumped by a 6 W Coherent Innova argon ion laser was employed as the burn laser. This laser system is characterized by a linewidth of  $\sim 0.05 \text{ cm}^{-1}$  and provides burn intensities ( $I_B$ ) up to  $500 \text{ mW/cm}^2$ . The burn laser beam passes a set of optical prisms and is then focused to the sample position by a cylinder lens resulting in a focal line perpendicular to the laser beam. This assures that a test beam oriented perpendicularly to the burn laser beam probes an area excited by an almost constant burn intensity. A Bruker IFS 120 HR Fourier transform infrared (FTIR) spectrometer is used to record (read) the preburn and postburn absorption spectra. A Tungsten lamp within the FTIR spectrometer provided the spectrally broad test beam. The test beam passes a Michelson interferometer so that it

interferes with itself. If the position of the reflecting mirror is changed by  $\Delta x$ , the test beam intensity  $I(\Delta x)$  oscillates due to subsequent periods of constructive and destructive interference.  $I(\Delta x)$  is related to the test beam spectrum  $I(\omega)$  by a Fourier transformation. If the sample absorbs a certain frequency, the contribution of the latter to  $I(\Delta x)$  is removed. Thus, the absorption spectrum of a sample  $A(\omega)$  can be calculated from the detected signal  $I(\Delta x)$  via the numerical, fast Fourier transformation. A Janis 8-DT convection cooling liquid helium cryostat maintained the sample temperature at 4.2 K. The sample was contained in a cuvette of 10 mm optical pathlength. Therefore, the total Chl concentration was adjusted to 0.007 mg/ml in order to yield an optical density of the sample of  $\sim 0.7$  at 676 nm and 4.2 K. Burn intensities ( $I_B$ ) and times ( $\tau_B$ ) or burn fluences ( $I_B\tau_B$ ) as well as read resolutions are given in the figure captions.

### 3.2.1.2 Fluorescence Excitation Mode

High-resolution HB was performed in the fluorescence excitation mode. This method utilizes the fact that the fluorescence signal is proportional to the absorption at the excitation wavelength. HB leads to a loss of absorption and, therefore, to a decrease in the fluorescence signal excited at the burn wavelength. This principle has two major advances for high-resolution experiments: First, the hole growth during the burn process can be directly monitored and adjusted by simultaneously measuring the drop of the excited fluorescence signal in order to prevent effects from saturation broadening. Second, the hole spectrum can be recorded by subsequently scanning the hole with a narrow band laser and monitoring the fluorescence signal excited at each wavelength. The fluorescence, however, can be detected in a broad wavelength range. Therefore, the resolution for burning and reading is determined by the narrow laser linewidth.

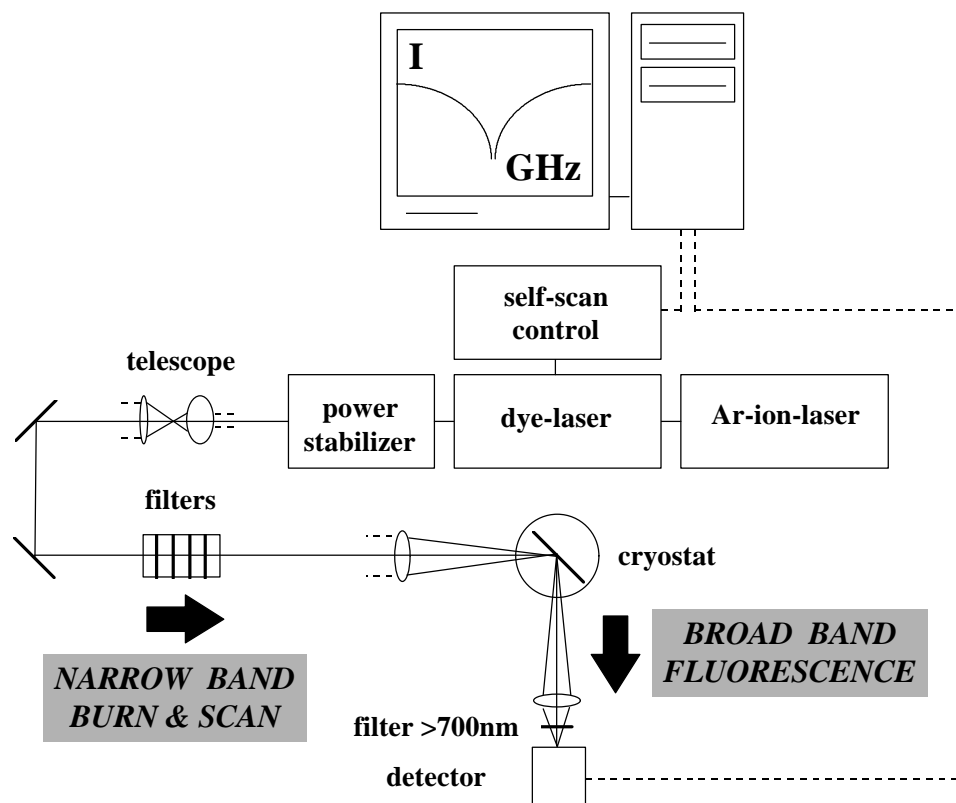


Figure 16. Setup for hole-burning experiments in the fluorescence excitation mode.

The setup used for HB in the fluorescence excitation mode (see Fig. 16) was first described by Kim et al. (1995). The above laser system with all intracavity etalons inserted was used to burn and scan the hole spectra. In this case, the resolution for burning and reading is determined by the laser linewidth of  $< 30 \text{ MHz}$  ( $0.001 \text{ cm}^{-1}$ ). A LS 100 power stabilizer (Cambridge Research and Instrumentation) prevented fluctuations of the laser intensity higher than  $\sim 5\%$ . Subsequently, the laser beam was expanded by a telescope and passed a series of neutral density filters. Thus, the laser intensities could be adjusted to  $15\text{-}55 \mu\text{W}/\text{cm}^2$  for burning and attenuated by a factor of 10-50 for reading. Fluorescence was detected and processed by a GaAs photomultiplier tube (RCA C31034) and a photon counter (SR-400, Stanford Research Instruments). Scattered laser light was rejected by long wavelength pass filters allowing for broad band fluorescence detection above 700 nm. The decrease of the fluorescence signal during the burn process was detected simultaneously in order to assure that the fractional hole depths were typically  $< 10\%$  and, therefore, virtually free from saturation broadening. A Janis 10-DT

convection cooling liquid helium cryostat combined with a temperature controller (Lakeshore Cryotronics, Model 330) was used for temperature-dependent studies. An additional vacuum pump was connected to the sample chamber in order to reach temperatures below 4.2 K. After the temperature diode reading reached the pre-set temperature, the sample was allowed to equilibrate for 15 minutes prior to initiating fluorescence excitation measurements. The sample was contained in a gelatin capsule of 5 mm optical pathlength. The optical density of the sample was adjusted to ~ 0.1 at 676 nm and 4.2 K.

### 3.2.1.3 High-Pressure Apparatus

The high-pressure apparatus that was first described by Chang et al. (1994) can be combined with the HB setup for lower resolution absorption and HB experiments (see Chapter 3.2.1.1). High pressures of up to 800 MPa were generated by a three-stage hydraulic compressor (Model U11, Unipress Equipment Division, Polish Academy of Sciences). Helium gas was used as the pressure transmitting medium. The compressor was connected to a specially designed high-pressure cell through a flexible thick-walled beryllium copper capillary (outer diameter / inner diameter = 3.0 mm / 0.3 mm). The sample was contained in an elastic gelatin capsule of 5 mm optical pathlength and then housed in the high-pressure cell. Three sapphire windows with a thickness of 4 mm provided optical access to the cell for burn laser and test beam. A specially designed Janis 11-DT cryostat was used for cooling of the high-pressure cell. For studies at higher temperatures than 4.2 K, a Lakeshore temperature controller (Model 330) was used to stabilize the temperature.

When performing high-pressure experiments at low temperatures it has to be kept in mind that helium, the pressure transmitting medium, solidifies e.g. at 18, 75 and 800 MPa for temperatures of 4.2, 12 and 55 K, respectively. Therefore, the pressure dependence of the  $Q_y$ -absorption spectrum of LHC II was studied up to ~ 500 MPa at 77 K. High-pressure HB was performed applying pressures up to ~ 70 MPa at 12 K.

In order to confirm that pressure-induced structural changes are elastic,

absorption and hole spectra were routinely recorded before pressure was applied and after it was released, respectively.

### 3.2.2 Fluorescence Experiments

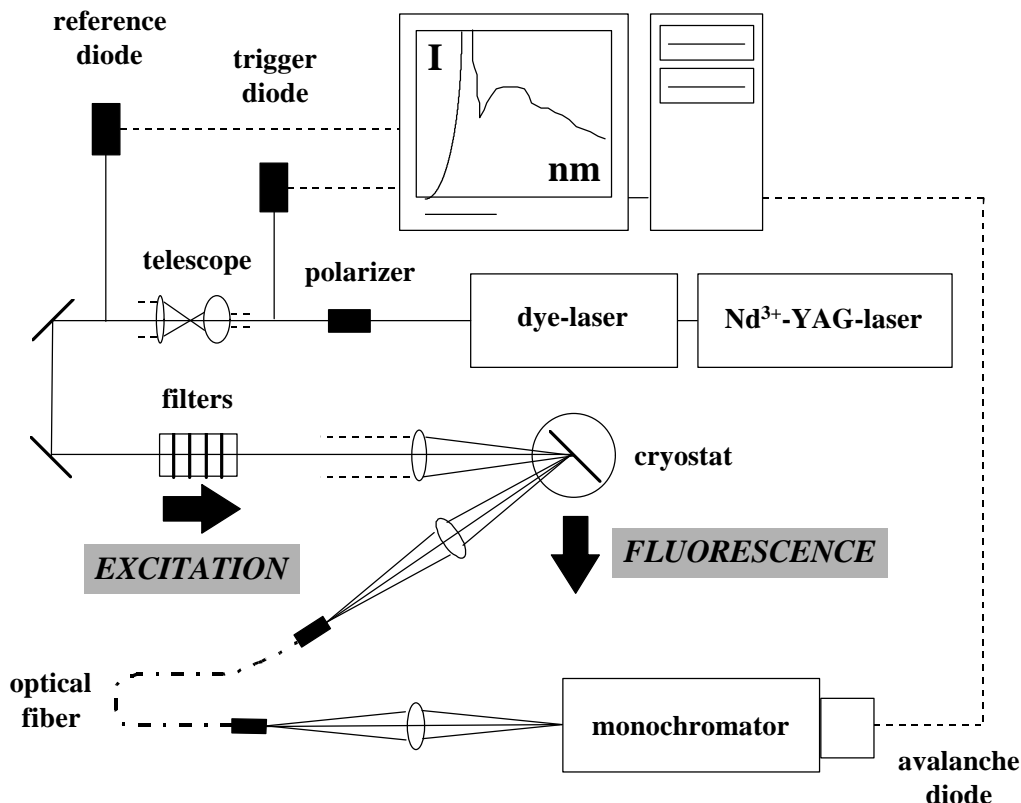


Figure 17. Setup for fluorescence experiments.

Fluorescence experiments employed (see Fig. 17) a Nd<sup>3+</sup>-YAG laser pumped dye laser (Laser Analytical Systems LDL 105), which delivered excitation pulses of about 3 ns duration, a repetition rate of 10 Hz and a spectral width of  $\sim 0.002$  nm. A polarizer is employed to minimize contamination of the laser beam with spontaneous emission of the laser dye to a ratio of 1:1000. Two beam splitters direct part of the excitation signal to diode detectors providing a trigger (*vide infra*) and a reference signal, respectively. The latter signal is used to account for fluctuations in excitation intensity which are typical for dye lasers. The remaining laser beam is expanded by a telescope and passes a set of neutral density filters in order to adjust the excitation intensity. Focusing of the laser beam and collection of the fluorescence signal was carried out as in Schödel et al. (1996). Briefly, the laser beam was focused by an objective of 140 mm focal length. The sample was placed slightly out of focus to obtain a

relatively broad excitation spot with a diameter of about 100  $\mu\text{m}$ .

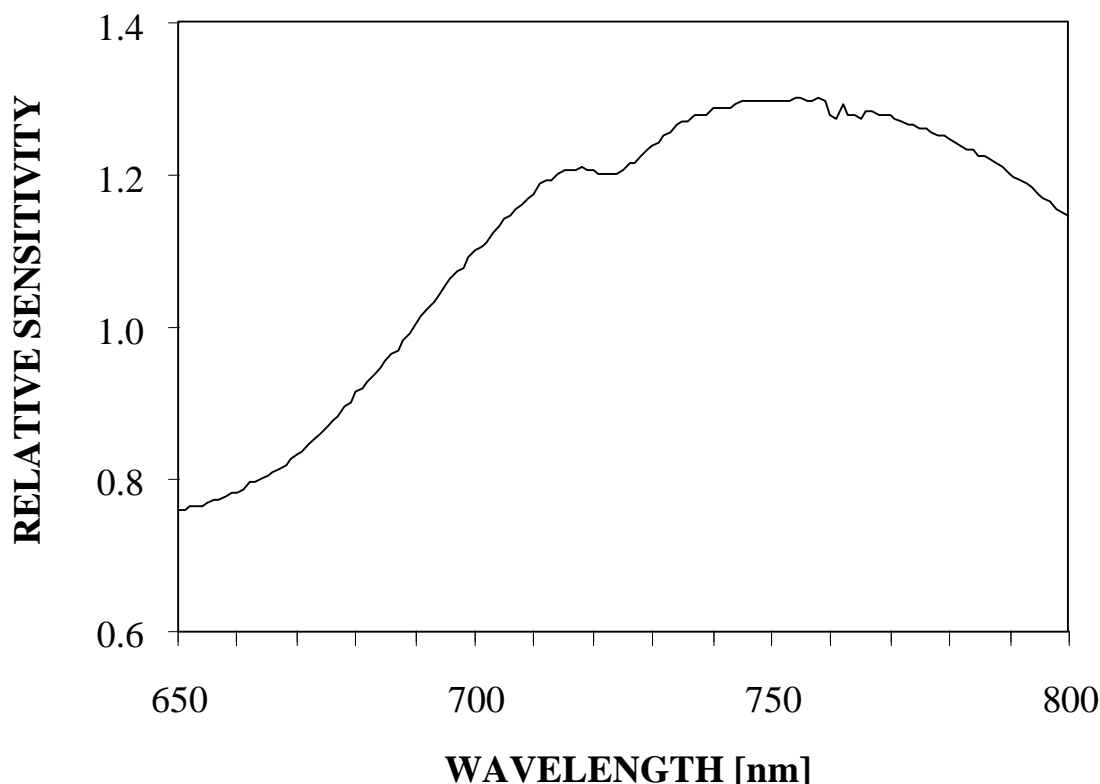


Figure 18. Sensitivity of the detection branch of the setup for fluorescence experiments as obtained measuring the emission spectrum of a calibrated wolfram lamp.

Another objective of 140 mm focal length was used to display the fluorescence signal onto a pinhole that selected emission from the center of the excitation spot. This arrangement assured that the measured fluorescence signal is related to a well-defined excitation intensity, *vide infra*. A double monochromator (GDM 1000, Carl Zeiss Jena) and an avalanche diode amplifier module (Analog Modules Inc., type 712-A4) were used for spectral analysis of the fluorescence. Reference and fluorescence signal were delivered into a boxcar integrator that was triggered by the laser beam and operated in the gated mode (gate width of 10 ns). Finally, the data were read out by a personal computer. The experimental data were corrected for the spectral sensitivity of the detection branch as obtained measuring the emission spectrum of a calibrated wolfram lamp (see Fig. 18). The sample temperature was maintained and stabilized using an Oxford Helium flow Cryostat (Optistat) combined with an Oxford temperature controller. The sample was allowed to equilibrate for 20 minutes prior to fluorescence measurements.

### *3.2.2.1 Non-Line-Narrowed Fluorescence Spectra*

When measuring non-line-narrowed fluorescence spectra the resolution of the detection branch was 0.5 nm. The applied excitation intensity was approximately  $10^{13}$  photons per  $\text{cm}^2$  and pulse in order to avoid non-linear (intensity-dependent) effects (Schödel et al., 1996). Unless otherwise noted the samples were contained in cuvettes of 0.01 mm optical pathlength. The resulting optical density of 0.02 at 676 nm and 4.2 K assured that the results remain virtually unaffected by reabsorption (see Chapter 4.5.2).

### *3.2.2.2 Line-Narrowed Fluorescence Spectra*

Line-narrowed fluorescence spectra were measured using a spectral resolution of 0.2 nm. The experimental conditions were carefully chosen in order to avoid possible systematic errors, i.e. contamination with scattering artifacts (see Chapter 4.6.1), HB effects (see Chapter 4.6.2) and effects owing to reabsorption (Chapter 4.6.3). Routinely, an excitation intensity of approximately  $10^{13}$  photons per  $\text{cm}^2$  and pulse was employed. The ZPL of the FLN spectra was obscured by scattered laser light. In order to permit a subtraction of its contribution the spectral characteristics of the scattered light of the excitation source was measured by placing a reflecting, non-emitting surface at the position of the sample. This spectrum was normalized to the high-energy wing of the FLN spectra and then subtracted to yield the phonon contribution to the spectra. Quantitatively, the excitation signal was suppressed by about three orders of magnitude 1 nm beside the excitation wavelength. The samples were contained in cuvettes of 0.50 mm optical pathlength corresponding to an optical density of 1.00 at 676 nm and 4.2 K. It will be shown in Chapter 4.6.3 that this optical density assured that the fluorescence signal is virtually free from reabsorption.

## 4 Experimental Results

### 4.1 Hole-Burned Spectra of LHC II

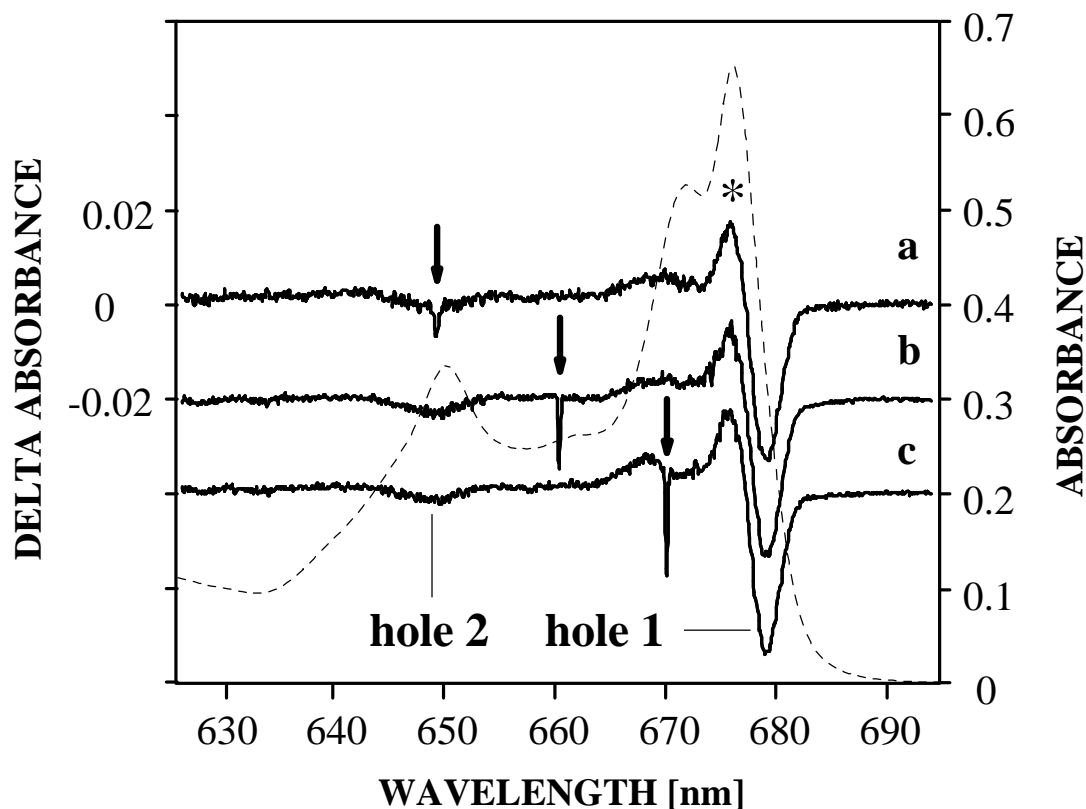


Figure 19. The 4.2 K absorption spectrum (see dashed line) as well as three typical hole-burned spectra of trimeric LHC II (see full lines) obtained for burn wavelengths of a) 648.5, b) 660.0 and c) 670.0 nm (see arrows), a burn fluence of  $80 \text{ J/cm}^2$  and a read resolution of  $4 \text{ cm}^{-1}$ . The spectra are given equidistant offsets of 0.02. Spectrum a is twice enlarged. The feature indicated by the asterisk is the anti-hole of hole 1.

As already mentioned in Chapters 1.2 and 2, the 4.2 K  $Q_y$ -absorption spectrum of trimeric LHC II shown in Fig. 19 is quite structureless with only four partially resolved bands at 649.5, 661.4, 671.3, and 676.1 nm. HB can be expected to significantly improve the resolution of optical spectroscopy of LHC II at 4.2 K. Hole-burned spectra were obtained with burn wavelengths ( $\lambda_B$ ) between 640 and 684 nm. The changes in the absorption spectrum produced by HB were persistent on the time scale of the experiment, but completely reversible upon temperature increase to about 180 K. These observations indicate that the generated absorption difference spectra are due to persistent NPHB. The ZPH burning efficiencies for  $660 \text{ nm} \leq \lambda_B \leq 674 \text{ nm}$  were more than an order of magnitude lower than for  $\lambda_B \geq 674 \text{ nm}$ . A further decrease of the burn

efficiencies by about a factor of 5 was observed for 640 nm  $\leq \lambda_B \leq$  655 nm. Therefore, hole-burned spectra obtained for burn wavelengths lower and higher than 674 nm will be presented separately.

#### **4.1.1 Hole-Burning with Burn Wavelengths Lower than 674 nm**

The hole-burned spectra a, b and c of Fig. 19 were obtained with  $\lambda_B =$  648.6, 660.0 and 670.0 nm, respectively, and a burn fluence of  $\sim 80$  J/cm<sup>2</sup>. They show structure that is typical of spectra obtained with 640 nm  $\leq \lambda_B \leq$  674 nm. First, there is the ZPH coincident with  $\lambda_B$  which is indicated by an arrow. Second, there is a broad and intense hole near 680 nm which is labeled as hole 1. Third, there is a broad hole near 648 nm with a width of  $\sim 125$  cm<sup>-1</sup>, labeled as hole 2, which is close to the maximum of the 650 nm absorption band. The positive feature labeled by the asterisk is the blue-shifted anti-hole of hole 1. These general features have already been observed in a previous HB study by Reddy et al., (1994). The observation of hole 1 at 679.3 nm for all burn wavelengths suggests that it is due to HB in a low-energy state(s), which is rapidly populated from higher states by efficient EET.

#### **4.1.2 Constant Fluence Hole-Burning in the Low-Energy Region**

Constant fluence hole-burning (ZPH action) spectroscopy with  $\lambda_B \leq 674$  nm was employed in order to further characterize the spectral position and inhomogeneous width of the low-energy state(s) represented by hole 1. Fig. 20 shows the ZPH action spectrum obtained with a constant burn fluence of 3.6 J/cm<sup>2</sup> and a read resolution of 0.3 cm<sup>-1</sup>. Thus, the read resolution is an order of magnitude higher while the burn fluence is about a factor of 5 lower than those used by Reddy et al. (1994). The burn conditions employed result in fractional hole depths less than 17 % (see Table 2). Therefore, the fractional depth is almost a factor of 3 lower than that obtained by Reddy et al. (1994) and assures that the results are not significantly affected by saturation effects. The action spectrum is approximately Gaussian with a width (FWHM) of  $(90 \pm 10)$  cm<sup>-1</sup> and is centered at  $(678.2 \pm 0.2)$  nm, which is 1.3 nm lower than the value reported by Reddy et al (1994). The observation of narrow ZPH establishes that hole 1 of Fig. 19 is inhomogeneously broadened, see next chapter. Furthermore, no satellite holes building on the ZPH of the action

spectrum were observed indicating that the low-energy state(s) is largely uncorrelated with those of the higher energy states.

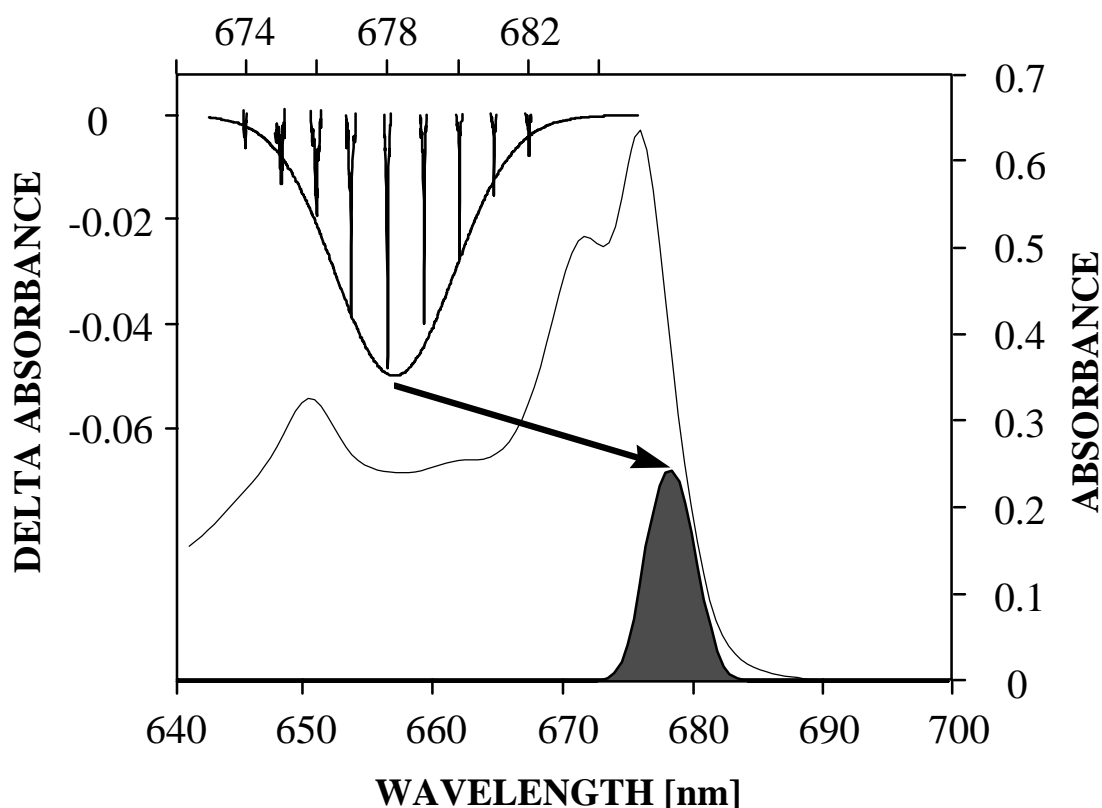


Figure 20. The 4.2 K absorption and ZPH-action spectrum (see upper, left corner) of trimeric LHC II. The action spectrum was generated with a constant burn fluence of  $3.6 \text{ J/cm}^2$  and a read resolution of  $0.3 \text{ cm}^{-1}$ . Its location within the 4.2 K absorption spectrum is indicated by the hatched profile.

The ZPH widths (uncorrected for read resolution) for burn wavelengths between 674 and 682 nm range from  $2.5 \text{ cm}^{-1}$  to  $0.5 \text{ cm}^{-1}$  (see Table 2 in Chapter 6.2). The observation of broader ZPH at the high-energy wing of the action spectrum suggests that it is contributed to by higher energy states. Nevertheless, the latter contribution should be small because of their much shorter lifetimes  $T_1$  due to downward EET. As discussed in Chapter 2.2.2, the burn efficiency increases significantly with increasing excited state lifetime  $T_1$ . The widths of the ZPH for  $\lambda_B \approx 679 \text{ nm}$  are close to the read resolution of  $0.3 \text{ cm}^{-1}$ . Therefore, high-resolution ( $< 30 \text{ MHz}$ ) experiments were performed in the fluorescence excitation mode in order to determine the true widths for shallow ZPH with fractional hole depth of less than 10 % and burn wavelengths between 681 and 682 nm. Holewidths of  $0.074$ ,  $0.146$ , and  $0.600 \text{ cm}^{-1}$  were

obtained based on Lorentzian fits for temperatures of 1.9, 4.7, and 9.2 K, respectively. The temperature dependence of the holewidth can be fit by an  $T^A$  power law with  $A = (1.3 \pm 0.1)$  (not shown). This dependence is the signature for spectral dynamics stemming from coupling to the glass-like TLS of the protein (see, e.g., Hayes et al., 1988a; Völker, 1989).

#### **4.1.3 Compatibility of the Low-Energy Hole Features**

For the hole spectra shown in Fig. 19 hole 1 was centered at  $(679.3 \pm 0.2)$  nm, i.e. its position was independent of  $\lambda_B$  for all  $\lambda_B$ -values  $\geq 674$  nm. The burn fluence used was  $78 \text{ J/cm}^2$ . The ZPH action spectrum of Fig. 20, with a maximum at  $(678.2 \pm 0.2)$  nm, was obtained with a much lower fluence of  $3.6 \text{ J/cm}^2$ . To investigate the source of the 1.1 nm difference between these two maxima, the burn fluence dependence of hole 1 was determined. Results are shown in frame A of Fig. 21 for  $\lambda_B = 660$  nm. For comparison the ZPH action spectrum from Fig. 20 is also shown. Burn intensities and times for the six spectra of hole 1 are given in the figure caption. The wavelength of the maximum of hole 1 decreases from  $(679.8 \pm 0.2)$  nm (top profile; burn fluence of  $7.8 \text{ J/cm}^2$ ) to  $(679.0 \pm 0.2)$  nm (bottom profile; burn fluence of  $230 \text{ J/cm}^2$ ). The fractional OD changes at the hole 1 maxima in frame A of Fig. 21 are, from top to bottom, 0.040, 0.060, 0.085, 0.11, 0.16 and 0.19.

The blue shifting of hole 1 with increasing burn fluence is more apparent in frame B. Hole a was obtained under the conditions used to obtain the results of frame A except that  $\tau_B = 30$  s, i.e. for the lowest available burn fluence. Hole b is the difference between the lowest two profiles of frame A (normalized to the same peak intensity as hole a), i.e. it represents only those electronic transitions bleached with highest available burn fluence. The maxima of holes b and a are at  $(678.4 \pm 0.2)$  nm and  $(679.8 \pm 0.2)$  nm, respectively. The latter wavelength is the red-most position of hole 1 while the former is equal, within experimental uncertainty, to the maximum of the ZPH action profile.

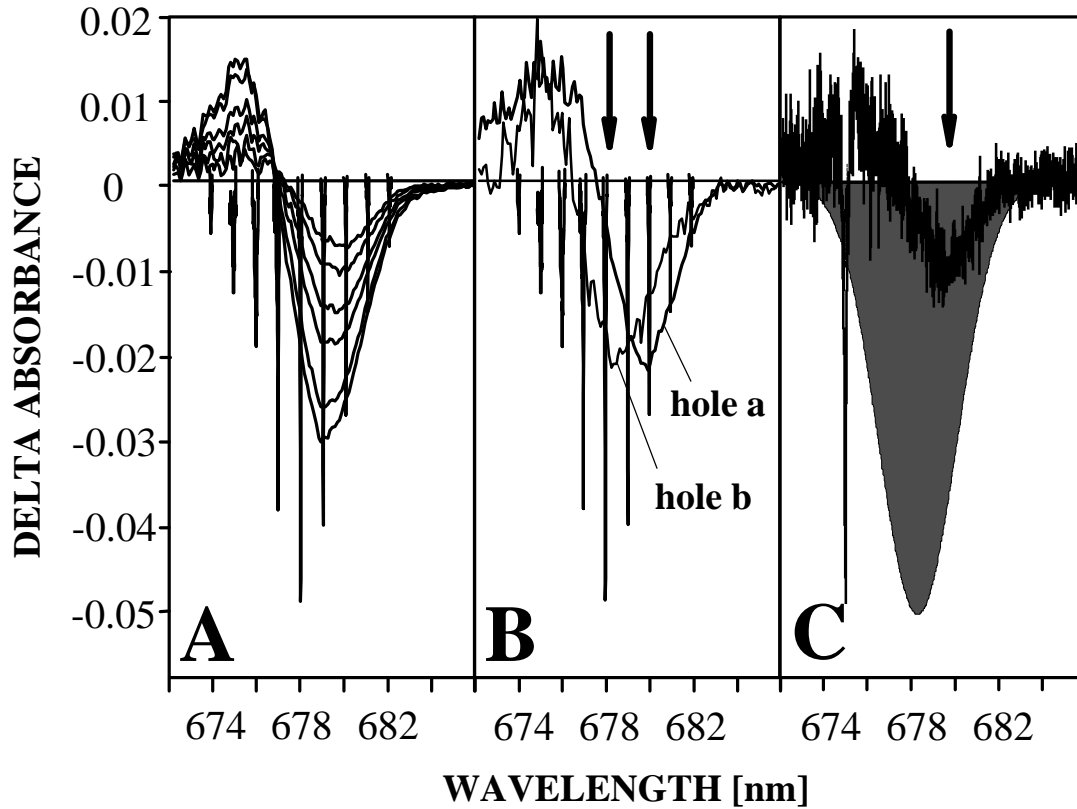


Figure 21. Comparison of different low-energy hole features of trimeric LHC II: The ZPH-action spectrum from Fig. 20 is shown along with hole 1 (see Fig. 19) obtained under different burn conditions. Frame A: Burn fluence dependence of hole 1 obtained for  $I_B = 660$  nm, a burn intensity of  $130 \text{ mW/cm}^2$  and burn times (top to bottom) of 1, 2, 5, 10, 20 and 30 min (close to saturation). The read resolution was  $4.0 \text{ cm}^{-1}$ . Frame B: Further illustration of blue-shift of hole 1. Hole a was obtained for the shortest burn time of 30 s while hole b is the difference between the lowest two hole spectra of Frame A. Holes a and b peak at  $(679.8 \pm 0.2)$  and  $(678.4 \pm 0.2)$  nm, respectively (see arrows). Frame C: Hole spectrum obtained with  $I_B = 675.0$  nm (coincident with the sharp ZPH), burn intensity =  $100 \text{ mW/cm}^2$  and burn time = 60 s. The broad hole at 679.8 nm is indicated by an arrow.

Frame C of Fig. 21 shows a hole-burned spectrum obtained with  $\lambda_B = 675.03$  nm,  $I_B = 100 \text{ mW/cm}^2$  and  $\tau_B = 60$  s that provides additional support for the red-most position of hole 1 being at  $\sim 679.8$  nm. The broad satellite hole indicated by the arrow is located at  $(679.8 \pm 0.2)$  nm. Its width, after a correction for interference from the anti-hole on the high-energy side, is  $\sim 80 \text{ cm}^{-1}$ , which is  $10 \text{ cm}^{-1}$  narrower than that of the ZPH action spectrum. The shaded gray profile in frame C is the Gaussian profile of the action spectrum.

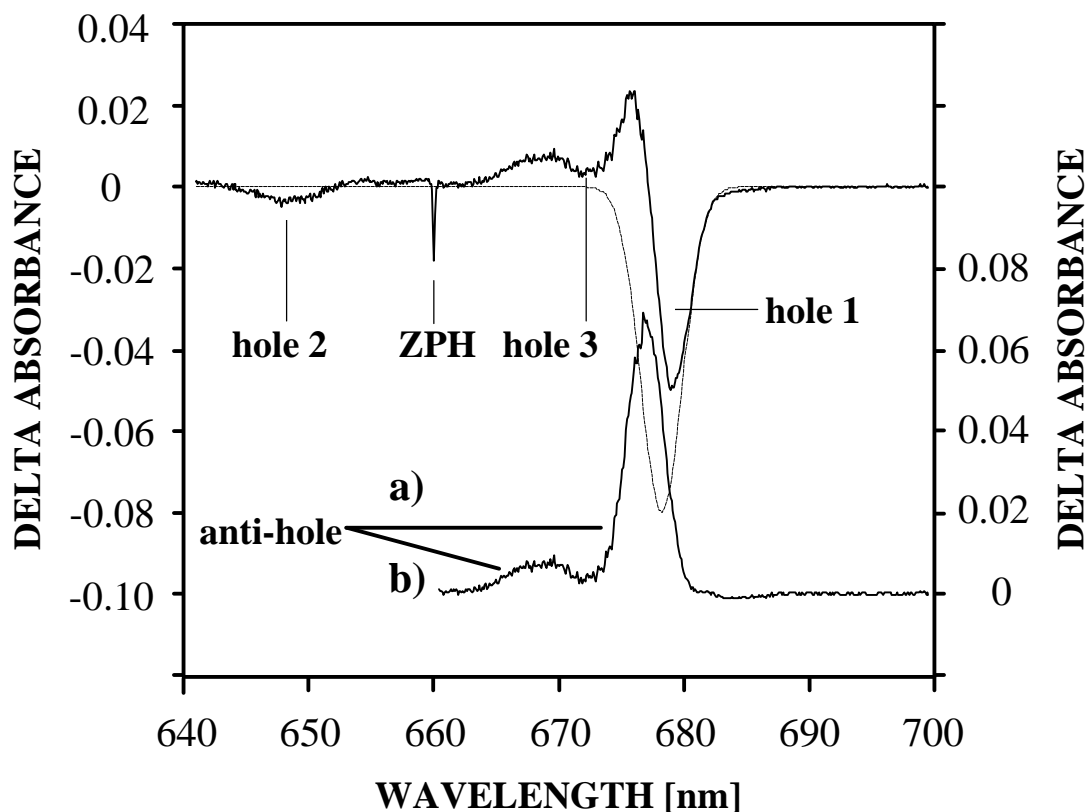


Figure 22. Saturated hole spectrum (top) of trimeric LHC II obtained with  $I_B = 660.0$  nm, a burn intensity of  $130$  mW/cm<sup>2</sup> and a burn time of 30 min. The envelope of the ZPH-action spectrum (dashed curve) is fitted to the low-energy wing of hole 1. The bottom spectrum is the difference between the former two curves and represents the anti-hole spectrum.

The findings presented above suggest that hole 1 „scans“ the spectral shape of the action spectrum with increasing burn fluence. In fact, the remaining difference in shape and peak position of hole 1 and the action spectrum can be understood in terms of interference of hole 1 with its anti-hole. In frame A of Fig. 21 it is apparent that the high-energy wing of hole 1 sharpens as the burn fluence increases. The asymmetry of hole 1 is more obvious in the upper spectrum of Fig. 22 where it is saturated. The profile of the ZPH action spectrum is shown as the dashed curve. The difference between the upper spectrum and the action spectrum fit to the low-energy side of hole 1 is shown at the bottom and represents the anti-hole spectrum. Anti-hole a is symmetric with a width of  $\sim 90$  cm<sup>-1</sup>. It is associated with hole 1, relative to which it is shifted by only  $+25$  cm<sup>-1</sup>. The integrated intensity of anti-hole a accounts for 80% of the intensity of hole 1. The discrepancy of 20% can be understood in terms of interference of the actual anti-hole, which typically is asymmetric with a slight tailing towards higher energy (Shu and Small, 1990), and satellite holes

of higher energy states. The feature labeled as hole 3 appears to be a satellite hole corresponding to the 671 nm absorption band. Anti-hole b is most likely associated with that. The sum of the intensities of anti-holes a and b equals that of hole 1. Thus, it can be concluded that the mechanism of HB is nonphotochemical.

The fractional OD change of the two most intense ZPH of the action spectrum is  $\sim 0.16$ , which is comparable to the changes for the two most intense hole 1 profiles of frame A in Fig. 21. That the former and latter were obtained with burn fluences of  $\sim 4$  and  $200 \text{ J/cm}^2$  might, at first sight, appear to be inconsistent. However, this is not the case since the effective *spectral* burn intensity or fluence must be taken into account. For the case of hole 1, the burn fluence of  $200 \text{ J/cm}^2$  needs to be multiplied by the ratio of the homogeneous width of the ZPL excited at  $\lambda_B = 660 \text{ nm}$  ( $\sim 2 \text{ cm}^{-1}$ ) divided by the inhomogeneous width of the ZPH action profile ( $\sim 90 \text{ cm}^{-1}$ ). This follows since, as previously mentioned, higher energy states and the state(s) associated with the ZPH action spectrum are uncorrelated. Thus, the excitation energy absorbed in a  $\sim 2 \text{ cm}^{-1}$  interval at 660 nm is distributed over the inhomogeneously broadened absorption profile of the low-energy state(s) prior to HB.

From the argumentation given above it appears that the spectral shape and position of hole 1 are in agreement with those of the ZPH action spectrum. Furthermore, the burn conditions applied to obtain both types of hole spectra are consistent. Therefore, it can be concluded that hole 1 and the ZPH action spectrum are due to HB within the same low-energy state(s). The blue-shifting of hole 1 with increasing burn fluence suggests the presence of more than one state in the low-energy region, with the terminal and lowest energy (fluorescent) state being located at 679.8 nm. Because the terminal state has a lifetime of a few ns, it undergoes HB first since the higher energy state(s) near  $\sim 678 \text{ nm}$  should have a shorter lifetime due to EET. The corresponding energy separation of  $\sim 30 \text{ cm}^{-1}$  is large relative to  $kT$  at 4.2 K ( $2.9 \text{ cm}^{-1}$ ). Thus, at 4.2 K one expects that most of the fluorescence should originate from the 679.8 nm state. This is relevant to the discussion of the low-energy level

structure of LHC II, see Chapter 5.

#### 4.1.4 Phonon Sideband Holes

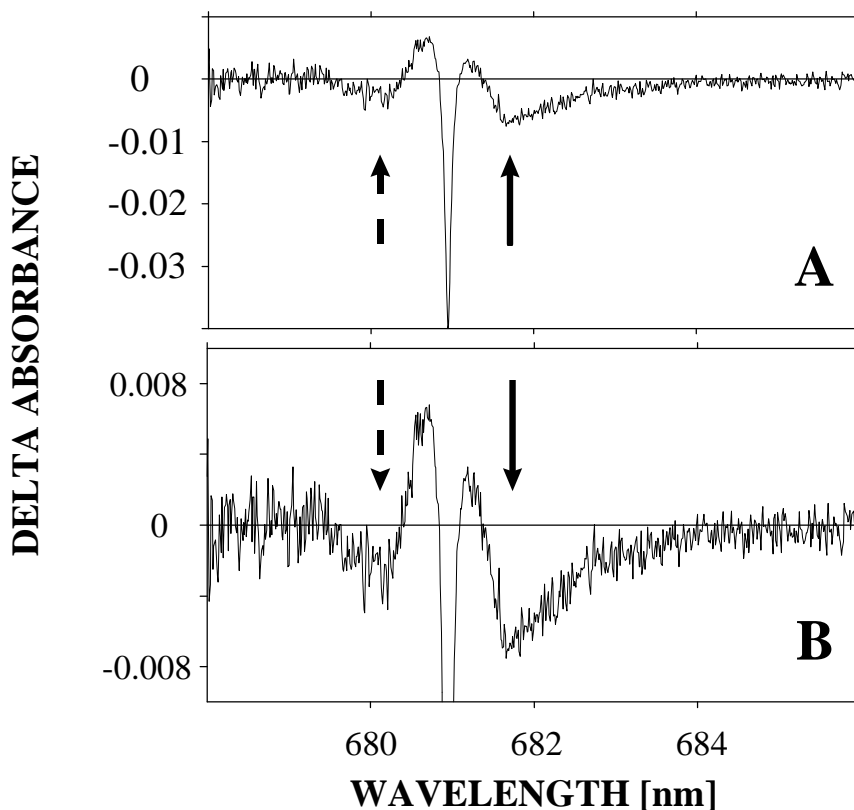


Figure 23. Frame A shows a saturated hole-burned spectrum of LHC II obtained with  $I_B = 681$  nm and a burn fluence of  $15 \text{ J/cm}^2$ . The real- and pseudo-PSBH at  $+24$  and  $-18 \text{ cm}^{-1}$  relative to the ZPH are indicated by dashed and full arrows, respectively. Frame B gives a magnification of the hole-burned spectrum of Frame A for ease of inspection of the PSBH features.

None of the ZPH shown in Figs. 19 and 20 were accompanied by phonon sideband holes for the burn wavelengths and fluences employed. This indicates that the electron-phonon coupling is weak for all  $Q_y$ -states of LHC II. It was already mentioned that the burn efficiency increases drastically for  $\lambda_B \approx 674$  nm (see beginning of Chapter 4.1) and, thus, satellite holes building on the ZPH are produced for high burn fluences (not shown). The burn wavelength, however, has to be tuned further to the red ( $\lambda_B \approx 680$  nm) to prevent superposition of the satellite holes with the broad hole 1 due to EET from higher energy states. Frame A of Fig. 23 shows a saturated hole spectrum (noisy curve) obtained with a burn fluence of  $15 \text{ J/cm}^2$  and  $\lambda_B = 681.0$  nm, i.e. at the low-energy side of the ZPH action spectrum. The

fractional absorbance change of the ZPH is 0.40. A magnification of the PSBH features accompanying the ZPH is given in Frame B of Fig. 23. The real- and pseudo-PSBH at +24 and -18  $\text{cm}^{-1}$  relative to the ZPH are indicated by broken and full arrows, respectively. The pseudo-PSBH is asymmetric with a width of  $\sim 25 \text{ cm}^{-1}$ . Unfortunately, the real-PSBH is interfered with by the anti-hole which is characteristic of NPHB. Therefore, further analysis will be based on the pseudo-PSBH. According to Hayes et al. (1988b), the saturated fractional OD change of the ZPH at the low-energy side of an inhomogeneously broadened absorption band is approximately given by  $\exp(-S)$  where  $S$  is the Huang-Rhys factor (see Eq. 21). Thus, for a fractional OD change of 0.40 a value of  $\sim 0.9$  can be estimated for  $S$  assuming that the absorption due to the next higher state at  $\sim 676 \text{ nm}$  band is negligible at 681 nm.

A detailed theoretical analysis of the phonon structure observed in HB and corresponding line-narrowed fluorescence spectra of LHC II will be given in Chapter 7. As a preliminary result, however, it can be concluded that the lowest state(s) of trimeric LHC II is characterized by weak electron-phonon coupling ( $S = 0.9$ ) to phonons with a mean frequency of  $\sim 18 \text{ cm}^{-1}$ . Similar (weak) coupling strengths and phonon frequencies have been reported for other antenna complexes (for a review see Reddy et al., 1992).

#### **4.2 Effects upon Aggregation of LHC II**

It is well-established that utilization of glycerol as glass-forming solvent may induce non-desirable aggregation effects in LHC II (Vasil'ev et al., 1997b). Thus, it appeared to be necessary to test the systematic deviations emerging in hole-burned spectra upon aggregation of LHC II. Consequently, experiments comparable to those reported for trimeric LHC II in Chapter 4.1 were also performed for aggregated LHC II.

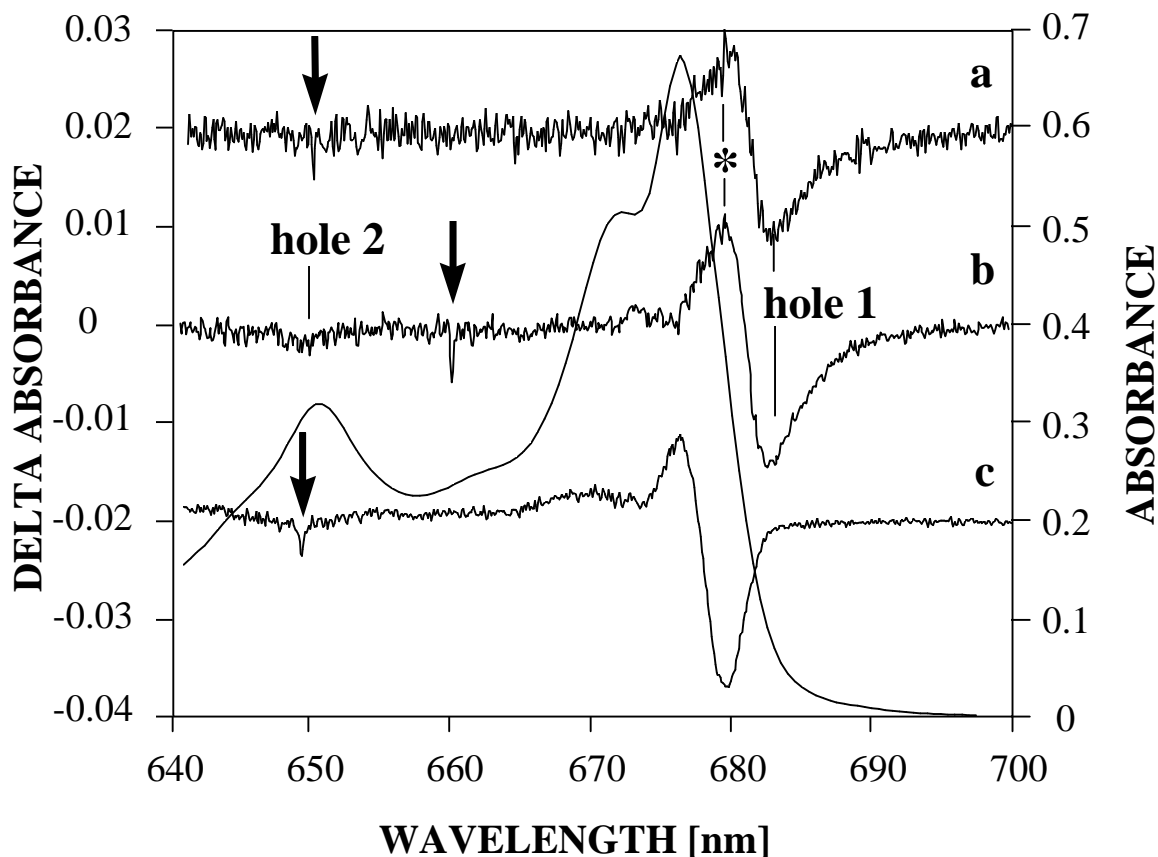


Figure 24. Typical hole-burned spectra of aggregated (a, b) and trimeric LHC II (c) obtained with a burn laser intensity of  $100 \text{ mW/cm}^2$  and a read resolution of  $4.0 \text{ cm}^{-1}$ . The burn wavelengths (indicated by arrows) and burn times were a) 649 nm and 10 min, b) 660 nm and 30 min, c) 648.5 nm and 10 min, respectively. Hole-burned spectra are separated by DOD of 0.02. The 4.2 K absorption spectrum of aggregated LHC II (full, smooth line) is given for comparison.

The 4.2 K absorption spectrum of aggregated LHC II shown in Fig. 24 exhibits four main bands at 676.3, 671.9, 662.0 and 650.5 nm which are red-shifted by 1 nm relative to those of trimeric LHC II, see Chapter 4.1. Besides this slight uniform shifting, the  $Q_y$ -spectra of aggregated and trimeric LHC II are essentially identical. HB of aggregated LHC II was performed with burn wavelengths ( $\lambda_B$ ) between 640 and 688 nm for different burn fluences at 4.2 K. Traces a and b of Fig. 24 show hole-burned spectra of aggregated LHC II which are quite typical for  $\lambda_B < 676 \text{ nm}$ . The most obvious features of these spectra are a) a ZPH coincident with the burn wavelength, b) a broad hole (hole 1) in the vicinity of 682.5 nm having a width of about  $80 \text{ cm}^{-1}$  and c) a broad and shallow hole (hole 2) at about 650 nm. The feature labeled by the asterisk in Fig. 24 is the anti-hole of hole 1. For all burn wavelengths employed the most intense feature of the hole-burned spectrum is hole 1 located in the

low-energy wing of the 676.3 nm absorption band.

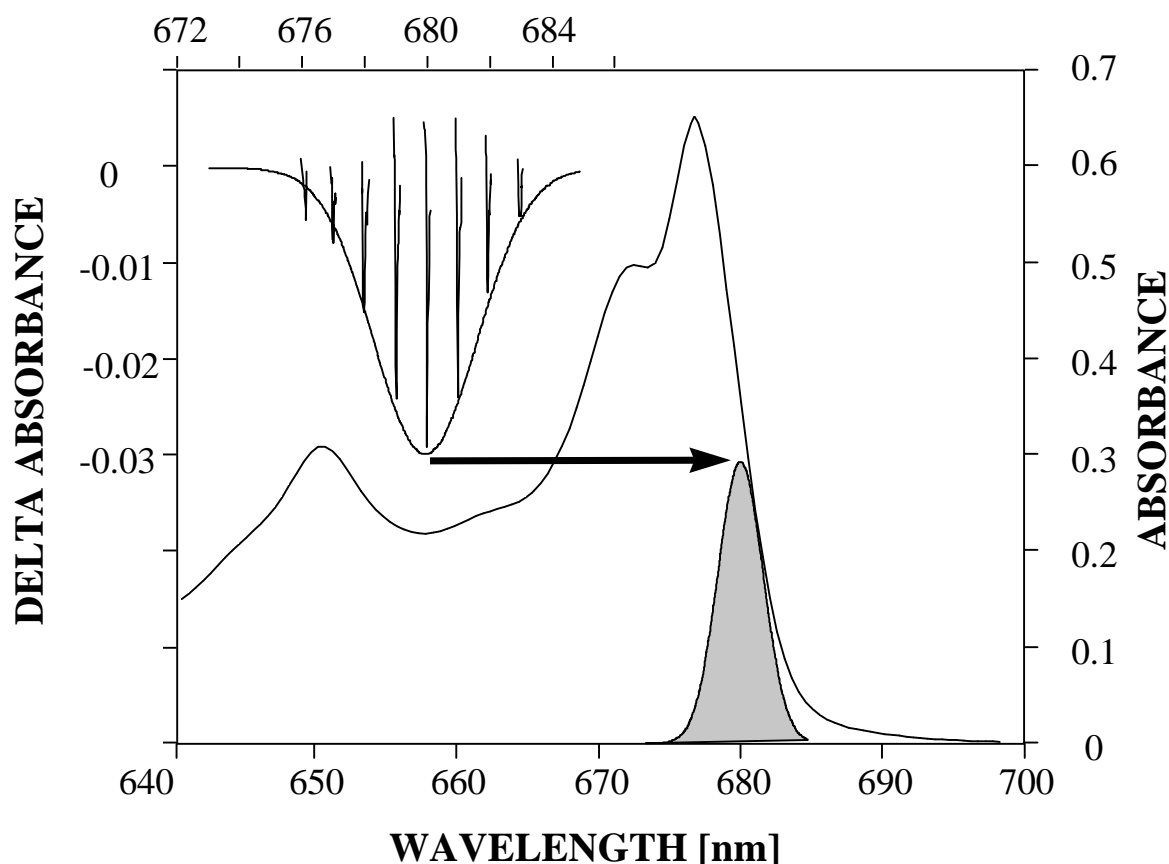


Figure 25. The 4.2 K absorption and ZPH-action spectrum (see upper, left corner) of aggregated LHC II. The action spectrum was generated with a constant burn fluence of  $6 \text{ J/cm}^2$  and a read resolution of  $0.3 \text{ cm}^{-1}$ . Its location within the 4.2 K absorption spectrum is indicated by the hatched profile.

For comparison, a hole-burned spectrum of trimeric LHC II is shown as spectrum c in Fig. 24. For comparable burn fluences, hole 1 of trimeric LHC II is located at 679.4 nm, i.e. 3 nm to the blue of hole 1 of the aggregated complex. This shift is about 3 times larger than the shift of the principal absorption bands. The width of hole 1 increases from  $55 \text{ cm}^{-1}$  to about  $80 \text{ cm}^{-1}$  upon aggregation. The observed broadening of hole 1 is most likely connected with the slight tailing of its low-energy wing. Therefore, it has to be concluded that aggregated LHC II is characterized by additional weak absorption at  $\lambda \approx 683 \text{ nm}$ . This tailing can most likely be ascribed to aggregation-induced, red-emitting states lying at wavelengths  $\approx 683 \text{ nm}$  that were assigned in steady-state fluorescence and fluorescence decay experiments (Vasil'ev et al., 1997a).

The broad Chl *b* hole (hole 2) for the aggregate lies at  $(650.2 \pm 0.3)$  nm. This represents a red-shift of about 2 nm compared to its position at  $(648.3 \pm 0.3)$  nm in trimeric LHC II while its width of  $\sim 125 \text{ cm}^{-1}$  remains almost the same.

As for trimeric LHC II, constant fluence hole-burning (ZPH-action) spectroscopy was employed in order to further investigate the spectral position and inhomogeneous width of the lowest state(s). The ZPH-action spectrum obtained for a burn fluence of  $6 \text{ J/cm}^2$  and a read resolution of  $0.3 \text{ cm}^{-1}$  is shown in Fig. 25. It is centered at 680 nm and can be fit by a Gaussian envelope with a width of  $(90 \pm 10) \text{ cm}^{-1}$ . The widths of the ZPH (uncorrected for read-resolution) decrease from  $2.0 \text{ cm}^{-1}$  (677 nm) to  $0.6 \text{ cm}^{-1}$  (681-683 nm) at the low-energy wing of the action spectrum. The broader ZPH observed at the high-energy wing of the action spectrum most probably stem from downward EET from states associated with the main 676.3 nm absorption band.

A comparison of the above results for aggregated and trimeric LHC II shows that, upon aggregation, the lowest energy state(s) of the isolated trimer are basically red-shifted by about 2 nm. At the same time, the width of the inhomogeneous distribution function and the homogeneous widths of the ZPH associated with the action spectrum are remain virtually unaffected. This also applies to the observed narrowing of the ZPH when the burn wavelength is tuned from the blue to the red sides of the action spectrum. Therefore, it can be concluded that the low-energy level structure of trimeric LHC II remains almost intact upon aggregation except for the slight red-shifting. A more detailed inspection of the low-energy level structure near 680 nm as well as implications of the reported HB results for the function of aggregated LHC II in the dissipation of excess energy is given in Pieper et al. (1999b).

In view of the discussed similarities, it seems to be possible to identify hole-burned spectra of aggregated LHC II by fault as „shifted“ spectra of trimeric LHC II. The red-shifts of low-energy hole features, i.e. hole 1 and the ZPH action spectrum, as well as additional absorption for  $\lambda > 683$  nm observed upon aggregation introduce considerable uncertainty in the assignment of low-energy states of LHC II. As a consequence, strong attention has to be paid to

prevent non-desirable aggregation effects due to glycerol-containing buffer solutions. Nevertheless, an inspection of Fig. 22 in Chapter 4.1.3 reveals that the low-energy wing of the ZPH action spectrum of trimeric LHC II is in perfect agreement with that of the corresponding hole 1. Thus, the trimeric LHC II studied in the present work is virtually free from aggregation effects and exhibits no additional absorption at wavelengths higher than  $\sim 680$  nm. This conclusion is in agreement with those of Vasil'ev et al. (1997b), see Chapter 3.1.1.

### **4.3 Hole-Burned Spectra of CP29**

Because of the structural similarities and the smaller number of bound chromophores, spectroscopic studies of CP29 may also be useful in interpretation of data obtained for the trimeric LHC II complex. Especially, CP29 occurs in monomeric form. Thus, 4.2 K HB experiments similar to those reported for the trimeric LHC II in Chapter 4.1 were performed for the isolated and purified CP29 Chl *a/b* binding complex in order to identify and characterize its lowest energy state.

#### **4.3.1 Hole-Burning with Burn Wavelengths Lower than 674.5 nm**

The 4.2 K  $Q_y$ -absorption spectrum of CP29 is shown in Fig. 26 (see dashed line). With a prominent band at 674.5 nm, a weak shoulder at about 665 nm and two further bands at 638.5 and 650.0 nm it is quite similar to previously reported spectra (Zucchelli et al., 1994; Pascal et al., 1999). HB of CP29 was first performed with burn wavelengths ( $\lambda_B$ ) lower than that of the most intense band at 674.5 nm and with burn fluences ranging from 3 to about 500 J/cm<sup>2</sup>. As observed for LHC II, the burned holes were persistent on the time scale of the experiment, but completely reversible upon temperature increase to about 150 K. This indicates that the resulting absorption difference spectra are due to persistent NPHB. Fig. 26 shows only saturated hole spectra which are quite typical for  $\lambda_B$ -values in this spectral region. They were obtained with a burn fluence of about 500 J/cm<sup>2</sup> and  $\lambda_B$ -values of 638.5 (spectrum a) and 650.0 nm (spectrum b) within the two Chl *b* bands, as well as for a  $\lambda_B$ -value of 665.0 nm (spectrum c). The arrows in Fig. 26 indicate the burn wavelengths.

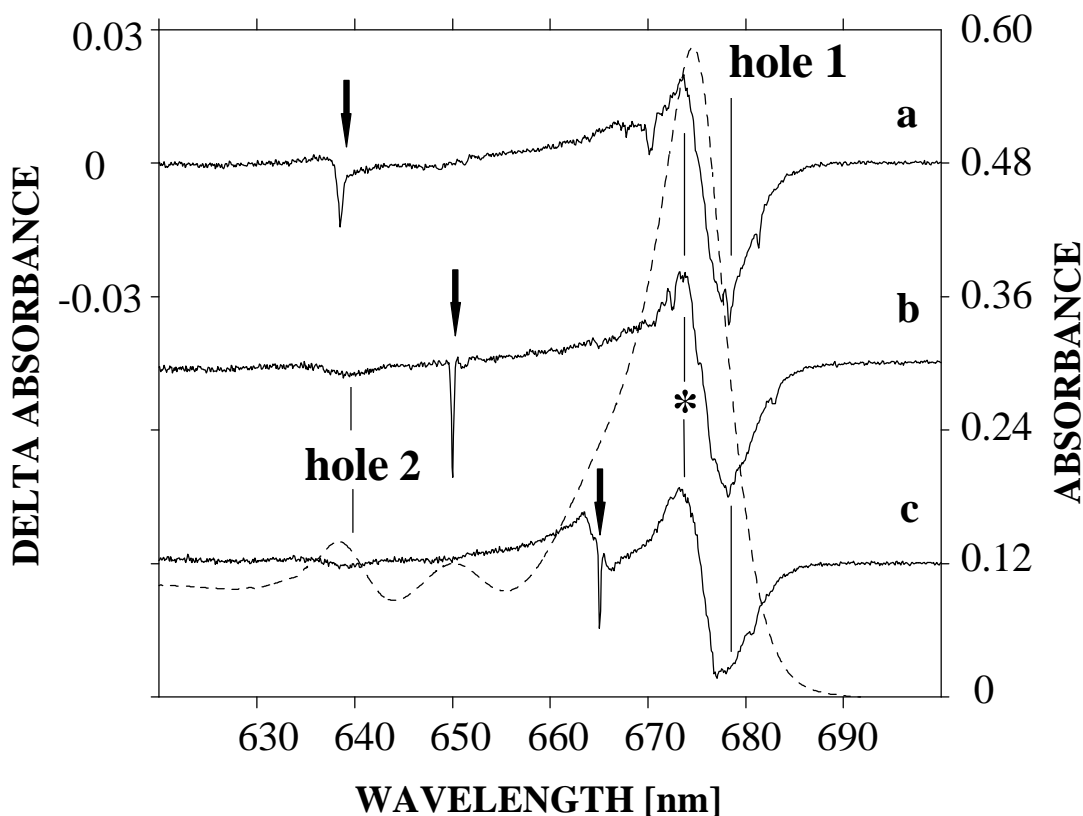


Figure 26. Absorption (dashed line) and typical hole-burned spectra (full lines) of CP29 at 4.2 K. Hole spectra were obtained with a burn fluence of about  $500 \text{ J/cm}^2$  and a read resolution of  $4.0 \text{ cm}^{-1}$ . The burn wavelengths (marked by arrows) were a) 638.5 nm, b) 650.0 nm and c) 665.0 nm, respectively. The position of the anti-hole of hole 1 is indicated by an asterisk. Hole spectra are separated by a DA of 0.045.

A magnification of the low-energy region of spectra a, b and c is shown in Fig. 27. All spectra in Fig. 26 exhibit four main features: a ZPH coincident with the burn wavelength, a broad and intense hole (hole 1) at 678.2 nm, a blue-shifted anti-hole (located by the asterisk) associated with hole 1 and a broad and shallow hole (hole 2) at about 639 nm. In addition, all hole spectra show a number of relatively sharp low-energy satellite ZPH in the vicinity of hole 1. These satellite holes are displaced from  $\lambda_B$  by wavenumber values (see labels and thin arrows in Fig. 27) corresponding to the energies of Chl a excited state vibrations. The 264, 517, 573, 606, and 744 wavenumber values agree within an experimental uncertainty of  $\pm 2$  with those reported for Chl a in Photosystem I particles (Gillie et al., 1989). The 342, 918 and 984 wavenumber values differ by  $\sim 10 \text{ cm}^{-1}$  from those reported by Gillie et al.. The latter excited state vibrational frequencies, however, are quite consistent with the ground state vibrational frequencies observed in FLN experiments for

trimeric LHC II (Peterman et al., 1997). The differences between the two sets of vibrational energies may result from the way the Chl a molecules of CP29 are embedded into the protein matrix, i.e. some of the Chl a excited state vibrational frequencies may be altered or hindered by the environment. Nevertheless, it can be concluded that the satellite ZPH are the result of HB of vibronic bands that build on the Chl a origin band region (Reddy et al., 1992).

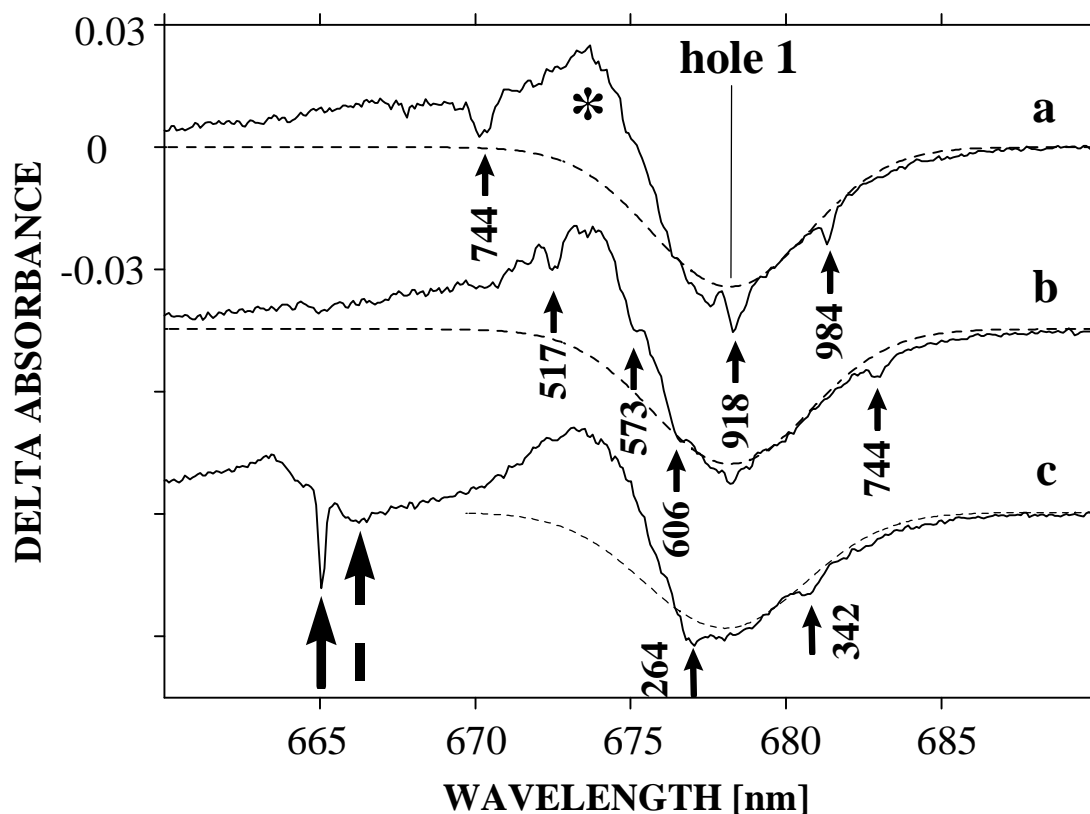


Figure 27. Low-energy part of hole-burned spectra a, b and c (full lines) of Fig. 26. Peak position and low-energy wing of hole 1 are fit by Gaussian profiles (dashed lines) centered at  $14745 \text{ cm}^{-1}$  ( $678.2 \text{ nm}$ ) and having a width of  $130 \text{ cm}^{-1}$ . The position of the anti-hole is indicated by an asterisk. The ZPH at  $665.0 \text{ nm}$  (marked by a thick, full arrow) is accompanied by a pseudo-phonon sideband (marked by a thick, broken arrow) with a peak frequency of  $\sim 20 \text{ cm}^{-1}$ . Thin arrows and frequencies label the positions of vibrational ZPH.

The most intense feature of all hole spectra shown in Fig. 26 is hole 1 located at  $(14745 \pm 5) \text{ cm}^{-1}$  ( $678.2 \text{ nm}$ ), which is almost  $4 \text{ nm}$  lower in energy than the  $674.5 \text{ nm}$  absorption band. A Gaussian fit (dashed lines in Fig. 27) based on its peak position and low-energy side yielded a width of  $(130 \pm 10) \text{ cm}^{-1}$ . Interference of hole 1 with its anti-hole (see asterisk) is responsible for the steeper, non-Gaussian rise of its high-energy wing. In spectrum c hole 1 is superimposed with the satellite ZPH corresponding to the  $264 \text{ cm}^{-1}$  Chl a

excited state vibration. This leads to a slight deviation from the Gaussian fit. Apart from this, the position and the width of hole 1 was independent of burn fluence (results not shown) and burn wavelength (see Fig. 27). The above results strongly indicate that the absorption band of the lowest energy state of CP29 is located at about 678.2 nm and that it is populated from higher states by efficient EET. The observation of sharp ZPH in the vicinity of hole 1 upon vibronic HB establishes that the 678.2 nm band is characterized by significant inhomogeneous broadening, *vide infra*.

Spectra b and c of Fig. 26 reveal that burning at 650.0 and 665.0 nm produces a broad (width of  $\sim 110 \text{ cm}^{-1}$ ) and shallow high-energy satellite hole at  $(639.4 \pm 0.5) \text{ nm}$  that is essentially coincident with the higher energy Chl *b* absorption band. This satellite hole was not observed for  $\lambda_B = 676.0, 680.0$  and  $682.0 \text{ nm}$ , wavelengths in the vicinity of the lowest energy  $Q_y$ -state (results not shown), which indicates that the coupling of the Chl *a* molecule associated with this state and the Chl *b* molecules is weak.

#### 4.3.2 Constant Fluence Hole-Burning in the Low-Energy Region

Constant fluence hole-burning (ZPH-action) spectroscopy was employed in the vicinity of hole 1 in order to further investigate the spectral position and inhomogeneous width of the lowest state's absorption band. The action spectrum is shown in the upper left hand corner of Fig. 28. Under the conditions of the experiment (see figure caption), the fractional depths of the ZPH were less than 0.12 so that the action spectrum should not be significantly affected by saturation effects. Furthermore, higher energy states do not contribute significantly to the ZPH because of their much shorter lifetimes due to downward EET, see Chapter 2.2.2. The action spectrum can be fit by a Gaussian with a peak position at  $(14740 \pm 10) \text{ cm}^{-1}$  (678.4 nm) and a width of  $(120 \pm 10) \text{ cm}^{-1}$ . These values are in close agreement with the position and width of hole 1 shown in Fig. 26, *vide supra*. Furthermore, the action spectrum establishes that hole 1 is mainly inhomogeneously broadened.

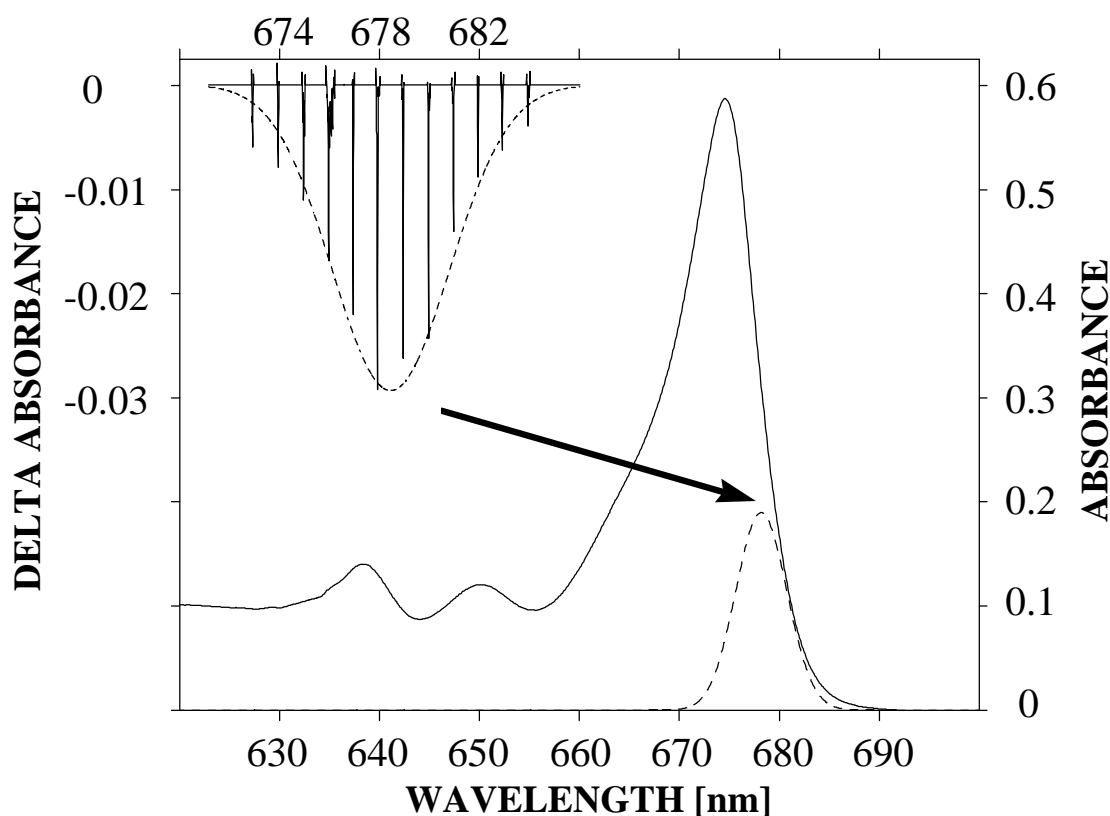


Figure 28. The 4.2 K absorption and ZPH-action spectrum (see upper, left corner) of CP29. The action spectrum was generated with a constant burn fluence of  $0.05 \text{ J/cm}^2$  and read resolution of  $0.5 \text{ cm}^{-1}$ . Its position within the absorption spectrum is indicated by the dashed line.

The widths of the ZPH in the action spectrum shown in Fig. 28 are limited by the read resolution of  $0.5 \text{ cm}^{-1}$ . Therefore, high-resolution ( $< 30 \text{ MHz}$ ) experiments were performed at 4.2 K in the fluorescence excitation mode in order to determine the true widths for three representative burn wavelengths (676.1, 678.1 and 680.4 nm) within the inhomogeneously broadened absorption band of the lowest state. The last two burn wavelengths are located near the maximum of the band and on its low-energy side, respectively, and yield almost identical holewidths of  $\sim 0.05 \text{ cm}^{-1}$  based on Lorentzian fits. This width corresponds to an effective dephasing time of 400 ps. The width of the hole at 676.1 nm is about a factor of 2 broader. This increase may be due to a contribution to the hole from the next higher state at  $\sim 674.5 \text{ nm}$  and/or some saturation broadening. The important result is, however, that the spectral dynamics is independent of  $\lambda_B$  for  $\lambda_B \gtrsim 678 \text{ nm}$ . The temperature dependence (1.8-10 K) of the holewidth for  $\lambda_B$  in the near vicinity of 680 nm carries a  $T^{1.3}$  dependence for  $T \gtrsim 8 \text{ K}$  (not shown). This dependence is the signature for

spectral dynamics stemming from coupling to the glass-like TLS of the protein (see, e.g., Hayes et al., 1988a; Völker, 1989).

On the basis of the results discussed above, it can be concluded that the absorption band of the lowest energy and fluorescent state of CP29 is located at 678.2 nm at 4.2 K, about 4 nm lower than the wavelength of the most intense absorption band at 674.5 nm. In general, this observation is comparable to the results obtained for the structurally similar trimeric LHC II (see Chapter 4.1). Most striking, however, is the absence of a blue-shift for hole 1 of CP29 with increasing burn fluence, which was observed for the analogous feature in hole-burned spectra of LHC II and indicated the presence of more than one low-energy state (see Chapter 4.1). The consequences of these findings for the assignment of the low-energy  $Q_y$ -states of trimeric LHC II will be discussed in Chapter 5. A more detailed discussion of assignment and nature of the lowest  $Q_y$ -state as well as EET dynamics of CP29 is given in Pieper et al. (2000).

#### ***4.4 Pressure-Dependent Spectra of LHC II***

As already mentioned in Chapter 2.5, an investigation of the pressure dependence of absorption and hole-burned spectra of LHC II may permit conclusions on Chl-Chl coupling strengths. Thus, the pressure dependence of the 77 K  $Q_y$ -absorption spectrum of LHC II was studied up to 463 MPa. The spectra obtained for several pressures are shown in Fig. 29. There is an apparent red-shifting of the major bands at 650, 671 and 676 nm with increasing pressure. A larger shift rate for the 671 nm band relative to the 676 nm band leads to an interesting narrowing of the overall absorption profile in the vicinity of the 671 and 676 nm bands. It should also be noted that the absorption at ~ 661 nm decreases with increasing pressure until the valley between the 650 and 671 nm bands is flat.

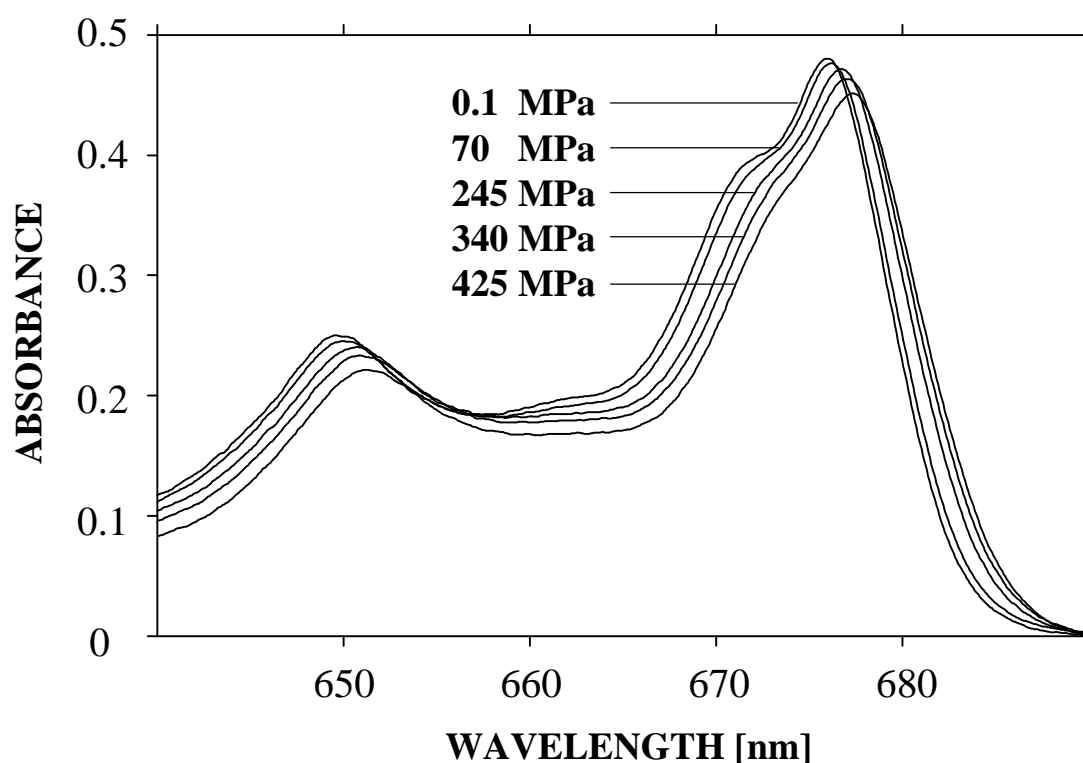


Figure 29. Pressure dependence of the 77 K absorption spectrum of trimeric LHC II. Upon pressure release, the ambient pressure spectrum (0.1 MPa) was recovered indicating elastic behavior (not shown).

Fig. 30 confirms that the shift rates visible in Fig. 29 depend linearly on pressure as previously observed for photosynthetic complexes as well as for isolated chromophores in polymers and glasses (see e.g. Reddy et al., 1996). The linear pressure shift rates for the 650, 671 and 676 bands are  $-0.088$ ,  $-0.094$  and  $-0.069$   $\text{cm}^{-1}/\text{MPa}$ , respectively. Since these bands are contributed to by several states, the pressure shifts should be viewed as averages. Higher selectivity is achieved using HB. The upper and lower data points in Fig. 31 are for ZPH burned at 12 K with  $\lambda_B = 677$  and 678 nm, respectively. These wavelengths are close to the maximum of the ZPH action spectrum of Fig. 20. The linear shift rates of  $-0.077$  and  $-0.088$   $\text{cm}^{-1}/\text{MPa}$  at 4.2 K are similar to those given above. For a better comparison with the 77 K rates, the 12 K rates should be increased by  $\sim 10$ -15% to account for a weak dependence of the protein compressibility on temperature (see e.g. Reddy et al., 1996).

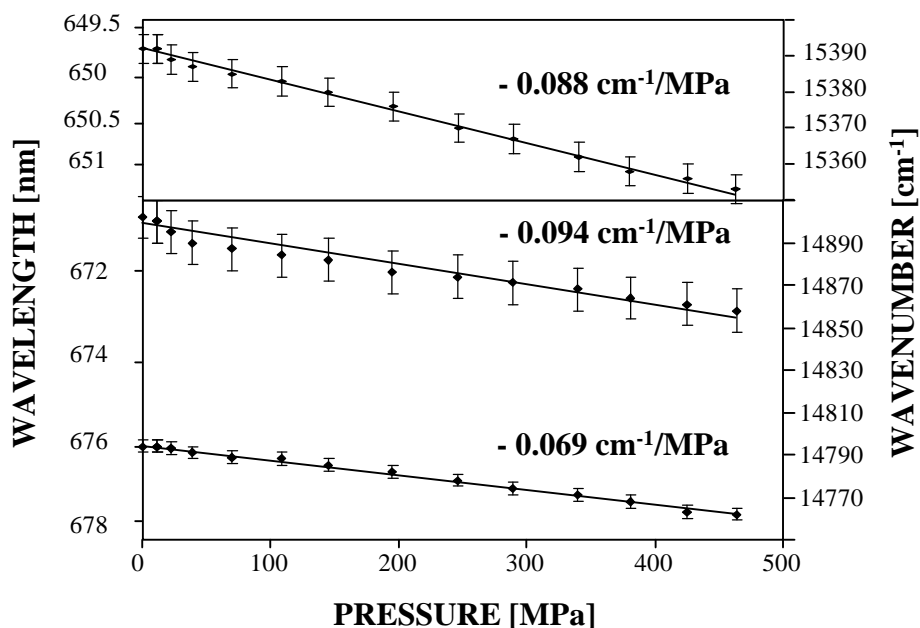


Figure 30. Linear pressure shifting of the 649.5 nm (top), 671.3 nm (middle) and 676.1 nm (bottom) absorption bands of trimeric LHC II at 77 K (labeled by shift rates).

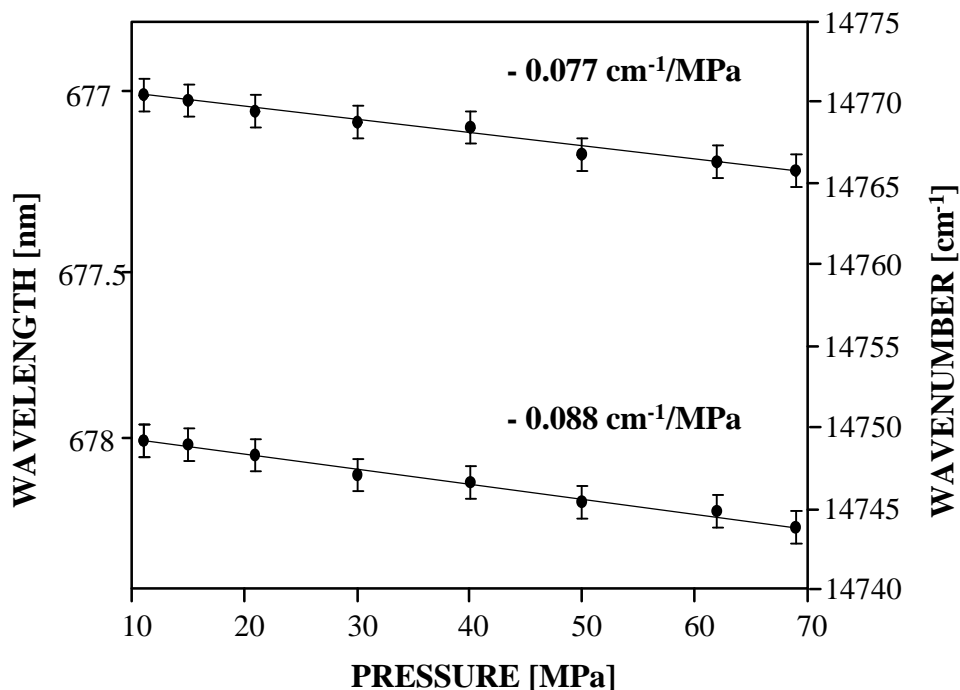


Figure 31. Linear pressure shifting of zero-phonon holes burned at 677.0 nm (top) and 678.0 nm (bottom) at 12 K (labeled by shift rates).

Nevertheless, the shift rates observed are comparable to those reported for isolated chromophores in polymers and glasses. Therefore, it appears that excitonic interactions in LHC II are too weak to affect the pressure dependence

and the shift rates are dictated by Chl-protein interactions, see Chapter 5.2.

#### 4.5 Fluorescence Spectra of LHC II

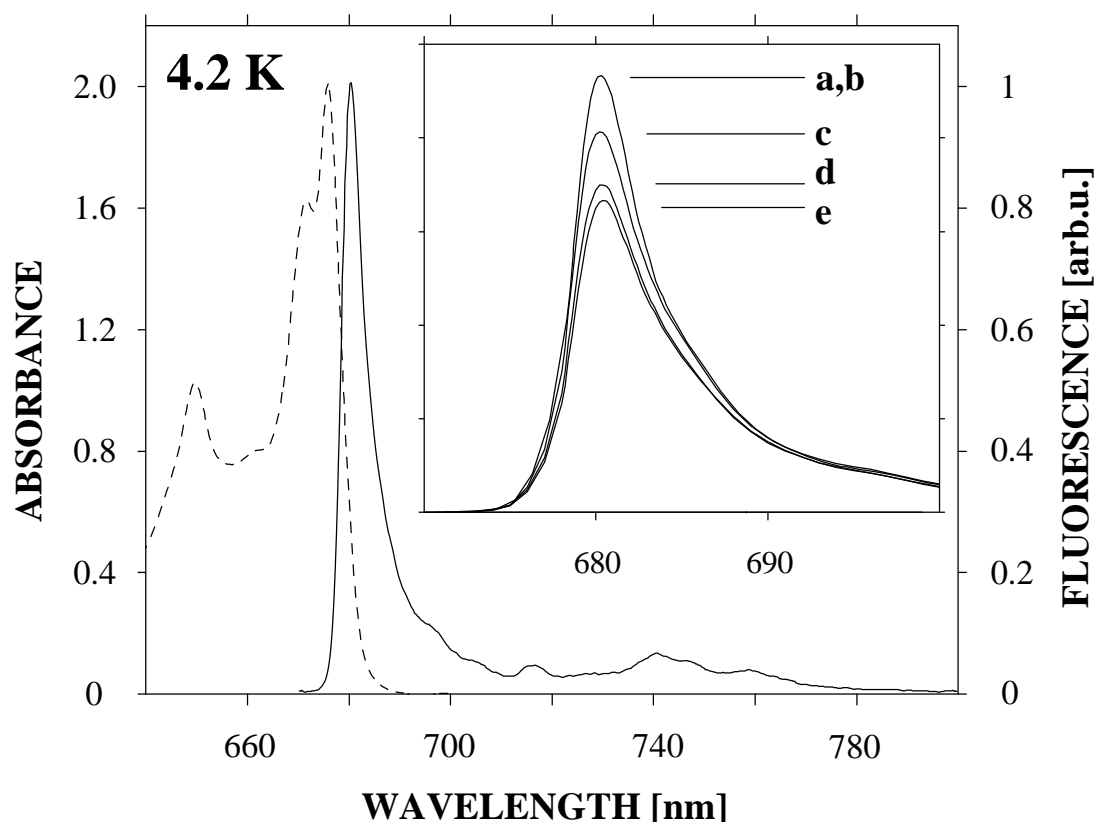


Figure 32. The 4.2 K absorption (dashed line) and normalized fluorescence spectrum (full line) of trimeric LHC II. The latter spectrum is the same as spectrum a in the inset. The inset shows 4.2 K fluorescence spectra obtained for samples of different optical density (different optical pathlength of cuvettes), i.e. a) 0.02 (0.01 mm), b) 0.2 (0.1 mm), c) 0.4 (0.2 mm), d) 1.0 (0.5 mm), and e) 2.0 (1.0 mm) at 676 nm and a constant chlorophyll concentration of 0.2 mg/ml. The spectra are normalized at 740 nm.

The availability of reliable fluorescence data is important for the verification of both, the assignment of the low-energy states as well as the parameters of electron-phonon coupling obtained on the basis of spectral HB experiments. Thus, the non-line-narrowed fluorescence spectra of LHC II were measured at 4.2 K and for several other temperatures up to 300 K.

##### 4.5.1 The 4.2 K Fluorescence Spectrum

The 4.2 K absorption and fluorescence spectra of LHC II are shown in Fig. 32. The non-line-narrowed fluorescence spectrum (see full line) was excited at 430 nm and obtained for a sample with an optical density (OD) of 0.02 at 676 nm, *vide infra*. It is characterized by a broad and strongly asymmetric

origin band peaking at  $(680.3 \pm 0.2)$  nm with a width of  $(5.5 \pm 0.2)$  nm. The main fluorescence band is accompanied by a number of partially resolved satellite features (e.g. at  $\sim 697$ ,  $\sim 715$ ,  $\sim 741$ , and  $769$  nm) which were shown to correspond to intramolecular vibrations of Chl *a* (Kwa et al., 1993; Peterman et al., 1997). The peak positions and the absence of a shoulder at  $\sim 695$  nm in the fluorescence spectrum establish that this preparation is virtually free of aggregation effects (Vasil'ev et al., 1997b).

#### ***4.5.2 Effects Owing to Reabsorption***

The main fluorescence band at 680.3 nm shows an apparent overlap with the sharply decreasing low-energy wing of the absorption spectrum. Moreover, the HB results of Chapter 4.1.3 indicate that the lowest (fluorescing)  $Q_y$ -state of LHC II is located at  $\sim 679.8$  nm, i.e. almost resonant to the fluorescence maximum. Under such circumstances strong reabsorption can be expected. In order to investigate this effect, fluorescence measurements were carried out varying the OD of the LHC II samples at a constant chlorophyll concentration (see inset of Fig. 32). For the sake of direct comparability, the data were normalized at 740 nm where no influence of reabsorption is expected. An inspection of the results reveals two striking features: a) a marked increase of emission in the peak region and b) a small but discernible blue-shift as well as an obvious narrowing of the main fluorescence band with decreasing OD. Similar observations were made varying the chlorophyll concentration at constant optical pathlength (not shown). As a consequence strong attention has to be paid to eliminate effects owing to reabsorption. However, no further changes arise, within experimental uncertainty, between the spectra for the lowest two OD values. Therefore, the 4.2 K fluorescence spectrum obtained for samples with the lowest OD of 0.02, *vide supra*, seems to be virtually unaffected by reabsorption in the case of LHC II and suitable to be compared with model calculations and line-narrowed spectra measured at that temperature (see Chapter 7.1).

### 4.5.3 Temperature-Dependent Fluorescence Spectra

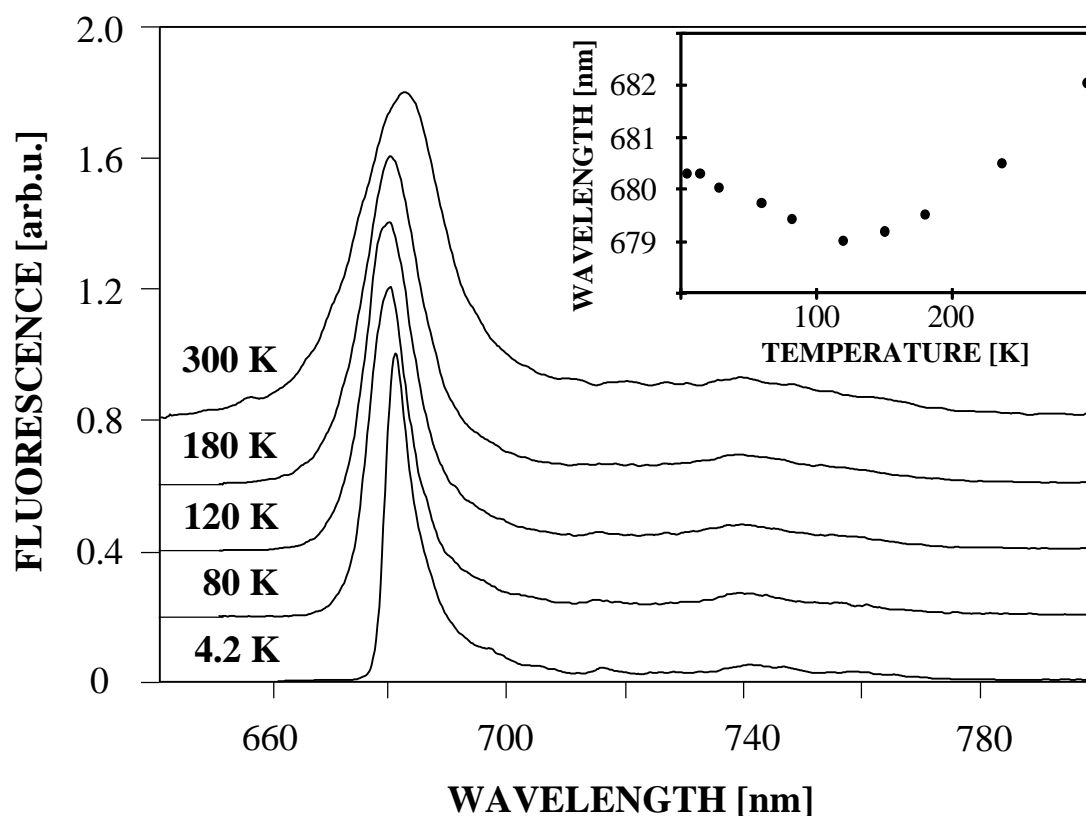


Figure 33. Normalized fluorescence spectra of LHC II excited at 430 nm for different temperatures between 4.2 K and 300 K (see labels). The spectra are separated by an equidistant offset of 0.2. The inset shows the position of the fluorescence maximum as a function of temperature.

Fluorescence spectra of LHC II measured under the same conditions for various temperatures between 4.2 and 300 K are shown in Fig. 33. Most striking is the temperature dependence of the fluorescence maximum (see inset of Fig. 33), which shifts to the blue from 680.3 nm at 4.2 K to 678.9 nm at 120 K. If the temperature is further increased, however, the fluorescence maximum shifts continuously back to the red peaking at 682.0 nm at room temperature. A similar temperature dependence has already been observed (Peterman et al., 1997). At the same time the origin band broadens from 5.5 nm at 4.2 K to 8.4 nm at 80 K and 17.5 nm at room temperature while its shape becomes more symmetric.

### 4.6 Line-Narrowed Fluorescence Spectra of LHC II

As discussed in detail in Chapter 2, FLN experiments may provide valuable information on electron-phonon coupling parameters, especially on the one-

phonon profile, of pigment-protein complexes. In this regard, results gathered from line-narrowed fluorescence spectra should be directly comparable to those of corresponding HB experiments at 4.2 K (see Chapter 4.1.4). Line-narrowing in LHC II fluorescence spectra was achieved by selective laser excitation within the fluorescence origin band at a temperature of 4.2 K. As discussed in the next chapters, special attention was paid to eliminate possible systematic errors.

#### ***4.6.1 Artifacts Owing to Light Scattering***

The ZPL of the FLN spectra ( $\lambda_E = 680.5$  nm) shown as full lines in Fig. 34 are obscured by scattered laser light. This effect is typical for FLN spectra because the ZPL is coincident with the excitation wavelength. In order to permit a subtraction of the scattered laser light from the FLN spectra, the spectral characteristics of the excitation beam was directly measured by placing a reflecting, non-emitting surface at the position of the sample. The resulting spectrum is shown as a dashed line in Fig. 34, where it is normalized to the high-energy wing of the FLN spectrum. Subtraction of the dashed spectrum from the FLN spectrum readily yields the PSB.

#### ***4.6.2 Effects Owing to Hole-Burning***

For an excitation intensity of approximately  $10^{13}$  photons per  $\text{cm}^2$  and pulse at excitation wavelengths  $> 680.0$  nm no decrease of the fluorescence signal was observed during the time course of the measurement. This indicates that HB effects are negligible. Consequently, the wavelength dependence of the FLN spectra (see Chapter 4.6.4) was studied using these experimental conditions. A typical FLN spectrum excited at 680.5 nm with a laser intensity of  $10^{13}$  photons per  $\text{cm}^2$  and pulse is shown in Fig. 34 and labeled by „FLN“.

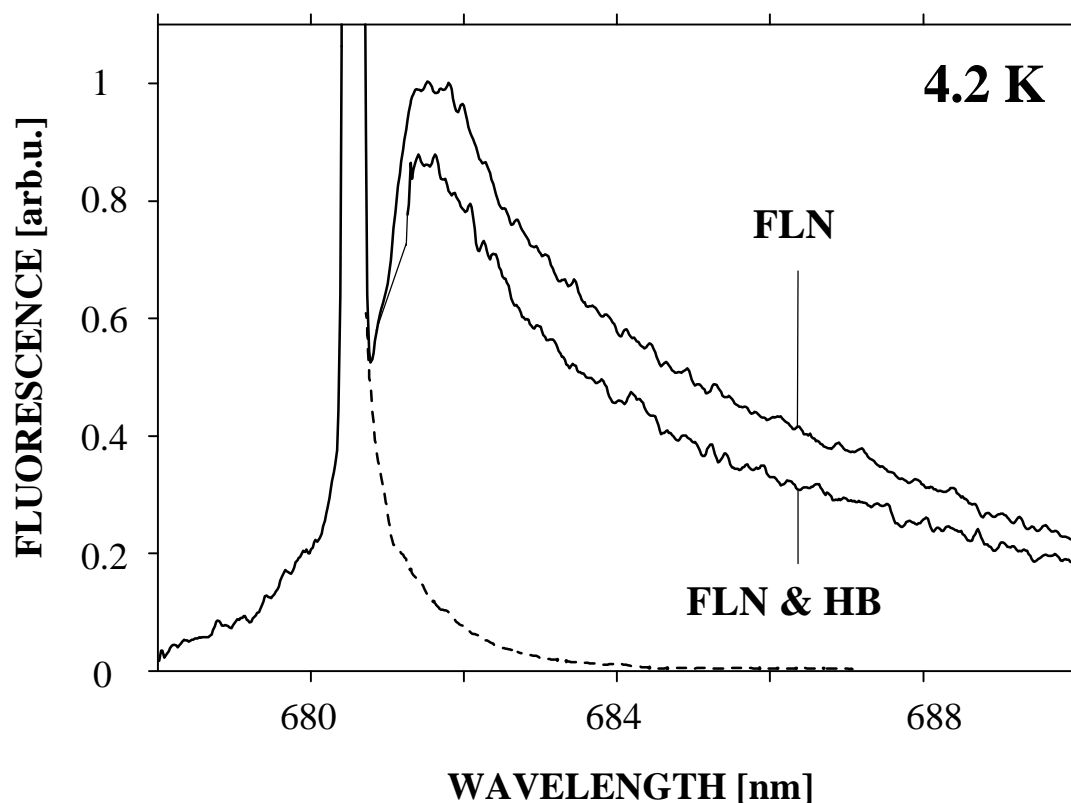


Figure 34. Selectively excited fluorescence spectra at 4.2 K (full lines). The upper FLN spectrum (labeled by „FLN“) was excited at 680.5 nm with a laser intensity of  $\sim 10^{13}$  photons per  $\text{cm}^2$  and pulse. The lower spectrum (labeled by „FLN & HB“) was obtained under identical conditions but after previous exposure of the sample to a laser intensity of  $\sim 10^{14}$  photons per  $\text{cm}^2$  and pulse for 300 s. The dashed line gives the spectral characteristics of the scattered laser light.

Exposure of the sample to laser light with an intensity of  $10^{14}$  photons per  $\text{cm}^2$  and pulse for 300 s prior to the FLN measurement led to the lower spectrum of Fig. 34 which is labeled by „FLN & HB“. It exhibits a similar shape as the upper spectrum but reduced fluorescence intensity due to HB at the excitation wavelength of 680.5 nm. The observation that HB affects the entire FLN spectrum confirms that the PSB observed in the FLN spectra corresponds to the PSBH presented in Chapter 4.1.4.

#### 4.6.3 Effects Owing to Reabsorption

Remarkable effects owing to reabsorption were observed when measuring non-line-narrowed fluorescence spectra of LHC II at 4.2K (see Chapter 4.5.2). Thus, the dependence on the optical density of the sample was also investigated for FLN spectra. The results are shown in Fig. 35 for samples with an optical density (different optical pathlength of cuvettes) of 0.2 (dashed line),

0.4 (full line), and 1.0 (full line) at 676 nm and a constant chlorophyll concentration of 0.2 mg/ml at 4.2 K.

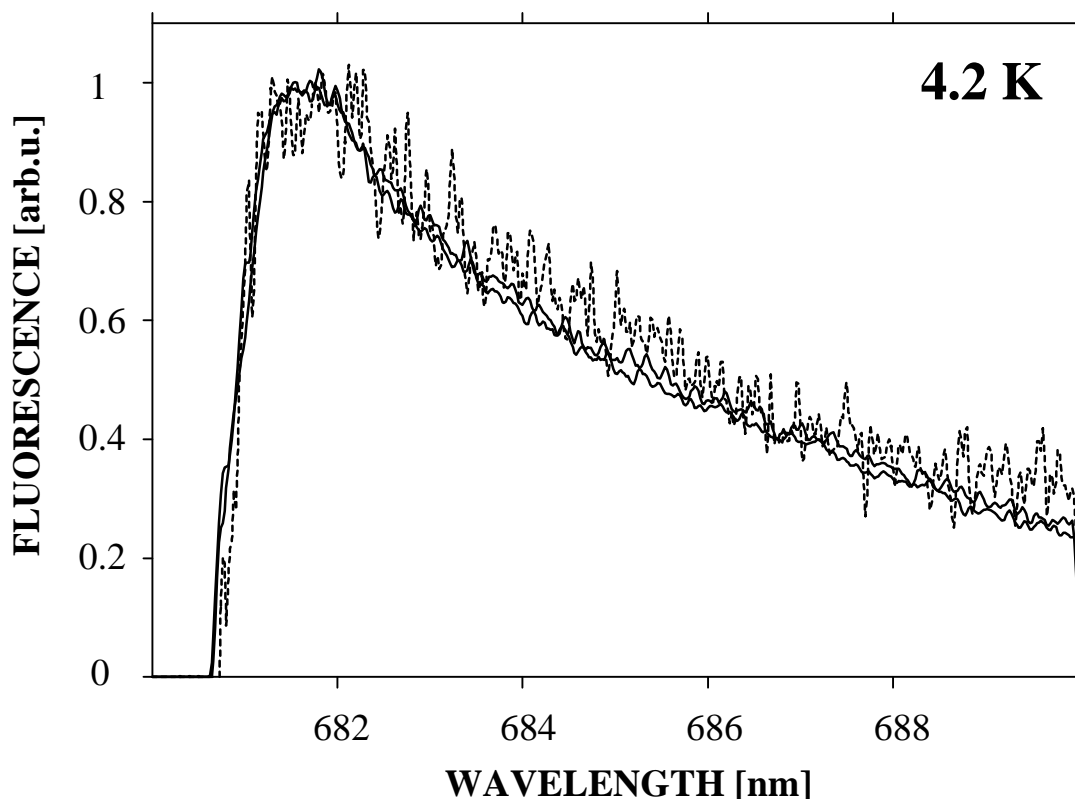


Figure 35. Selectively excited fluorescence spectra at 4.2 K (full lines) excited at 680.5 nm with a laser intensity of  $\sim 10^{13}$  photons per  $\text{cm}^2$  and pulse. The spectra were obtained for samples with an optical density (different optical pathlength of cuvettes) of 0.2 (dashed line), 0.4, and 1.0 (full lines) at 676 nm and a constant chlorophyll concentration of 0.2 mg/ml. The scattered laser light was subtracted before normalizing the spectra.

These OD values are similar to those used in the case of non-line-narrowed fluorescence spectra. In particular, the latter spectra were found to be virtually free from reabsorption for an OD of 0.2. The FLN spectra shown in Fig. 35 were excited at 680.5 nm with a laser intensity of  $\sim 10^{13}$  photons per  $\text{cm}^2$  and pulse at 4.2 K. The scattered laser light was subtracted before normalizing the spectra. It is apparent that variation of the OD of the sample did not lead to changes of the spectral shape of the line-narrowed fluorescence. Thus, the FLN spectra appear to be virtually free from reabsorption and were routinely measured using samples with the highest tested OD of 1.0 at 676 nm and a constant chlorophyll concentration of 0.2 mg/ml.

## 4.6.4 Excitation Wavelength Dependence

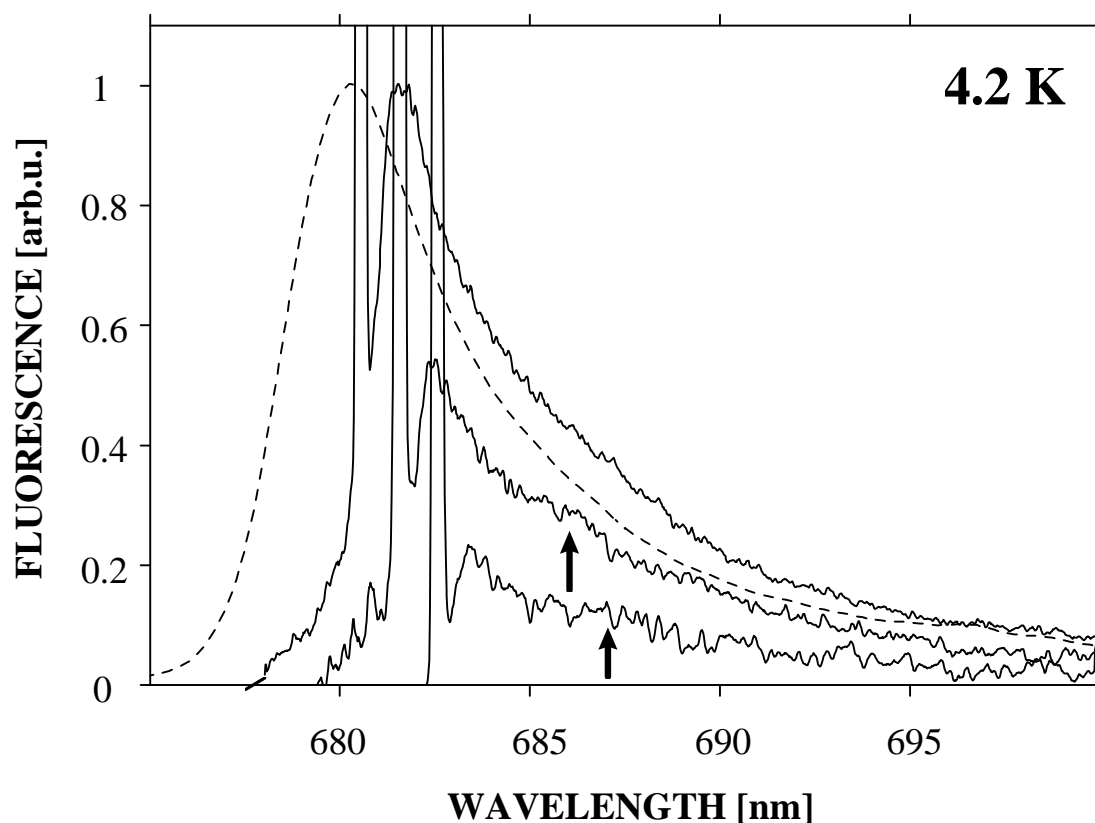


Figure 36. Selectively excited fluorescence spectra at 4.2 K (full lines) for a laser intensity of  $\sim 10^{13}$  photons per  $\text{cm}^2$  and pulse as well as excitation wavelengths of 680.5, 681.5 and 682.5 nm from left to right, respectively. The non-line-narrowed fluorescence spectrum (dashed line) excited at 645 nm is given for comparison.

Line-narrowed fluorescence spectra of LHC II obtained for different excitation wavelengths ( $\lambda_E$ ) within the fluorescence origin band at 4.2 K are shown in Fig. 36. To account for the wavelength dependence of the excitation intensity  $I_{\text{exc}}(\lambda_E)$  the spectra were re-normalized by a factor of  $I_{\text{exc}}(680.5 \text{ nm})/I_{\text{exc}}(\lambda_E)$ . The non-line-narrowed fluorescence spectrum excited at 645 nm is given for comparison (see dashed line in Fig. 36). Measurements of FLN spectra were restricted to  $\lambda_E > 680 \text{ nm}$  in order to minimize the extent of non-resonant excitation (Kikas, 1978). Furthermore, for  $\lambda_E < 680 \text{ nm}$  excitation of higher electronic states followed by EET to the lowest state has to be expected. This would result, most probably, in the FLN spectrum being superimposed with the non-line-narrowed fluorescence spectrum, i.e. in an additional loss of selectivity. All line-narrowed spectra peak about  $24 \text{ cm}^{-1}$  to the red of the excitation wavelength ( $\lambda_E$ ). This observation establishes, in agreement with the

HB data (see Chapter 4.1.2), that the lowest (fluorescing)  $Q_y$ -state of LHC II is mainly inhomogeneously broadened and the FLN spectrum predominantly represents the PSB. The peak value is similar to the results of Peterman et al. (1997) while the pseudo-PSBH was peaking at  $18 \text{ cm}^{-1}$  (see Chapter 4.1.4). Furthermore, the shape of the FLN spectra is characterized by a remarkable asymmetry (width of  $\sim 100 \text{ cm}^{-1}$ ) that resembles that of the non-line-narrowed fluorescence spectrum. At the first glance, this result seems to be in contrast with the relatively narrow PSBH (width of  $\sim 25 \text{ cm}^{-1}$ ). Nevertheless, a consistent interpretation of both, FLN and HB results, is possible as will be shown in Chapter 7. Tuning the excitation wavelength to the red, the fluorescence intensity decreases drastically, which is qualitatively consistent with the relatively narrow inhomogeneous width of the absorption band of the lowest state of  $< 90 \text{ cm}^{-1}$  (see Chapter 4.1.2). Furthermore, a weak shoulder at about  $90 \text{ cm}^{-1}$  seems to appear in the spectra obtained for  $\lambda_E$  of 681.5 and 682.5 nm. This may point to a further structure within the one-phonon profile (see Chapter 7.1.3).

## **5 Low-Energy Level Structure of LHC II**

With 12 Chl molecules per subunit it can be expected that 36  $Q_y$ -states contribute to the 4.2 K absorption spectrum of trimeric LHC II. In the absence of both, significant excitonic interactions between Chls of and structural heterogeneity among the different subunits of the trimer, this number may reduce to 12  $Q_y$ -states. Nine states were assigned in the region between ~ 650 and 676 nm based on the 77 K absorption, linear dichroism and circular dichroism spectra (Hemelrijk et al., 1992). However, no spectral feature indicated the existence of a low-energy state at ~ 680 nm that was later suggested based on HB spectroscopy at 4.2 K (Reddy et al., 1994), pump-probe experiments at room temperature (Schrötter et al., 1994; Kehrberg et al., 1995) and reabsorption studies (Voigt et al., 1996). In this regard, a careful inspection of the low-energy hole features presented in Chapter 4.1 may lead to a more detailed characterization of spectral positions and nature of the low-energy level structure of trimeric LHC II.

### **5.1 Assignment of the Lowest $Q_y$ -State**

The ZPH action spectrum is centered at 678.2 nm (see Fig. 20) and reflects the inhomogeneously broadened zero-phonon absorption profile of the lowest energy  $Q_y$ -state(s) of LHC II at 4.2 K. The burn fluence dependence of hole 1 obtained with excitation into higher energy bands (Frames A, B and C of Fig. 21) indicates, however, that the lowest (and fluorescing) energy  $Q_y$ -state is located at  $(679.8 \pm 0.2)$  nm. According to Eq. 12, the 4.2 K fluorescence origin band is shifted by  $S\omega_m$  to the red of the lowest energy  $Q_y$ -state. With the Huang-Rhys factor of  $S = 0.9$  and the phonon frequency of  $\omega_m = 18 \text{ cm}^{-1}$  obtained in Chapter 4.1.4,  $S\omega_m$  equals  $16 \text{ cm}^{-1}$  (0.8 nm) so that the fluorescence origin band should be located at 680.6 nm. The non-line-narrowed fluorescence spectrum obtained at 4.2 K is shown in Fig. 32. The origin band peaks at  $(680.3 \pm 0.2)$  nm, which is in good agreement with the predicted value. If the lowest energy state was at 678.2 nm, which is the maximum of the ZPH action spectrum, the predicted position of the origin band would be 678.8 nm. Thus, it can be concluded that the lowest energy  $Q_y$ -state

of trimeric LHC II is located at  $(679.8 \pm 0.2)$  nm and the ZPH action spectrum is contributed to by more than one low-energy  $Q_y$ -state.

### 5.2 Nature of the Low-Energy States

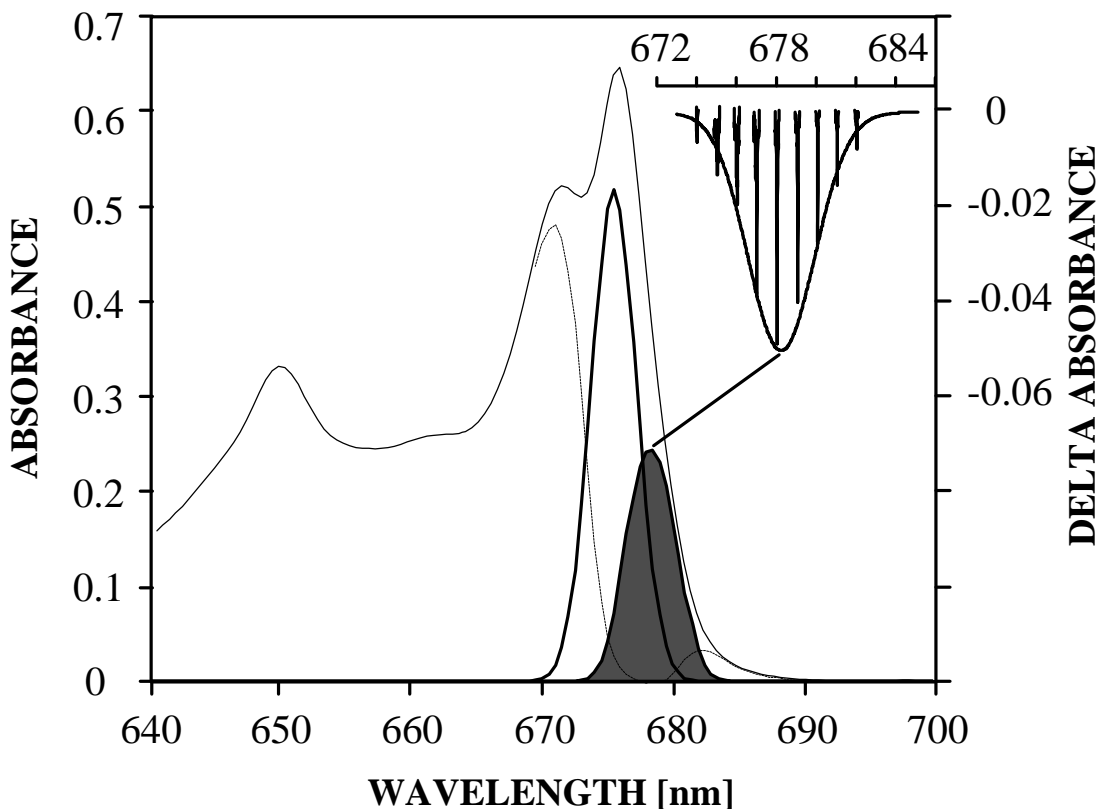


Figure 37. The 4.2 K absorption (from Fig. 19) and ZPH-action spectrum (from Fig. 20) of trimeric LHC II. The hatched profile indicates the position of the three lowest energy states associated with the ZPH-action spectrum. The profile to the left of the hatched one represents the next higher electronic state at  $\sim 676$  nm. The residual absorption is given by the dashed line.

In order to consider the nature of the above mentioned low-energy states an estimate of their contribution to the entire  $Q_y$ -absorption spectrum is required. It is reasonable to assume that the combined absorption profile of these low-energy states is the profile of the ZPH action spectrum centered at 678.2 nm and having a Gaussian width of  $\sim 90$   $\text{cm}^{-1}$  (see upper right corner of Fig. 37). An additional constraint was imposed by an analysis of the saturated hole depths near the center (678 nm) as well as within the low-energy wing (681 nm) of the ZPH action spectrum. As discussed in Chapter 4.1.4, the fractional depth of a saturated hole is given by  $\exp(-S)$ . An upper limit for the Huang-Rhys factor  $S$  of 0.9 was estimated from a saturated hole depth of 0.40 at

681 nm assuming that the absorption due to the 676 nm band is negligible at this wavelength (Fig. 37). Near the center of the ZPH action spectrum at 678 nm, however, a saturated hole depth of 0.24 was obtained. With the aforementioned Huang-Rhys factor  $S$  of 0.9 the expression  $\exp(-S)$  indicates that the lowest energy states contribute only by about 60 % to the full absorption at 678 nm, see shaded Gaussian profile in Fig. 37. Subtraction of the absorption due to these states from the experimental absorption spectrum yielded a Gaussian shape for the low-energy side of the 676 nm band with a width of  $\sim 90 \text{ cm}^{-1}$ , see profile to the immediate left of the shaded profile in Fig. 37. With the integration truncated at 640 nm the low-energy states represented by the ZPH action spectrum account for  $\sim 9 \%$  of the total  $Q_y$ -absorption. When estimating the number of Chl molecules contributing to the low-energy states 15 Chl *b* and 21 Chl *a* molecules per LHC II trimer have to be taken into account according to Kühlbrandt et al. (1994). Furthermore, it was assumed that the ratio of the dipole strengths of Chl *b* and Chl *a* is 1.64 as reported for the molecules dissolved in ether (Lichtenthaler, 1987). Then, the value of 9 % corresponds to absorption by 2.7 Chl *a* molecules per LHC II trimer ( $\sim 0.9$  Chl *a* per subunit). The Gaussian profile of the 676 nm band shown in Fig. 37 carries twice the intensity of the shaded profile and, therefore, has the absorption strength of  $\sim 6$  Chl *a* molecules per LHC II trimer.

The finding that the absorption strength of the lowest state(s) represented by the ZPH action spectrum corresponds to approximately one Chl *a* molecules per subunit suggests that each of these states is localized on one Chl *a* molecule of a subunit of the LHC II trimer. Within this picture there would be three low-energy states within the LHC II trimer, which are expected to be degenerate in the absence of inter-subunit Chl-Chl interactions and energy disorder due to structural heterogeneity. The burn fluence dependence of hole 1 discussed in Chapter 4.1.3, however, led to the assignment of the lowest energy state at 679.8 nm, 1.6 nm lower in energy than the center of the action spectrum, and indicated the presence of more low-energy states within the ZPH action spectrum. This means that there would need to be two non-degenerate states absorbing near 678 nm, which are not resolved in the hole-burned spectra. This seems reasonable since the envelope of the ZPH action

spectrum of Fig. 20 can be fit with three Gaussians of equal width ( $80 \text{ cm}^{-1}$ ) and intensity, which are centered at 679.8, 678.4 and 677.1 nm (not shown). The width of  $80 \text{ cm}^{-1}$  was chosen because it is the width of the 679.8 nm hole shown in Frame C of Fig. 21. Thus, the inhomogeneous width of the low-energy states is  $\sim 80 \text{ cm}^{-1}$  while the width of the ZPH action spectrum of Fig. 20 ( $\sim 90 \text{ cm}^{-1}$ ) results from the superposition of their zero-phonon absorption bands. The splitting between the three levels is  $\sim 30 \text{ cm}^{-1}$ . Each state should be quite highly localized on individual subunits for an inter-subunit Chl a-Chl a coupling  $\sim 5 \text{ cm}^{-1}$  (Voigt et al., 1996) and an energy inequivalence of  $30 \text{ cm}^{-1}$  (Wu and Small, 1998). Therefore, it appears that the degeneracy of the low-energy states is removed due to structural heterogeneity among the subunits of the LHC II trimer. This interpretation is further supported by the results obtained for monomeric CP29. The burn fluence dependence of hole 1 that led to the assignment of three low-energy states for trimeric LHC II was absent for the analogous feature in the hole-burned spectra of CP29 (see Chapter 4.3). Rather, a single low-energy  $Q_y$ -state was found to be located at  $\sim 678.4 \text{ nm}$ . In addition, the presence of three low-energy  $Q_y$ -states in trimeric LHC II has recently been confirmed by single molecule spectroscopy (Jelezko, personal communication).

### ***5.3 Pigment-Pigment Coupling Strengths***

The discussion of the low-energy hole features in the preceding chapter led to the assignment of three low-energy states at 677.1, 678.4 and 679.8 nm with the latter state being the lowest and fluorescent  $Q_y$ -state of trimeric LHC II at 4.2 K. The absorption strength of each state corresponds approximately to that of one Chl a molecule. Therefore, it was concluded that these states are highly localized on a single Chl a molecule of each subunit of the LHC II trimer.

Other approaches for gauging the extent of excitonic coupling involve the satellite hole structure as well as the pressure dependence of absorption bands and hole features. As to the first, HB in any excitonic level of systems of strongly coupled chromophores should produce responses from the other exciton levels, which would appear as persistent satellite holes (see Chapter 2.5). It is apparent from the hole spectra of Figs. 19 and 22 that HB

within the lowest energy states (hole 1) results in only weak satellite holes associated with the higher energy absorption bands. Hole 2 is located at ~648 nm, i.e. almost coincident with the 650 nm band, and has a width of ~125 cm<sup>-1</sup> (Figs. 19 and 22). From Fig. 22 it is apparent that another satellite hole at ~672 nm (hole 3) interferes with the anti-hole of hole 1. No satellite holes were observed when selectively burning in the spectral range of the lowest states (not shown). It appears, therefore, that the Chl *a* molecule associated with the lowest energy state of the subunit is weakly coupled to the Chl *b* molecules responsible for the 650 nm band. This is in agreement with the preliminary assignment of Chl *a* and *b* molecules (Kühlbrandt et al, 1994) and excitonic calculations (T. Renger, 1995, 1996), which reveal that the largest interaction energies can be expected within Chl *b/a* dimers. On the other hand, the weakness of the satellite hole structure might suggest a second interpretation. Conformational changes of the protein induced by NPHB may not be confined to the immediate region around the excited Chl *a* molecule but spatially extended. Thus, the transition frequencies of other Chl molecules may be altered in the absence of significant Chl-Chl interactions.

There is very little satellite hole activity between ~ 650 and 671 nm. The anti-hole of hole 1 marked with an asterisk in Fig. 19 interferes with the weak satellite hole of the 671 nm band, which is labeled as hole 3 in Fig. 22. This may indicate weak coupling between the Chl *a* molecule associated with the lowest state of the subunit and the Chl *a* molecule responsible for the 671 nm band. However, hole 3 appears in hole spectra obtained with high burn fluence when hole 1 is close to saturation. Therefore, it is more likely that the latter satellite hole actually builds on hole 2 associated with the main Chl *b* band. Then, the satellite hole structure would represent weak excitonic coupling of the Chl *b* and the Chl *a* molecules associated with the 650 nm and the 671 nm bands, respectively.

In recent years high pressure has been combined with low-temperature absorption and HB spectroscopies in order to assess the strength of excitonic couplings in photosynthetic complexes (see e.g. Reddy et al., 1996). As discussed in Chapter 2.5, shift rates of -0.05 to -0.15 cm<sup>-1</sup>/MPa have been

determined for the  $S_1$ -states of isolated chromophores embedded in glass, polymer and protein hosts, while shift rates with absolute values higher than  $\sim 0.2 \text{ cm}^{-1}/\text{MPa}$  may indicate that excitonic interactions within an photosynthetic complex are relatively strong (see e.g. Reddy et al., 1996 and references therein). The absolute values of the shift rates observed for the main absorption bands of trimeric LHC II at 650, 671 and 676 nm are smaller than  $-0.1 \text{ cm}^{-1}/\text{MPa}$  at 77 K (see Chapter 4.4 as well as Figs. 29 and 30) and, therefore, comparable to those reported for isolated chromophores in amorphous hosts, *vide supra*. Thus, it appears that the shift rates are dictated by protein-Chl interactions. In addition, it has already been shown theoretically that excitonic interactions in the LHC II subunit are too weak to significantly affect the shift rates (Pieper et al., 1999a). In that work the theoretical analysis given in Wu et al. (1998) for the B850 and B875 antenna rings of purple bacteria was reduced to the case of a heterodimer using second order perturbation theory. This seemed to be reasonable in the case of LHC II because the largest interaction energies  $V$  of  $\sim 150 \text{ cm}^{-1}$  are expected for Chl *a/b* dimers (T. Renger et al., 1995, 1996) while the energetic splitting  $\Delta E$  between the monomer energies is  $\sim 600 \text{ cm}^{-1}$ . The estimated contribution to the shift rate for the given values of  $V$ ,  $\Delta E$  and  $\kappa = 0.1 \text{ GPa}^{-1}$  (see Chapter 2.5) is  $\sim 0.005 \text{ cm}^{-1}/\text{MPa}$ , which is one order of magnitude lower than the observed shift rates. The upper and lower heterodimer levels, however, shift to higher and lower energies, respectively, so that their shift rates add destructively and constructively to the negative rate from protein-Chl interactions. The expected difference in the overall pressure shift rates of  $\sim 0.01 \text{ cm}^{-1}/\text{MPa}$  may explain the faster red-shifting of the 671 and 661 nm absorption bands compared to that of the 650 nm band. In particular, the 661 nm band disappears/ merges with the 671 and 676 nm bands at pressures  $\geq 200 \text{ MPa}$  precluding an exact determination of its shift rate. If so, the Chl *a* molecules associated with the 671 and 661 nm absorption bands would be in close contact to Chl *b* molecules. The shift rate for ZPH burned selectively within the lowest state(s) at 12 K of about  $-0.08 \text{ cm}^{-1}/\text{MPa}$  (see Fig. 31) is nearly the same as those observed for the higher energy states. This is consistent with the low-energy states being dominated by a single Chl *a* molecule of the subunit that is weakly

coupled to others.

In summary, three low-energy states at 677.1, 678.4 and 679.8 nm were assigned for trimeric LHC II with the latter state being the lowest and fluorescent  $Q_y$ -state at 4.2 K. The absorption strength of each state corresponds approximately to that of one Chl *a* molecule per LHC II trimer. Furthermore, the weak satellite hole structure produced by HB of the low-energy states as well as their small pressure shift rates indicate that each of these states is highly localized on a single Chl *a* molecule of the corresponding subunit of the LHC II trimer. It is possible, however, that these Chl *a* molecules are weakly coupled to Chl *b* molecules associated with the 650 nm absorption band.

Both, the observed satellite hole structure as well as the differences in the pressure shift rates of the 650, 661 and 671 nm absorption bands are consistent with weak excitonic coupling with interaction energies of up to  $150 \text{ cm}^{-1}$  between the corresponding Chl *a* and Chl *b* molecules as reported by T. Renger et al. (1995, 1996).

## 6 Excitation Energy Transfer in LHC II

### 6.1 Chl b-Chl a Excitation Energy Transfer

Qualitatively, the population decay time ( $T_1$ ) of an excited state is reflected in the ZPH burning efficiency, i.e. HB is less efficient for excited states with short lifetimes (see Chapter 2.2.2). The burn efficiencies for  $660 \text{ nm} \leq \lambda_B \leq 674 \text{ nm}$  were found to be more than an order of magnitude lower than for  $\lambda_B \approx 674 \text{ nm}$ . A further decrease of the burn efficiencies by about a factor of 5 was observed for  $640 \text{ nm} \leq \lambda_B \leq 655 \text{ nm}$ . The observation of the lower burn efficiency for  $\lambda_B$  within the 650 nm absorption band is consistent with short lifetimes of the corresponding excited states, i.e. ultrafast Chl *b*  $\rightarrow$  Chl *a* EET. From time resolved (pump-probe) experiments with excitation within the 650 nm band Bittner et al. (1995) reported fast ( $\sim 310 \text{ fs}$ ) and slow ( $\sim 1 \text{ ps}$ ) time constants for Chl *b*  $\rightarrow$  Chl *a* EET at 12 K. Similar values were determined in other studies at room temperature (Du et al., 1994; Bittner et al., 1994; Conelly et al., 1997) indicating that the temperature dependence of the EET kinetics is weak.

An analysis of the widths of holes burned into the 650 nm band (see Fig. 19) may permit a quantitative determination of the Chl *b*  $\rightarrow$  Chl *a* EET rates. The upper hole-burned spectrum (a) of Fig. 19 was obtained with  $\lambda_B = 648.6 \text{ nm}$ . One can observe a broad hole at  $\sim 648 \text{ nm}$  (hole 2) with a width of  $\sim 125 \text{ cm}^{-1}$  superimposed with a relatively sharp ZPH. Similar spectra were obtained for several burn wavelengths between 648 and 651 nm. From these spectra it was determined that the widths of the relatively sharp ZPH (fractional depths of  $\sim 0.02$ ) coincident with  $\lambda_B$  fall in the range of  $7\text{-}8 \text{ cm}^{-1}$ . It is reasonable to associate the width of  $\sim 8 \text{ cm}^{-1}$  with EET from a Chl *b* state to lower energy states because the contribution from pure dephasing is expected to be negligible for total dephasing times shorter than 10 ps (Völker, 1989). Since the ZPH width ( $\Gamma_{\text{hole}}$ ) is twice the homogeneous width  $\gamma$  (see Chapter 2.4.4), the lifetime is given by  $(\pi c \Gamma_{\text{hole}})^{-1}$ , where  $c$  is the speed of light. Then, the holewidth of  $\sim 8 \text{ cm}^{-1}$  corresponds to a lifetime of  $\sim 1 \text{ ps}$ . This value is in almost perfect agreement with the „slow“ EET component reported by Bittner et al. (1995), *vide supra*.

The broad hole 2 at  $\sim 648$  nm with a width of  $\sim 125$   $\text{cm}^{-1}$  is observed for burn wavelengths within the 650 nm band (see spectrum a in Fig. 19) as well as for burn wavelengths lying at lower energies (see spectra b and c in Fig. 19). This finding establishes, as discussed in Chapter 5.2, that hole 2 builds on hole 1, which is inhomogeneously broadened. Therefore, the observed width  $\Gamma_{\text{hole}}$  should roughly be  $\Gamma_{\text{hole}} \approx \Gamma_{\text{inh}} + \Gamma_{\text{ZPH}}$  where  $\Gamma_{\text{ZPH}}$  is the width of a ZPH burned directly into the 650 nm band. In the case of hole 2, however,  $\Gamma_{\text{ZPH}}$  becomes comparable to  $\Gamma_{\text{inh}}$ , which was determined to be  $\sim 80$   $\text{cm}^{-1}$  for the lowest state(s). Thus, the relationship  $\Gamma_{\text{ZPH}} = 2\gamma$  breaks down and  $\Gamma_{\text{ZPH}} \approx \gamma$  (Johnson and Small, 1991). Then, the width of hole 2 equals  $\Gamma_{\text{hole}} \approx \Gamma_{\text{inh}} + \gamma$ , which corresponds to a ZPH width of  $\sim 45$   $\text{cm}^{-1}$  and yields a lifetime of  $\sim 240$  fs. Therefore, hole 2 may represent the „fast“ (310 fs) EET component determined by Bittner et al. (1995), *vide supra*. The discrepancy can be understood assuming that the 650 nm band is contributed to by more than one state, i.e. hole 2 could be the superposition of two unresolved holes.

## **6.2 Chl a-Chl a Excitation Energy Transfer**

In analogy to the discussion given in the preceding chapter, the time constants of Chl a  $\rightarrow$  Chl a EET may be reflected in the widths of holes burned into the 676 nm band. The widths ( $\Gamma_{\text{hole}}$ ) and fractional absorbance changes ( $\Delta A/A$ ) of the ZPH associated with the action spectrum of Figs. 20 and 37 are given in Table 2. It was discussed in Chapter 4.1.2 that the magnitude of the latter holewidths may become comparable to the read resolution of  $0.3$   $\text{cm}^{-1}$ . In this case, the holewidth is given by  $\Gamma_{\text{hole}} = 2\gamma + 0.3$ . Thus, the homogeneous widths of the ZPL given in Table 2 were obtained using  $\gamma = (\Gamma_{\text{hole}} - 0.3)/2$ .  $\Gamma_{\text{hole}}$  is constant for  $\lambda_B \geq 679.0$  nm and increases for  $\lambda_B < 679.0$  nm. Since the fractional  $\Delta A/A$ -values are lower than 0.1 for the ZPH burned at 675.0, 676.0 and 677.0 nm it is unlikely that their widths are significantly contributed to by saturation broadening (see Lee et al., 1989). The total dephasing times ( $T_2$ ) corresponding to the  $\gamma$ -values obtained for the latter three holes are 12, 15 and 20 ps, respectively, see Table 2. In addition, the contribution from pure dephasing should be negligible, *vide supra*. Then, the lifetimes ( $T_1$ ) are  $\sim 6$ , 8 and 10 ps since  $T_2 = 2 T_1$ . The  $T_1$ -times are in good agreement with the values

reported by Savikhin et al. (1994) at 13 K on the basis of pump-probe anisotropy decays at 675 and 677 nm. The lifetimes ( $T_1$ ) can be attributed to downward EET from states associated with the 676 nm band although for  $\lambda_B = 677$  nm the possibility of inter-subunit EET from the subunit with the highest energy for the lowest state to the 678.4 and 679.8 nm states of the other two subunits of the LHC II trimer, see Chapter 5, cannot be excluded.

Table 2 Zero-phonon holewidths and dephasing times as obtained by ZPH-action spectroscopy at 4.2 K (see Fig. 20)

$\lambda_B$ (nm)	675.0	676.0	677.0	678.0
$\Delta A/A^a$	0.02	0.03	0.07	0.12
$\Gamma_{\text{hole}} (\text{cm}^{-1})^b$	$2.0 \pm 0.4$	$1.7 \pm 0.4$	$1.2 \pm 0.3$	$0.8 \pm 0.2$
$\gamma (\text{cm}^{-1})^c$	$0.9 \pm 0.2$	$0.7 \pm 0.2$	$0.5 \pm 0.2$	$0.3 \pm 0.1$
$T_2$ (ps) <sup>d</sup>	$12 \pm 3$	$15 \pm 5$	$20 \pm 10$	$40 \pm 10$
$\lambda_B$ (nm)	679.0	680.0	681.0	682.0
$\Delta A/A^a$	0.16	0.17	0.17	0.13
$\Gamma_{\text{hole}} (\text{cm}^{-1})^b$	$0.7 \pm 0.2$	$0.5 \pm 0.1$	$0.5 \pm 0.1$	$0.5 \pm 0.1$
$\gamma (\text{cm}^{-1})^c$	$0.2 \pm 0.1$	$\sim 0.1$ (0.073) <sup>e</sup>		
$T_2$ (ps) <sup>d</sup>	$\sim 100$	- <sup>f</sup>		

a) Fractional absorbance change of hole. b) Measured holewidth, uncorrected for read resolution of  $0.3 \text{ cm}^{-1}$ . c) Homogeneous width of zero-phonon line, corrected for read resolution of  $0.3 \text{ cm}^{-1}$  using  $\Gamma_{\text{hole}} = 2\gamma + 0.3 \text{ cm}^{-1}$ . d) Total optical dephasing time given by  $T_2 = (\pi \gamma c)^{-1}$ . e) Value in brackets determined with a resolution of  $0.001 \text{ cm}^{-1}$ . f) Resolution inadequate for determination.

### 6.3 Pure Dephasing

Turning to the ZPH burned for  $679.0 \leq \lambda_B \leq 682.0$  nm it is apparent from Table 2 that the read resolution of  $0.3 \text{ cm}^{-1}$  is too low to permit determination of the  $T_2$ -values. Furthermore, the fractional  $\Delta A/A$ -values are  $> 0.1$  so that the holes may be contaminated by some saturation broadening (Lee et al., 1989). Using  $\gamma = (\Gamma_{\text{hole}} - 0.3)/2$ , *vide supra*, the homogeneous width of the ZPL should

be smaller than  $0.1 \text{ cm}^{-1}$ . Since the 679.8 nm state was assigned as the lowest and fluorescent state of trimeric LHC II at 4.2 K, its  $T_1$ -value should equal the fluorescence lifetime of  $\sim 5.6 \text{ ns}$  (Vasil'ev, 1997a), which corresponds to  $\gamma \sim 0.001 \text{ cm}^{-1}$  in the absence of pure dephasing. However, shallow ZPH ( $\Delta A < 10 \%$ ) with holewidths of 0.074, 0.146, and  $0.600 \text{ cm}^{-1}$  were obtained in high-resolution ( $< 30 \text{ MHz}$ ) experiments in the fluorescence excitation mode with burn wavelengths between 681 and 682 nm for temperatures of 1.9, 4.7, and 9.2 K, respectively. The temperature dependence of the holewidth follows an  $T^A$  power law with  $A = (1.3 \pm 0.1)$  (not shown). This finding establishes that the homogeneous width of the 679.8 nm-state is determined by pure dephasing stemming from the glass-like nature of the protein (see, e.g., Hayes et al., 1988a; Völker, 1989). In particular, the homogeneous width is  $0.073 \text{ cm}^{-1}$  at 4.7 K corresponding to a pure dephasing time  $T_2'$  of  $\sim 150 \text{ ps}$ . Optical dynamics dictated by pure dephasing/ spectral diffusion for  $T \geq 15 \text{ K}$  was also reported, for example, for the lowest energy exciton level of the B850 BChl *a* antenna complex of *Rhodospseudomonas acidophila* (Wu et al., 1997). The absence of EET from the 679.8 nm-state provides further support for its assignment as lowest  $Q_y$ -state of trimeric LHC II.

## 7 Electron-Phonon Coupling in LHC II

The position of the lowest  $Q_y$ -state at  $(679.8 \pm 0.2)$  nm, an inhomogeneous width  $\Gamma_{inh}$  of  $(80 \pm 10)$   $\text{cm}^{-1}$  as well as a high degree of localization on one Chl a molecule for the three low-energy  $Q_y$ -states of trimeric LHC II were determined in the preceding two chapters. Basic parameters of electron-phonon coupling, however, such as the Huang-Rhys factor  $S$  of 0.9 and the phonon frequency  $\omega_m$  of  $\sim 18$   $\text{cm}^{-1}$  determined in HB experiments (see Chapter 4.1.4) have so far only been used to estimate the shift  $S\omega_m$  between the *peak positions* of zero-phonon absorption profile and fluorescence origin band in Chapter 5. The scope of the following chapter is a detailed theoretical simulation of the 4.2 K line-narrowed spectra (see Chapters 4.1.4 and 4.6) in order to thoroughly characterize the electron-phonon coupling of the lowest  $Q_y$ -state of trimeric LHC II including the shape of the one-phonon profile which is related to the spectral density of phonon modes.

### 7.1 Analysis of Line-Narrowed Spectra

As already mentioned in Chapter 4, the PSB structure observed in FLN and HB spectra of LHC II at 4.2 K exhibits apparent differences in shape and peak position. HB with  $\lambda_B = 681$  nm revealed a pseudo-PSBH peaking at  $\sim 18$   $\text{cm}^{-1}$  and having a width of only  $\sim 25$   $\text{cm}^{-1}$  (Chapter 4.1.4). Complementary FLN experiments with  $\lambda_E$  of 680-683 nm yielded much broader sidebands peaking at  $\sim 24$   $\text{cm}^{-1}$  and having a width of  $\sim 100$   $\text{cm}^{-1}$  (Chapter 4.6). These discrepancies are also reflected in the results of previous HB (Reddy et al., 1994) and FLN studies (Peterman et al., 1997), cf. Chapter 1.2. A key observation from the FLN experiments is that the width of the PSB of  $\sim 100$   $\text{cm}^{-1}$  may compete with the inhomogeneous width of  $\sim 80$   $\text{cm}^{-1}$ , *vide supra*. However, most of the theoretical model calculations of line-narrowed spectra presented so far assumed that  $\Gamma_{inh} \gg \Gamma$ , where  $\Gamma$  is the width of the one-phonon profile (see e.g. Personov, 1983; Hayes et al., 1988b). Therefore, the complexities associated with interpretation of phonon structure in FLN and HB spectra will be discussed in the next chapter by theoretically analyzing the different (PSB) contributions in the  $\Gamma_{inh} > \Gamma$  as well as in the  $\Gamma_{inh} \approx \Gamma$  regime. Results are presented that

appear to explain the discrepancy between the HB and FLN results for the LHC II complex.

**7.1.1 Analysis of Phonon Structure in Line-Narrowed Spectra**

The discussion of the PSB contributions to line-narrowed spectra in the low-temperature limit will be based on the theory reviewed in Chapter 2.4. Application of a theory valid for (isolated) chromophores in amorphous hosts appears to be justified because of the high degree of localization found for the lowest state of LHC II (see Chapter 5.2). To illustrate the essential physics it is sufficient to consider the short burn time limit expression of Hayes et al. (1988b) for the hole-burned spectrum which is given by

$$\Delta A(\omega) = \sum_{R,P=0}^{\infty} \left( S^R \frac{e^{-S}}{R!} \right) \left( S^P \frac{e^{-S}}{P!} \right) \int d\Omega_0 N(\Omega_0 - \omega_c) \times \quad .(19)$$

$$l_P(\omega_B - \Omega_0 - P\omega_m) l_R(\omega - \Omega_0 - R\omega_m)$$

Eq. 19 was discussed in detail in Chapter 2.4. Briefly, S is the Huang-Rhys factor and  $N(\Omega_0 - \omega_c)$  the inhomogeneous distribution function (IDF), which is assumed to be a Gaussian centered at  $\omega_c$  and having a width of  $\Gamma_{inh}$ . It is important to recall that the terms  $l_P$  (for  $P \geq 0$ ) describe the purely electronic transitions bleached by HB with a burn frequency  $\omega_B$  while the terms  $l_R$  (for  $R \geq 0$ ) represent the homogeneously broadened absorption spectrum of each of the latter electronic transitions. In particular,  $l_0$  is the Lorentzian ZPL located at  $\Omega_0$  and having a width of  $\gamma$ . The  $R=1,2,\dots$  terms correspond to the one-phonon and multi-phonon ( $R \geq 2$ ) transitions with  $l_1$  being the one-phonon profile and  $\omega_m$  the mean phonon frequency. Thus, the  $P = 0$  and  $P \geq 1$  terms represent the electronic transitions which are resonantly and non-resonantly bleached, respectively.

The corresponding FLN spectrum given by

$$F(\omega) = \sum_{R,P=0}^{\infty} \left( S^R \frac{e^{-S}}{R!} \right) \left( S^P \frac{e^{-S}}{P!} \right) \int d\Omega_0 N(\Omega_0 - \omega_c) \times \quad (20)$$

$$l_P(\omega_E - \Omega_0 - P\omega_m) l_R(\omega - \Omega_0 + R\omega_m)$$

is derived from Eq. 19 replacing  $\omega_B$  by  $\omega_E$  (excitation frequency) and  $-R\omega_m$  by  $+R\omega_m$  (see Chapter 2.4), i.e. the terms  $l_R$  now represent the homogeneously

broadened fluorescence spectrum.

*Table 3 Parameters of the model calculations shown in Fig. 38 and 39*

temperature	T [K]	5
position of IDF	$\omega_C$ [cm <sup>-1</sup> ]	0
burn / excitation frequency	$\omega_{B/E}$ [cm <sup>-1</sup> ]	0
homogeneous width	$\gamma$ [cm <sup>-1</sup> ]	0.4
inhomogeneous width	$\Gamma_{inh}$ [cm <sup>-1</sup> ]	80
Huang-Rhys factor	S	1.0
peak phonon frequency	$\omega_m$ [cm <sup>-1</sup> ]	15
FWHM of Gaussian wing	$\Gamma_G$ [cm <sup>-1</sup> ]	15
FWHM of Lorentzian wing	$\Gamma_L$ [cm <sup>-1</sup> ]	20 <sup>a</sup> /100 <sup>b</sup>
FWHM of one-phonon profile	$\Gamma$ [cm <sup>-1</sup> ]	17.5 <sup>a</sup> /57.5 <sup>b</sup>

a)  $\Gamma_L$  and  $\Gamma$  used for the calculations shown in Fig. 38

b)  $\Gamma_L$  and  $\Gamma$  used for the calculations shown in Fig. 39

Following the approach of Mc Colgin (1975) for FLN spectra, four contributions to line-narrowed spectra can be defined. The ZPH (ZPL) located at  $\omega_B$  ( $\omega_E$ ) is obtained for R,P=0 in Eqs. 19 and 20 (contribution a). The P=0, R $\geq$ 1 terms (contribution b) represent phonon transitions that build on the ZPH (ZPL) and form the real-PSB. The R=0, P $\geq$ 1 terms (contribution c) correspond to electronic transitions which are non-resonantly bleached (excited) at  $\omega_B$  ( $\omega_E$ ) via multi-phonon transitions and constitute the pseudo-PSB. Finally, the R,P $\neq$ 0 multi-phonon terms, i.e. the (integrated) phonon wing(s) of contribution c, will be referred to as contribution d.

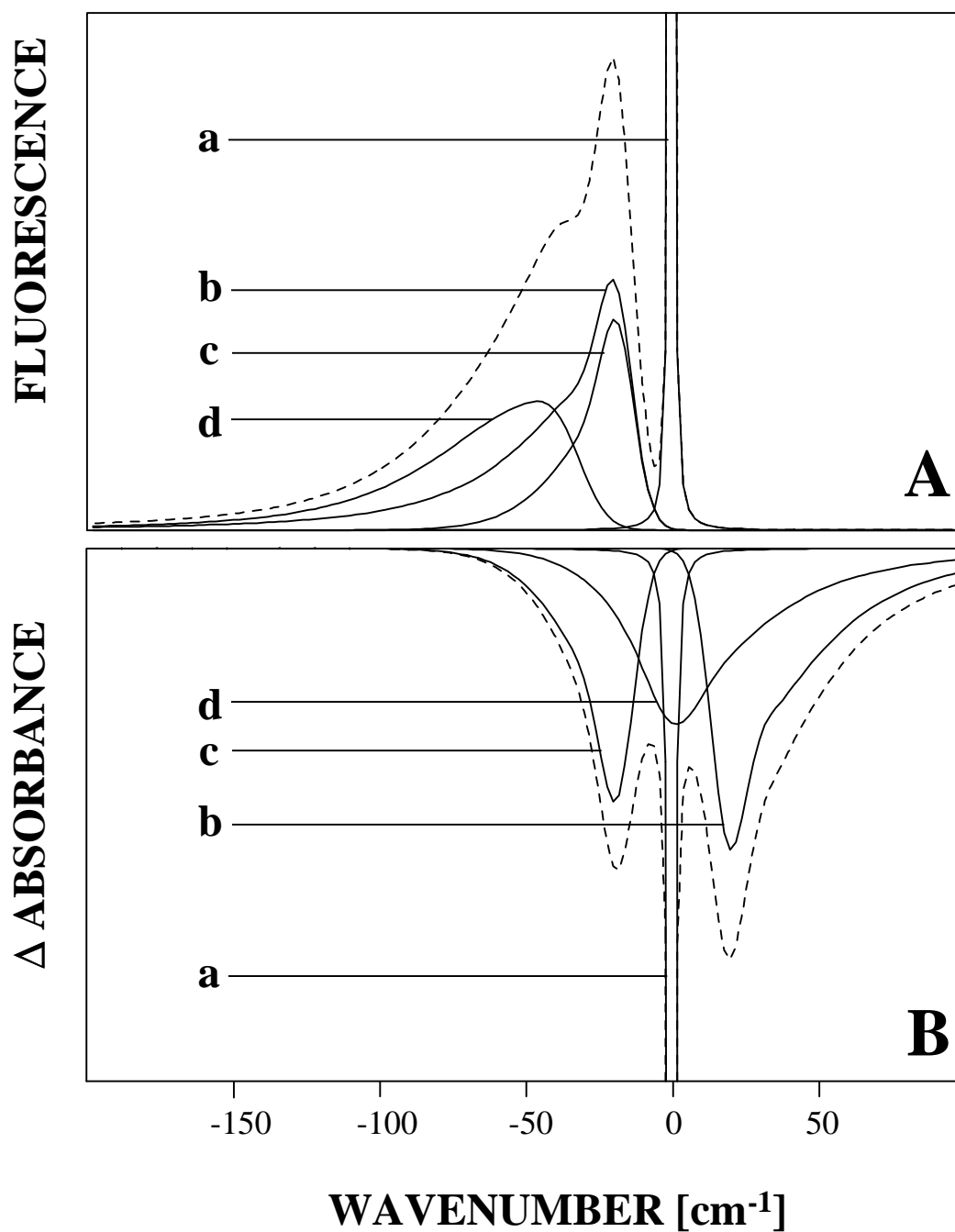


Figure 38. Low-temperature hole-burned (frame B) and line-narrowed fluorescence (frame A) spectra (dashed lines) calculated according to Eqs. 19 and 20, respectively, for illustration of the  $G_{inh} \gg G$  regime. The model system is defined in Table 3. In frames A and B, the full lines represent the ZPH (a) and multi-phonon contributions (b)-(d). The zero-phonon lines are cut off at 4% of their peak intensity value.

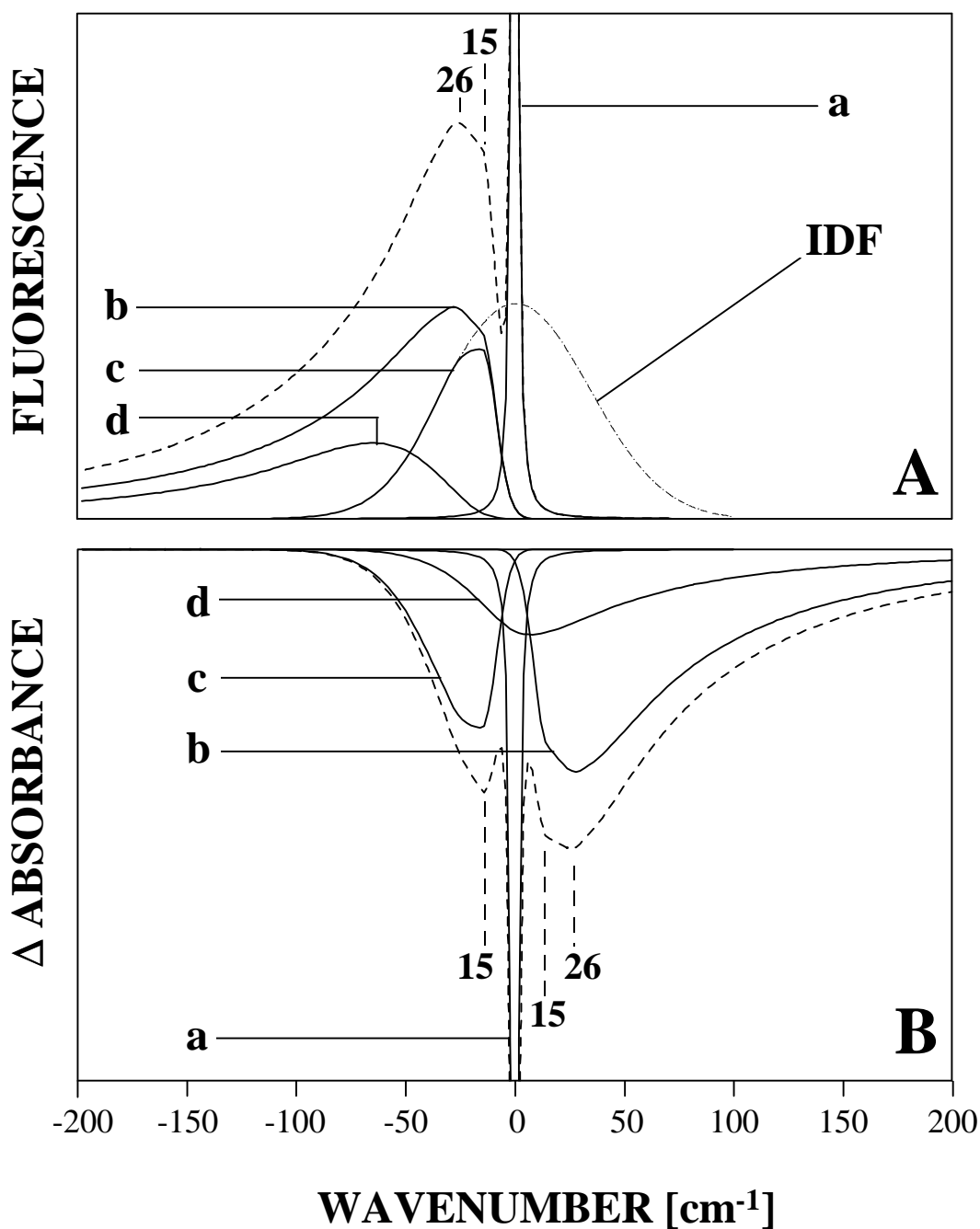


Figure 39. Low-temperature hole-burned (frame B) and line-narrowed fluorescence (frame A) spectra (dashed lines) calculated according to Eqs. 19 and 20, respectively, for illustration of the  $G_{inh} \sim G$  regime. The model system is defined in Table 3. In frames A and B the full lines represent the ZPH (a) and multi-phonon contributions (b)-(d). The zero-phonon lines are cut off at 4% of their peak intensity value. The dashed-dotted line represents the profile of the inhomogeneous distribution function (IDF).

Fig. 38 shows calculated FLN (Frame A) and HB (Frame B) spectra (dashed curves) representing the  $\Gamma < \Gamma_{inh}$  regime<sup>3</sup>. The model system is defined by the parameters given in Table 3. Especially,  $\Gamma = 17.5 \text{ cm}^{-1}$  ( $\Gamma_G = 15 \text{ cm}^{-1}$ ,  $\Gamma_L = 20 \text{ cm}^{-1}$ ), and  $\omega_E (\omega_B) = \omega_C \equiv 0$ .  $\Gamma_G$  and  $\Gamma_L$  are the widths of the Gaussian and Lorentzian profiles which determine the low- and high-energy wings of the asymmetric one-phonon profile, respectively, so that  $\Gamma = (\Gamma_G + \Gamma_L)/2$ . Comparison of Frames A and B reveals that the real- and pseudo-PSB features (contributions b and c) lie on the high- and low-energy sides of the ZPH in the HB spectrum, respectively. In contrast to this, the FLN spectrum is the superposition of both, features b and c, with contribution d on the low-energy side of the ZPL. Since feature d represents the phonon wings of the ZPL associated with the pseudo-PSB (contribution c), it peaks near 0 for HB and near  $2 \omega_m$  for FLN. It has to be noted that feature d contributes significantly to the tailing of the PSB in the FLN spectrum. Furthermore, it is obvious in Frames A and B that the real- and pseudo-PSB obey mirror symmetry in the  $\Gamma < \Gamma_{inh}$  regime. As such, they are comparable to the model calculations presented in Chapter 2.4.

Calculated FLN (Frame A) and HB (Frame B) spectra (dashed curves) for the  $\Gamma \approx \Gamma_{inh}$  regime are shown in Fig. 39. The calculations were performed with the same parameter values used above (see Table 3) except for  $\Gamma = 57.5 \text{ cm}^{-1}$  ( $\Gamma_G = 15 \text{ cm}^{-1}$ ,  $\Gamma_L = 100 \text{ cm}^{-1}$ ), i.e. the Lorentzian tailing of the one-phonon profile may exceed  $\Gamma_{inh}$ . It is obvious from Fig. 39 that the general composition of the line-narrowed spectra is the same as above. Most striking, however, is that the real- (contribution b) and pseudo-PSB (contribution c) exhibit apparently different shapes. The numbers in Fig. 39 correspond to the displacements of PSB features (in  $\text{cm}^{-1}$ ) measured relative to the ZPL (ZPH) at  $0 \text{ cm}^{-1}$ . The PSB of the dashed FLN spectrum and the real-PSB of the dashed HB spectrum show features at  $15$  and  $26 \text{ cm}^{-1}$  that correspond to one- and two quantum transitions of phonons with  $\omega_m = 15 \text{ cm}^{-1}$ . The two-quantum transition and the slight tailing towards higher phonon frequencies, however, are not

---

<sup>3</sup> The model calculations presented in Chapter 2.4 do also represent the  $\Gamma < \Gamma_{inh}$  regime (see

observed in the pseudo-PSB of the dashed spectrum in Frame B. This is most easily understood by separately analyzing contributions b and c to the FLN spectrum (Eq. 20). Recalling that  $P=0, R \geq 1$  and  $R=0, P \geq 1$  define contributions b and c, respectively, and using a delta function for the ZPL of the homogeneously broadened spectrum, it follows easily that they are given by

$$F_b(\omega) = \sum_{R=1}^{\infty} \left( S^R \frac{e^{-2S}}{R!} \right) N(\omega_E) l_R(\omega - \omega_E + R\omega_m) \quad (22)$$

and

$$F_c(\omega) = \sum_{P=1}^{\infty} \left( S^P \frac{e^{-2S}}{P!} \right) N(\omega) l_P(\omega - \omega_E + P\omega_m). \quad (23)$$

The only difference is that  $F_b(\omega)$  depends on the fixed value of the IDF ( $N$ ) at  $\omega_E$  while  $F_c(\omega)$  depends on  $N(\omega)$ . The latter point is nicely illustrated in frame A of Fig. 39 where it is apparent that the IDF determines the shape of the pseudo-PSB (c) on its low-energy side, i.e. the mirror symmetry between real- and pseudo-PSB breaks down in the  $\Gamma \approx \Gamma_{\text{inh}}$  regime. This effect is directly observed for the pseudo-PSB of the dashed HB spectrum.

### **7.1.2 Calculated Line-Narrowed Spectra**

Returning to the experimental data, 4.2 K FLN and HB spectra obtained for  $\lambda_E$  ( $\lambda_B$ ) within the low-energy wing of the lowest energy  $Q_y$ -state of the trimeric LHC II complex are shown in Fig. 40. The noisy curve in Frame C is a HB spectrum obtained with  $\lambda_B = 681.0$  nm (see Chapter 4.1.4). The real- and pseudo-PSBH at  $+24$  and  $-18$   $\text{cm}^{-1}$  relative to the ZPH are indicated by broken and full arrows, respectively. The noisy curve in Frame B is a FLN spectrum obtained with  $\lambda_E = 680.5$  nm (see Chapter 4.6.4). The ZPL at 680.5 nm was obscured by scattered laser light and, therefore, subtracted from the experimental spectrum by the procedure given in Chapter 4.6.1. Thus, the noisy spectrum represents the PSB structure. Its comparison with either the real- or pseudo-PSBH in Frame C might suggest incompatibility since the width test

---

parameters given in Table 1) so that basic conclusions are directly comparable.

of the PSB appears to be much broader than the apparent widths of the PSBH.

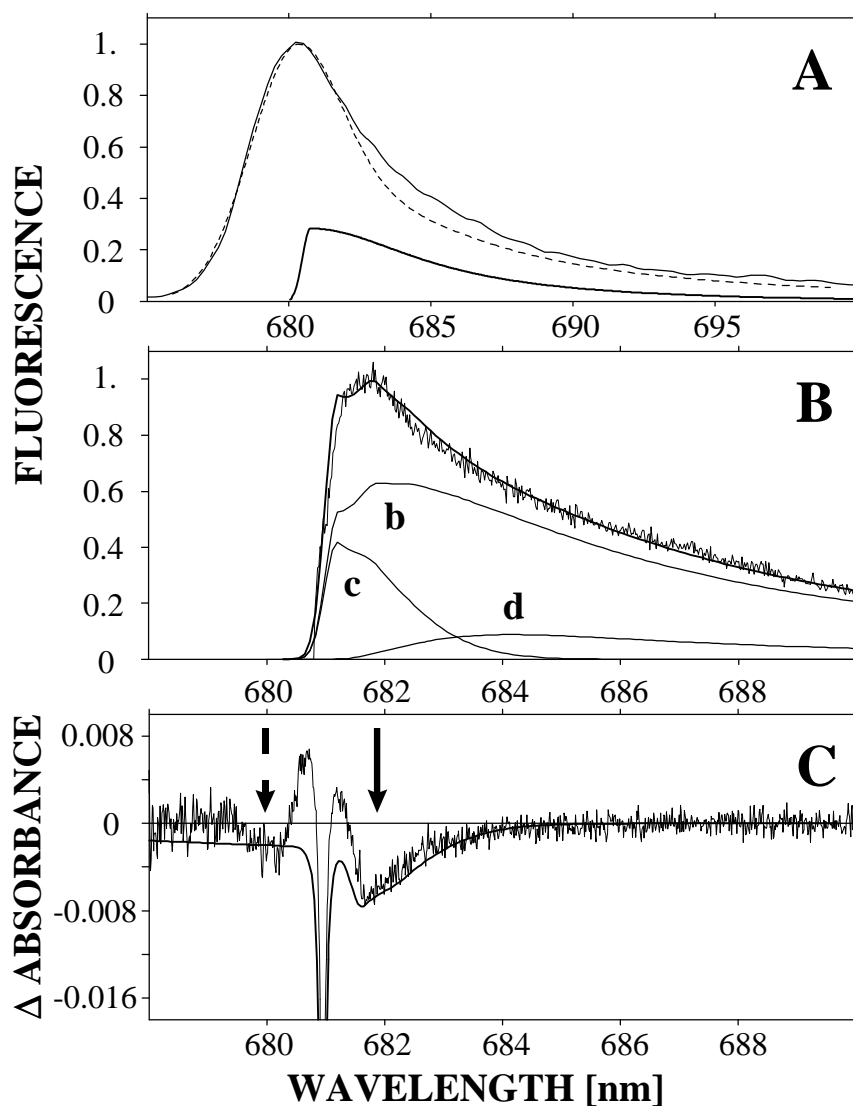


Figure 40. Analysis of phonon structure in HB, FLN and non-line-narrowed fluorescence spectra of trimeric LHC II at 4.2 K. Parameters are given in Table 4. Frame A: Experimental (full line) and calculated (dashed line) non-line-narrowed fluorescence spectra, respectively. The one-phonon profile (profile a) is shown as a full line on the bottom. Frame B: Experimental FLN spectrum (noisy line) obtained with  $I_E = 680.5$  nm. The scattered laser light has been subtracted. The fit was calculated according to Eq. 20 (smooth line). Contributions (b)-(d) are labeled as in Figs. 38 and 39. Frame C: Experimental HB spectrum (noisy line) from Fig. 23 obtained with  $I_B = 681.0$  nm and a burn fluence of  $15 \text{ J/cm}^2$ . The real- and pseudo-PSBH are indicated by full and broken arrows, respectively. The fit was calculated according to Eq. 18 with  $g = 0.2 \text{ cm}^{-1}$  and  $sIFt = 0.003$  (smooth line). See Fig. 42 for the complete fit.

Table 4 Comparison of the parameters obtained by HB, FLN, and the simultaneous fit shown in Fig. 40.

		HB	FLN	fit
temperature	T [K]	4.2		
position of lowest state	$\lambda_c$ [nm]	679.8±0.2	~ 680	680
homogeneous width	$\gamma$ [cm <sup>-1</sup> ]	0.073	-	*
inhomogeneous width	$\Gamma_{inh}$ [cm <sup>-1</sup> ]	80±10	~ 80	80
Huang-Rhys factor	S	0.8-0.9	-	0.9
peak phonon frequency	$\omega_m$ [cm <sup>-1</sup> ]	18	22	15
FWHM of Gaussian wing	$\Gamma_G$ [cm <sup>-1</sup> ]	-	-	10
FWHM of Lorentzian wing	$\Gamma_L$ [cm <sup>-1</sup> ]	-	-	200
FWHM, one-phonon profile	$\Gamma$ [cm <sup>-1</sup> ]	~ 25	~ 100	105

\* the fit procedure used (see Chapter 2.4.5) requires that  $\gamma \ll \Gamma_{inh}$

Nevertheless, the 4.2 K FLN and HB spectra of Fig. 40 can be fit simultaneously using the following approach: The given values for the position of the lowest Q<sub>y</sub>-state  $\lambda_c$  at (679.8±0.2) nm and the inhomogeneous width  $\Gamma_{inh}$  of (80±10) cm<sup>-1</sup> were varied within the range of the experimental uncertainty. The Huang-Rhys factor S of 0.9 was determined from the saturated hole depth of the ZPH at 681.0 nm (see Chapter 4.1.4), i.e. its value does not depend on the shape (and relative intensities) of the phonon sideband hole(s). Furthermore, it was discussed in Chapter 6.2 that for  $g = 0.073$  cm<sup>-1</sup> (see Chapter 4.1.2) and a read resolution of 0.3 cm<sup>-1</sup> the ZPH width of shallow holes is approximately given by  $G_{hole} = 2g + 0.3$  cm<sup>-1</sup>. Since a finite laser linewidth and/or spectral resolution is not accounted for in Eq. 18, the homogeneous width  $g$  was set to 0.2 cm<sup>-1</sup> to reproduce the width of the experimental ZPH. Guided by the pronounced asymmetry of the FLN spectra the one-phonon profile was

assumed to be asymmetric with free parameters  $\omega_m$ ,  $\Gamma_G$  and  $\Gamma_L$ . The latter three values were varied so as to give the best overall fit to the HB and FLN spectra of Fig. 40 under the condition that the depth of the experimental ZPH could be reproduced. Because of the interference of the anti-hole with the real-PSBH, the fit to the HB spectrum was based on the ZPH and pseudo-PSBH. In particular, the depth of the calculated ZPH was normalized to 125 % of the experimentally obtained hole depth in order to account for the interference of the anti-hole with the ZPH.

Based on these assumptions, the calculated spectra in Frames B and C of Fig. 40 were obtained according to Eqs. 20 and 17, respectively, for the parameter set compiled in Table 4, i.e.  $\omega_C = 14705 \text{ cm}^{-1}$  (680.0 nm),  $\omega_E = 14695.1 \text{ cm}^{-1}$  (680.5 nm),  $\omega_B = 14684.3 \text{ cm}^{-1}$  (681.0 nm),  $\Gamma_{inh} = 80 \text{ cm}^{-1}$ , and  $S=0.9$ . To achieve reasonable agreement between the fit and the experimental data,  $\omega_m$  had to be reduced from  $18 \text{ cm}^{-1}$ , as reported in Chapter 4.1.4, to  $15 \text{ cm}^{-1}$ . Thus, the one-phonon profile is characterized by  $\omega_m = 15 \text{ cm}^{-1}$  and  $\Gamma = 105 \text{ cm}^{-1}$  ( $\Gamma_G = 10 \text{ cm}^{-1}$ ,  $\Gamma_L = 200 \text{ cm}^{-1}$ ). It is shown as a full line on the bottom of Frame A in Fig. 40. The contributions b, c and d to the calculated fluorescence spectrum are shown in Frame B. What is striking is that the PSB in the FLN spectrum and the pseudo-PSBH in the HB spectrum, which from cursory examination give different qualitative pictures of electron-phonon coupling, can be explained with the same set of parameter values. It is obvious that the shape of contribution c to the FLN spectrum closely resembles that of the pseudo-PSBH of the HB spectrum while the pronounced asymmetry of the FLN spectrum is mainly due to contribution b (real-PSB). A similar scenario was observed when discussing model calculations for the  $\Gamma \approx \Gamma_{inh}$  regime (see Fig. 39 in the previous chapter). Thus, it can be concluded that the mirror symmetry between the real- and pseudo-PSB in HB and FLN spectra of LHC II breaks down because the width of the one-phonon profile is of the same magnitude as the inhomogeneous width. As a consequence, the low-energy wing of the pseudo-PSB in HB spectra is determined by the IDF rather than by the one-phonon profile. This finding readily explains the discrepancies in the shapes of the line-narrowed spectra of LHC II.

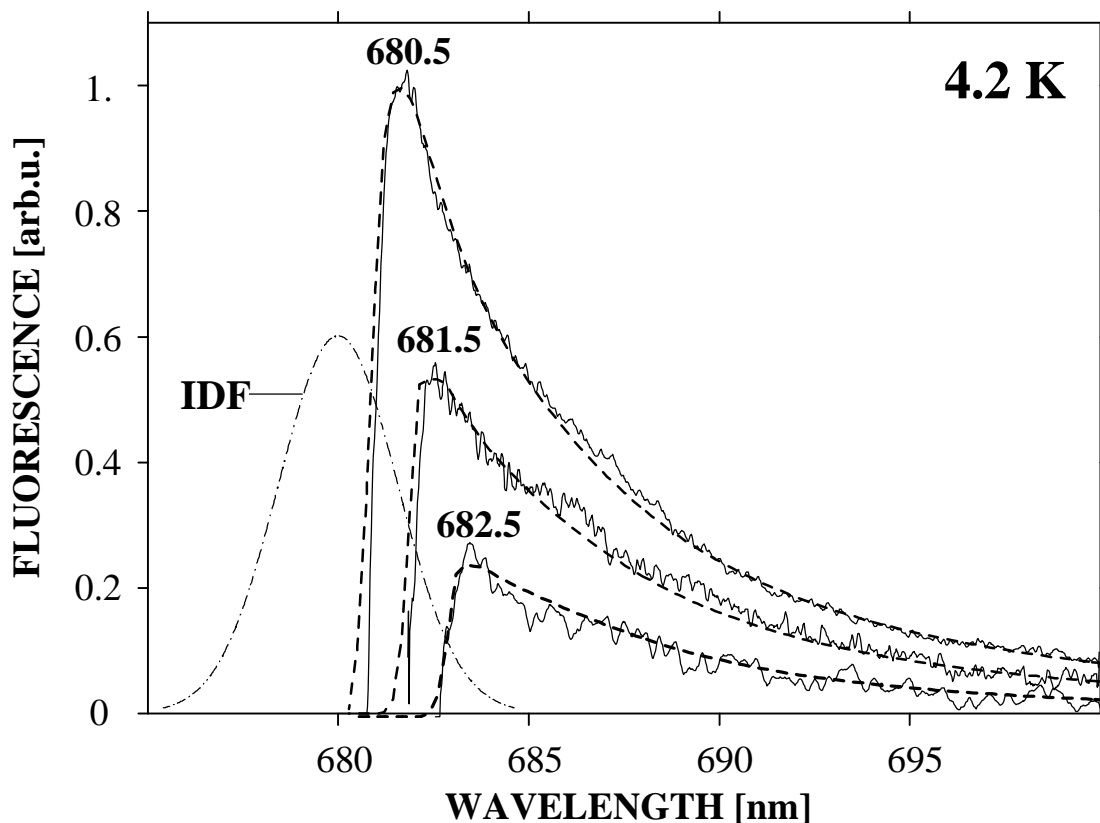


Figure 41. Experimental FLN spectra of LHC II at 4.2 K (full, noisy lines) generated with excitation wavelengths of 680.5, 681.5, and 682.5 nm from left to right, respectively. Scattered laser light has been subtracted from the FLN spectra. Calculated spectra (dashed lines) were obtained according to Eq. 20 for the parameters given in Table 4. The IDF profile (dashed-dotted line) is shown for comparison.

As a next step, it was verified that the parameters used above do also account for the excitation wavelength dependence of the FLN spectra. The full lines in Fig. 41 show FLN spectra obtained at 4.2 K with  $\lambda_E = 680.5$ , 681.5 and, 682.5 nm. The ZPL were subtracted as described in Chapter 4.6.1 so that the spectra represent the PSB structure. The dashed lines were calculated according to Eq. 20 for the parameters of Table 4. In general, the fits are in good agreement with the experimental data. At the first glance the value of  $\omega_m = 15 \text{ cm}^{-1}$  seems to be surprisingly low compared to the peak frequency of the measured FLN spectra. For the relatively high S-value of 0.9, however, higher phonon transitions ( $R > 1$ ) contribute significantly to the entire phonon wing. Thus, the observed peak of the FLN spectra at  $24 \text{ cm}^{-1}$  results mainly from the superposition of the one- and the two-phonon transitions at  $15 \text{ cm}^{-1}$  and  $30 \text{ cm}^{-1}$ , respectively. Therefore, the fit is very sensitive to the position of  $\omega_m$ . The width ( $\Gamma = 105 \text{ cm}^{-1}$ ) and, especially, the strong asymmetry

( $\Gamma_L = 200 \text{ cm}^{-1}$ ) of the one-phonon profile are essential to account for the shape of the FLN spectra.

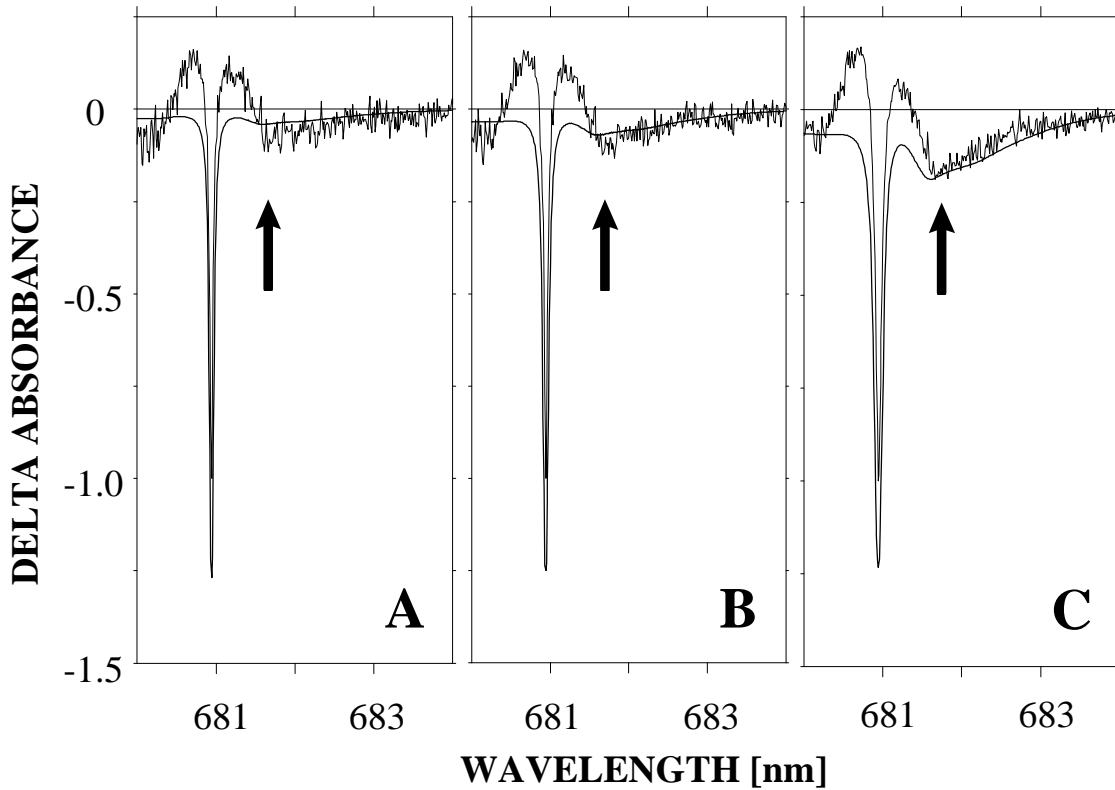


Figure 42. Experimental, normalized HB spectra of LHC II at 4.2 K (noisy lines) generated with  $I_B = 681 \text{ nm}$  and burn fluences of 1.5 (A), 3.0 (B), and  $15.0 \text{ J/cm}^2$  (C), respectively. The pseudo-PSBH are indicated by arrows. Calculated spectra (smooth lines) were obtained according to Eq. 18 for the parameters given in Table 4,  $g = 0.2 \text{ cm}^{-1}$  and  $sIFt$ -values of 0.0003 (A), 0.0006 (B), and 0.0030 (C), respectively. The depths of the calculated ZPH were normalized to 125 % of the actual hole depths to account for the anti-hole (see positive DA at both sides of the ZPH).

While the excitation wavelength dependence of the FLN spectra is especially sensible to the shape of the one-phonon profile, the value of S used above can be verified studying the burn fluence dependence of the HB spectrum, i.e. the burn fluence dependence of the relative ZPH and pseudo-PSBH intensities. In contrast to the FLN spectra, these features are directly observed in NPHB. The noisy lines in Fig. 42 show normalized HB spectra of LHC II generated at 4.2 K with  $I_B = 681 \text{ nm}$  and burn fluences of 1.5 (A), 3.0 (B), and  $15.0 \text{ J/cm}^2$  (C), respectively. The pseudo-PSBH are indicated by arrows. Calculated spectra (smooth lines) were obtained according to Eq. 18 for the parameters given in Table 4,  $g = 0.2 \text{ cm}^{-1}$  and  $sIFt$ -values of 0.0005 (A), 0.0010 (B), and 0.0050 (C), respectively. The depths of the calculated ZPH were normalized to

125 % of the actual hole depths to account for the interference of the ZPH with the anti-hole (see positive *DA* at both sides of the ZPH). It is apparent from Fig. 42 that the fit accounts for the broadening of the ZPH as well as for the increase in pseudo-PSBH intensity with increasing burn fluence. Thus, the burn fluence dependence of the HB spectrum provides further support for the electron-phonon coupling parameters used above (see Table 4) and, especially, for a Huang-Rhys factor *S* of 0.9.

As a final verification, the 4.2 K non-line-narrowed fluorescence spectrum of LHC II was calculated according to Eq. 11 for the values of Table 4 and shown as the dashed line in Frame A of Fig. 40. In general, the agreement with the experimental data (see full line) is quite satisfactory compared to previous studies (Peterman et al., 1997; Pieper et al., 1997). Obviously, the fit accounts for the peak position and the width of the fluorescence origin band as well as for its pronounced asymmetry and, therefore, confirms the electron-phonon coupling parameters determined by the fit of the line-narrowed spectra, *vide supra*. Moreover, the assignment of the lowest  $Q_y$ -state and its inhomogeneous broadening (see Chapter 5) can be verified. Slight deviations at the low-energy wing may have several reasons. First, the arbitrarily chosen Gaussian/Lorentzian shape may not exactly describe the actual one-phonon profile. Especially, the FLN spectrum calculated for an excitation wavelength of 682.5 nm, i.e. the spectrum with highest selectivity, appears to be too broad in the peak region, while it does not fully account for the weak shoulder at  $\sim 90 \text{ cm}^{-1}$  (*vide infra*). Another possibility is that minor protein complexes present in the sample provide weak emission near 684 nm (Vasil'ev et al., 1997a). Finally, vibrational satellites resulting from low-frequency intramolecular Chl modes ( $>250 \text{ cm}^{-1}$ ) may contribute to the fluorescence in this spectral region.

### **7.1.3 The One-Phonon Profile**

Summarizing the results of the preceding chapter, the 4.2 K FLN, HB and non-line-narrowed fluorescence data of trimeric LHC II can be simultaneously described by weak electron-phonon coupling with a Huang-Rhys factor *S* of 0.9 to a broad and strongly asymmetric one-phonon profile with a peak frequency

$\omega_m$  of  $15 \text{ cm}^{-1}$  and a width of  $\Gamma = 105 \text{ cm}^{-1}$ . Weak coupling strengths ( $S < 1$ ) and one-phonon profiles peaking at  $\sim 20 \text{ cm}^{-1}$  are generally reported for photosynthetic antenna complexes (for a review see e.g. Hayes et al., 1988a; Reddy et al., 1992). A one-phonon profile having a width of  $105 \text{ cm}^{-1}$ , however, has been reported for the first time and cannot be understood in terms of a mean phonon frequency<sup>4</sup>. The profile rather represents a broad distribution of phonon modes which are most likely attributed to delocalized vibrations of the amorphous protein backbone (see e.g. Hayes et al., 1988b). Then, the one-phonon profile basically reflects the density of states of the protein phonons multiplied by a frequency-dependent coupling strength. It is well-established that intramolecular vibrations of Chl *a* appear in the frequency range of  $> 250 \text{ cm}^{-1}$  (Avarmaa and Rebane, 1985; Gillie et al., 1989, Peterman et al., 1997) with *S* factors lower than 0.04 (Gillie et al., 1989). However, it is possible that certain pseudo-localized or localized vibrations of the protein as well as intermolecular (Chl-Chl) vibrations contribute to the high-energy wing of the one-phonon profile ( $> 50 \text{ cm}^{-1}$ ). The best example for such a mode is probably the *marker* mode ( $115 \text{ cm}^{-1} - 135 \text{ cm}^{-1}$ ) observed for bacterial reaction centers which was assigned to an intermolecular vibration of the special pair (Johnson and Small, 1989). Similar interpretations were suggested as one possibility to understand features at  $\sim 80 \text{ cm}^{-1}$  in the FLN spectra of the PS II reaction center (Peterman et al., 1998) and the CP47 core antenna complex (den Hartog et al., 1998). In this regard, it is interesting to note that a weak shoulder is observed at  $\sim 90 \text{ cm}^{-1}$  in the FLN spectra of LHC II, which is not fully accounted for in the one-phonon profile used in the above simulations. As for all modes constituting the high-frequency tail of the one-phonon profile, it cannot be distinguished, however, whether this shoulder represents a phonon mode of the protein, a pseudo-localized or intermolecular vibration.

---

<sup>4</sup> Nevertheless, the mean phonon frequency approximation is valid for theoretical calculations within the low-temperature limit, i.e. for negligible thermal population of phonon states, regardless of the actual width of the one-phonon profile. In this case, all frequency-dependent parameters can be expressed by the one-phonon profile.

## **7.2 Temperature-Dependent Spectra**

At temperatures higher than 4.2 K thermal occupation of both, higher electronic states and phonon modes, has to be accounted for. Both effects are qualitatively observed in the fluorescence spectra shown in Fig. 43. The blue-shift of the fluorescence peak for temperatures between 4.2 K to 120 K suggests that higher electronic states are subsequently populated with increasing temperature. Moreover, the onset of the blue-shift at a temperature as low as 30 K ( $kT \sim 21 \text{ cm}^{-1}$ ) points to a very small energetic difference between the adjacent state(s). The more symmetric shape of fluorescence origin band at temperatures  $\geq 60$  K can at least partly be attributed to thermal occupation of phonon modes giving rise to the anti-Stokes part of the PSB.

The simulations presented in Fig. 43 were based on the low-energy  $Q_y$ -level structure and corresponding oscillator strengths determined in HB experiments (see Chapter 5), i.e. the lowest  $Q_y$ -state at  $\sim 680.0$  nm is accompanied by two higher states at 678.4 and 677.1 nm, respectively. These three states are assumed to be associated with the three subunits of the LHC II trimer. The energetic separations of  $\sim 30 \text{ cm}^{-1}$  are most likely due to structural heterogeneity. Each of the three states was reported to carry the absorption intensity of approximately one Chl *a* molecule per LHC II trimer. Then, the absorption intensity of the next higher  $Q_y$ -state at  $\sim 676.0$  nm was estimated to be equal to that of six Chl *a* molecules per LHC II trimer. In the following it will be assumed that rapid thermal equilibration of excitation energy occurs among the  $\sim 680.0$ , 678.4, 677.1, and  $\sim 676.0$  nm states. Consideration of only these four  $Q_y$ -states appears to be justified because  $kT \sim 83 \text{ cm}^{-1}$  at 120 K, which is almost equal to the energetic difference between the 680 and the 676 nm-state. Thus, the 676 nm-state is the highest significantly populated  $Q_y$ -level at 120 K. To reduce the number of parameters it will be assumed that all four states are characterized by an inhomogeneous width of  $80 \text{ cm}^{-1}$  and the electron-phonon coupling parameters of the lowest state determined in the preceding chapter (see Table 4). The spectral positions, widths and oscillator strengths of the above four states are summarized in Table 6.

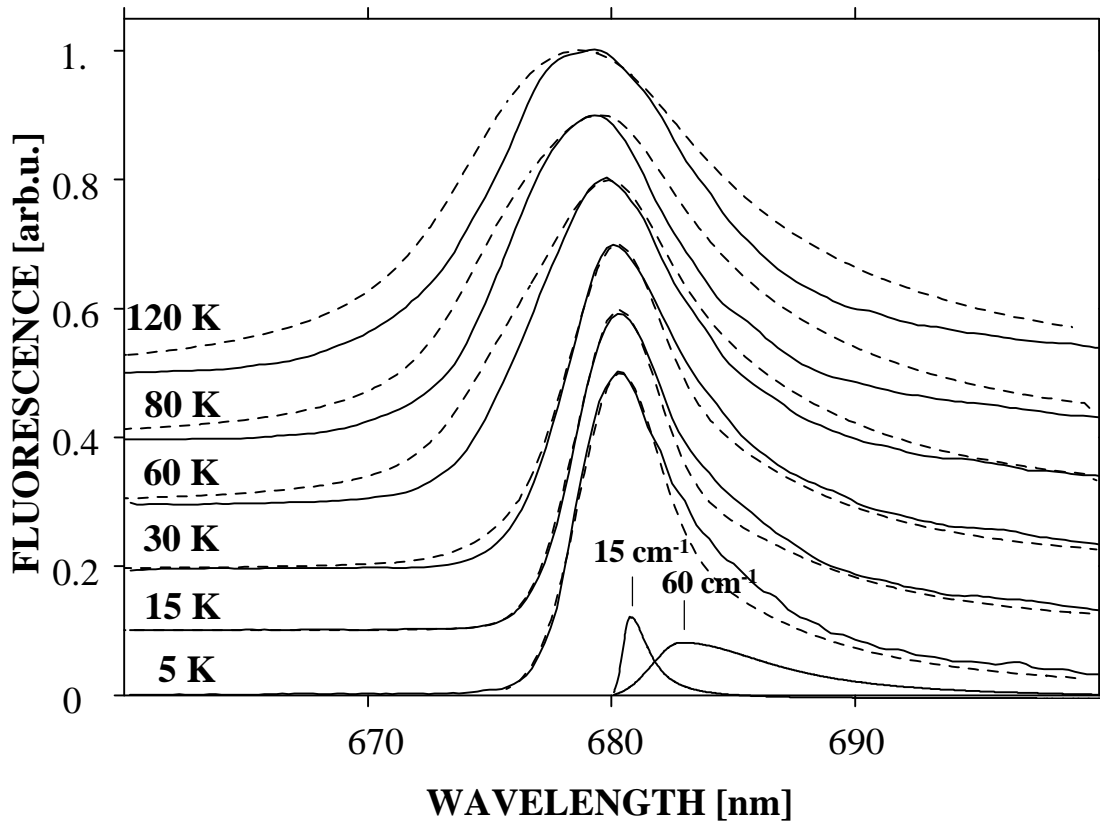


Figure 43. Normalized experimental (full lines) and calculated (dashed lines) fluorescence spectra of LHC II at different temperatures. The spectra were given equidistant offsets for ease of inspection. The calculated spectra were obtained for the parameters of Table 5 and the low-energy level structure of Table 6. The one-phonon profiles *b* and *c* are shown at the bottom and labeled by their peak frequencies of  $15 \text{ cm}^{-1}$  and  $60 \text{ cm}^{-1}$ , respectively.

Eq. 15 is used to simulate the temperature-dependent fluorescence band of each state. In the temperature range between 4.2 and 120 K  $kT$  increases from  $3.5$  to  $83 \text{ cm}^{-1}$ , while the one-phonon profile has a width of  $105 \text{ cm}^{-1}$  (see profile *a* in Table 5 and bottom of Frame A in Fig. 40). In order to partly account for the varying thermal occupation of the modes constituting the one-phonon profile, the latter was arbitrarily divided into two profiles (see bottom of Fig. 43) with maxima at  $15$  and  $60 \text{ cm}^{-1}$  (see profiles *b* and *c* in Table 5), respectively. Summation over the latter two profiles yields profile *a* (not shown). The separate profile peaking at  $60 \text{ cm}^{-1}$  has no special physical meaning but appeared to be a good intermediate value between  $kT$  at 4.2 and 120 K, respectively. The 4.2 K fluorescence spectrum calculated for the double profile (see Fig. 43) resembles exactly that shown in Frame A of Fig. 40.

Table 5 Parameters of the one-phonon profiles used to fit experimental data obtained at 4.2 K (profile a, see Fig. 40) and at higher temperatures (profiles b and c, see Fig. 43). The sum of profiles b and c equals profile a.

		profile a	profile b	profile c
temperature	T [K]	4.2	> 4.2	
lowest state(s)		see Table 6		
Huang-Rhys factor	S	0.9	0.22	0.68
peak phonon frequency	$\omega_m$ [ $\text{cm}^{-1}$ ]	15	15	60
FWHM of Gaussian wing	$\Gamma_G$ [ $\text{cm}^{-1}$ ]	10	10	60
FWHM of Lorentzian wing	$\Gamma_L$ [ $\text{cm}^{-1}$ ]	200	40	200
FWHM, one-phonon profile	$\Gamma$ [ $\text{cm}^{-1}$ ]	105	25	130

Table 6 Parameters of the low-energy  $Q_y$ -states of trimeric LHC II used to obtain the fits of Fig. 43.

$Q_y$ -state		adjacent $Q_y$ -state	lowest-energy $Q_y$ -states of the trimer subunits		
position	$\lambda_c$ [nm]	~ 676.0	677.1	678.4	680.0
homogeneous width	$\gamma$ [ $\text{cm}^{-1}$ ]	*			
inhomogeneous width	$\Gamma_{inh}$ [ $\text{cm}^{-1}$ ]	~80	80	80	80
absorption intensity per LHC II trimer	Chl a	6	1	1	1

\* the fit procedure used (see Chapter 2.4.5) requires that  $\gamma \ll \Gamma_{inh}$

Based on the parameters of Table 5, the fluorescence spectrum of each of the four states, *vide supra*, was calculated for a given temperature according to Eq. 15 and then multiplied by its individual oscillator strength (see Table 6) and

thermal population according to the Boltzmann distribution. After summation of the fluorescence bands of the four states the spectrum is finally normalized to be compared to the experimental data. It has to be noted that no adjustable parameters enter into the calculations. Fig. 43 shows the experimental non-line-narrowed (full lines) and calculated fluorescence spectra (dashed lines) for temperatures between 4.2 K and 120 K. The calculated spectra show the basic features of the temperature-dependent fluorescence spectra such as thermal broadening, more symmetric shape and blue-shifting of the fluorescence peak with increasing temperature. Especially, the blue-shift of the maximum is in almost perfect agreement with the experimental data. For temperatures  $\geq 60$  K, however, the spectra appear to be too broad. There are two possible reasons for this effect. First, the oscillator strength of the 676 nm-state might be slightly overestimated. Second, the arbitrarily divided one-phonon profile represents, strictly speaking, a two phonon frequency approximation, only. While the thermal population is exactly calculated for the mean frequency of each of the two profiles, phonon modes of lower/ higher frequency within the profile experience a population that is too low/ too high at a given temperature. This inaccuracy is more critical for the profile peaking at  $60\text{ cm}^{-1}$  because of its width of more than  $100\text{ cm}^{-1}$ . Consequently, the calculated spectra with this mode being significantly populated ( $\geq 60$  K) appear to be too broad. Nevertheless, it can be concluded that the temperature-dependent fluorescence spectra of LHC II can be satisfactorily described between 4.2 and 120 K based on the  $Q_y$ -level structure of Chapter 5 as well as the electron-phonon coupling parameters determined in Chapter 7.1.

### ***7.3 Effects at Temperatures above 120 K***

The temperature dependence of the LHC II fluorescence spectrum undergoes a drastic change above 120 K. A further blue-shifting would be expected with increasing temperature and subsequent population of higher  $Q_y$ -states. In contrast to this, a red-shift of the fluorescence peak is observed between  $\sim 150$  K and room temperature, which is not in line with the model presented above. A similar phenomenon was reported, for example, for the B875 absorption band of the LH1 antenna complex of *Rhodobacter sphaeroides*

(Wu et al., 1998). Briefly, its energetic location was found to be invariant, within experimental uncertainty, below  $\sim 150$  K, but shifting linearly to the blue at higher temperatures. In addition different rates of thermal broadening were observed above and below  $\sim 150$  K, respectively. Because these changes set in close to the glass temperature ( $T_g$ ), it was suggested that conformational changes of the protein environment become possible due to a decrease in viscosity above  $T_g$  (see Wu et al., 1998 and Refs. therein). Such structural changes may alter pigment-protein interactions as well as excitonic interactions between different Chls. The latter effect was found to be more important for the B850 and B875 bands by Wu et al. (1998). In the case of LHC II, theoretical calculations within the density matrix formalism (T. Renger et al., 1995, 1996) revealed that excitonic interactions between Chl molecules have a small effect on the  $Q_y$ -energies but may result in a remarkable redistribution of oscillator strengths. A redistribution of absorption intensity with increasing temperature, i.e. a gain of oscillator strength of the low-energy  $Q_y$ -states, has already been proposed from a study of the temperature dependence of the LHC II absorption spectrum (Voigt and Schrötter, 1999) and would also qualitatively account for the red-shift of the fluorescence peak above  $\sim 150$  K observed in the present study. In addition, complicating factors such as increasing heterogeneity due to thermally accessible conformational substates as well as quadratic and/ or anharmonic electron-phonon coupling can be expected at higher temperatures (see e.g. Hayes et al., 1994 and Refs. therein).

Another interesting effect, however, can be observed at the high-energy wing of the LHC II fluorescence spectra. Fig. 44 shows the half-logarithmic plot of the normalized fluorescence signal (650-680 nm) versus a wavenumber scale. Surprisingly, linear ranges over at least  $200 \text{ cm}^{-1}$  appear for all temperatures between 80 and 290 K. This observation suggests that the high-energy wing of the LHC II fluorescence spectrum is characterized by an exponential law. If the slope is identified with  $kT/h\nu$  the linear regression yields approximately the sample temperature (see caption of Fig. 44). This is remarkable since emission of a given fluorescent state should be proportional to the product of oscillator strength and thermal population. Nevertheless, this result indicates that higher energy  $Q_y$ -states are populated according to a Boltzmann

distribution representing the thermal equilibrium of the excitation energy at temperatures above 80 K. This is in line with conclusions from pump-probe experiments at room temperature (Schrötter et al., 1994).

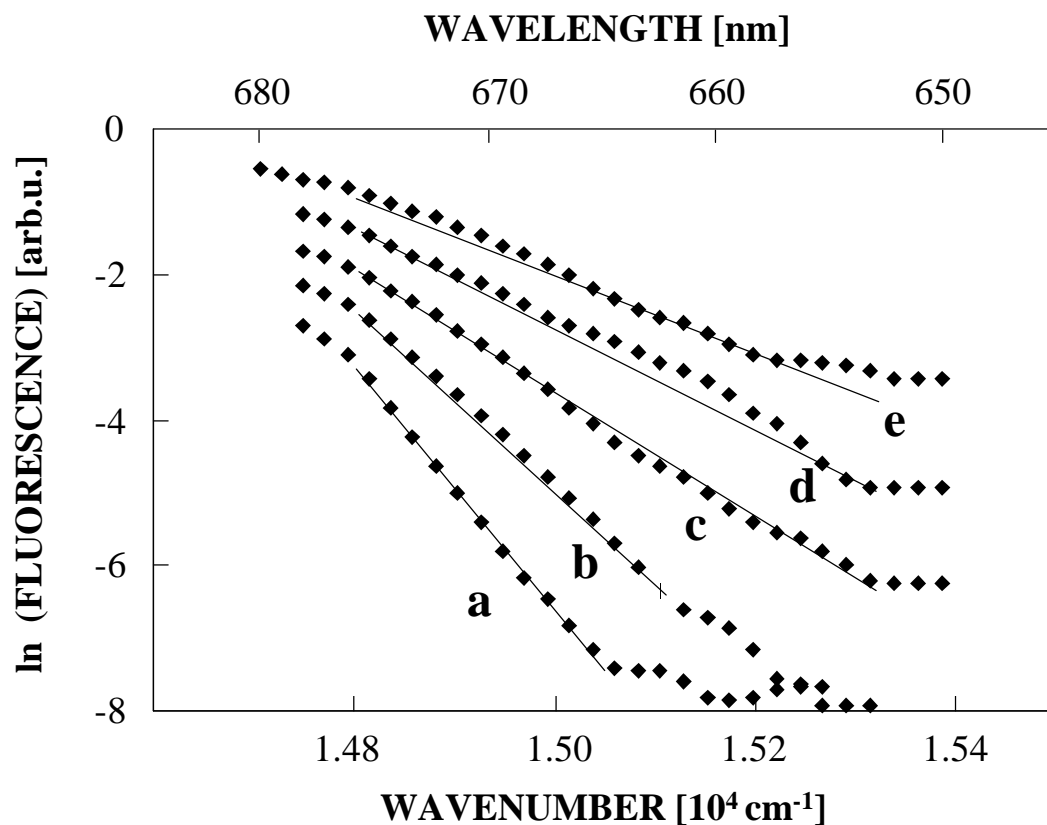


Figure 44. Natural logarithm of normalized fluorescence spectra of LHC II (high-energy wing) and its linear fit for temperatures of a) 80 K ( $85 \pm 2$ ), b) 120 K ( $115 \pm 2$ ), c) 180 K ( $169 \pm 2$ ), d) 240 K ( $215 \pm 5$ ), and e) 300 K ( $278 \pm 7$ ). Temperatures in brackets were calculated from linear regression.

## **8 Concluding Remarks**

### **8.1 Low-Energy Level Structure of LHC II**

Detailed nonphotochemical hole-burning at 4.2 K and pressure-dependent experiments were used to *identify and characterize the low-energy  $Q_y$ -levels* of the trimeric LHC II antenna complex of green plants. Comparative studies were carried out for aggregated LHC II as well as for the CP29 antenna complex of green plants.

For the first time, analysis of the 4.2 K burn-fluence-dependent hole spectra and ZPH action spectra has revealed the presence of three lowest energy  $Q_y$ -states, which are located at  $(677.1 \pm 0.2)$ ,  $(678.4 \pm 0.2)$  and  $(679.8 \pm 0.2)$  nm. The inhomogeneous width of their absorption bands is  $(80 \pm 10)$   $\text{cm}^{-1}$ . Their combined absorption intensity is equivalent to that of three Chl *a* molecules per LHC II trimer. Therefore, it is likely that these states are associated with the lowest energy state of each trimer subunit and each state is highly localized on one Chl *a* molecule of the respective subunit. For intersubunit coupling strength of  $\sim 5$   $\text{cm}^{-1}$  (Voigt et al., 1996), the energetic separations of  $\sim 30$   $\text{cm}^{-1}$  are most likely attributed to structural heterogeneity among the three subunits. This interpretation is consistent with the results obtained for the structurally similar but less complex, monomeric CP29 antenna system of green plants. Only one low-energy state at  $\sim 678.4$  nm was assigned for the latter monomeric complex. Furthermore, the above burn fluence dependence of the low-energy hole features was not observed.

Comparative studies on aggregated LHC II establish that non-desirable aggregation of LHC II samples may lead to a red-shift of the low-energy states of up to 2 nm and appearance of additional absorption at  $\sim 683$  nm. In agreement with the results of Vasil'ev et al. (1997b) it can be concluded, however, that the results reported above are virtually free from effects owing to aggregation of LHC II.

The satellite hole structure produced by hole-burning in the above three low-energy states of trimeric LHC II is relatively weak. The linear pressure shift rates of the corresponding ZPH are as low as  $-0.08$   $\text{cm}^{-1}/\text{MPa}$ , i.e. they are

comparable to those reported for isolated chromophores in amorphous hosts (see e.g. Reddy et al., 1996). The weak satellite hole structure as well as the low pressure shift rates indicate that each of the low-energy states is highly localized on a single Chl *a* molecule of the corresponding trimer subunit which is weakly coupled to other Chl molecules.

The linear pressure shift rates for the main  $Q_y$ -absorption bands are of the same magnitude. Thus, the shift rates appear to be dictated by protein-Chl interactions rather than excitonic couplings. Weak satellite holes associated with the 650 and 671 nm bands as well as the differences in their pressure shift rates may be related to excitonic coupling within Chl *b/a*-dimers as reported by T. Renger et al. (1995, 1996) on the basis of the structural model by Kühlbrandt et al. (1994).

## **8.2 Excitation Energy Transfer in LHC II**

The temperature dependence of the zero-phonon hole width for the lowest state at 679.8 nm indicates that its optical dynamics is dominated by pure dephasing due to coupling with glass-like TLS of the protein for  $T \gtrsim 10$  K. The homogeneous width at 4.7 K is  $0.073 \text{ cm}^{-1}$  corresponding to a pure dephasing time of 150 ps. The absence of EET from the 679.8 nm-state provides further support for its assignment as lowest  $Q_y$ -state of trimeric LHC II.

Holes burned into the 650 nm absorption band reveal lifetimes of 1 ps and  $\sim 240$  fs at 4.2 K, which are similar to the results of time domain measurements of the time constants for Chl *b*  $\rightarrow$  Chl *a* EET (Bittner et al., 1995). The holewidths of ZPH burned into the 676 nm absorption band lead to time constants for Chl *a*  $\rightarrow$  Chl *a* EET in the 6-10 ps range, in good agreement with the time domain values (Savikhin et al., 1994).

## **8.3 Electron-Phonon Coupling in LHC II**

Spectral hole-burning was combined with fluorescence line-narrowing experiments at 4.2 K and investigations of the temperature dependence of non-line-narrowed fluorescence spectra in order to investigate the *electron-phonon coupling of the lowest energy state of LHC II*. Special attention has been paid to eliminate effects owing to reabsorption and to assure that the line-narrowed

fluorescence spectra are virtually unaffected by hole-burning or scattering artifacts.

The PSB structures observed in FLN and HB spectra associated with the lowest  $Q_y$ -state of LHC II exhibit apparent differences in shape and peak position. HB revealed a pseudo-PSBH hole peaking at  $\sim 18 \text{ cm}^{-1}$  and having a width of only  $\sim 25 \text{ cm}^{-1}$  while complementary fluorescence line-narrowing experiments yielded much broader sidebands peaking at  $\sim 24 \text{ cm}^{-1}$  and having a width of  $\sim 100 \text{ cm}^{-1}$ . Therefore, the complexities associated with interpretation of the phonon structure in FLN and HB spectra were discussed by theoretically analyzing the different (PSB) contributions. It was shown that the mirror symmetry between the real- and pseudo-PSB breaks down in the  $\Gamma \sim \Gamma_{\text{inh}}$  regime where  $\Gamma$  is the width of the one-phonon profile and  $\Gamma_{\text{inh}}$  is the inhomogeneous width of the absorption band. In this case, the shape of the pseudo-PSB is determined by the IDF rather than by the one-phonon profile. This effect may explain the discrepancy between the HB and FLN results for the LHC II complex. Furthermore, it is concluded that the combination of HB and FLN is the most reliable approach for determining the shape of the one-phonon profile.

The simultaneous analysis of the 4.2 K fluorescence line-narrowing and hole-burning data indicates that the lowest  $Q_y$ -state of LHC II is characterized by weak electron-phonon coupling with a Huang-Rhys factor of  $\sim 0.9$  to a broad and strongly asymmetric one-phonon profile with a peak frequency  $\omega_m$  of  $15 \text{ cm}^{-1}$  and a width of  $\Gamma = 105 \text{ cm}^{-1}$ . At the same time a fit of the 4.2 K non-line-narrowed fluorescence spectrum confirmed the latter parameters of electron-phonon coupling as well as the assignment of the lowest  $Q_y$ -state at  $\sim 680.0 \text{ nm}$  and its inhomogeneous width of  $\sim 80 \text{ cm}^{-1}$ .

A one-phonon profile having a width of  $\sim 100 \text{ cm}^{-1}$  has been reported for the first time and cannot be understood in terms of a mean phonon frequency but rather represents a broad distribution of modes. The modes constituting the one-phonon profile are most likely attributed to delocalized vibrations of the amorphous protein backbone (see e.g. Hayes et al., 1988a). Then, the one-phonon profile basically reflects the density of states of the protein phonons

multiplied by a frequency-dependent coupling strength. It is possible, however, that pseudo-localized or localized vibrations of the protein as well as intermolecular (Chl-Chl) vibrations similar to the *marker* mode ( $115\text{ cm}^{-1}$  -  $135\text{ cm}^{-1}$ ) observed for bacterial reaction centers (Johnson and Small, 1989) contribute to the high-energy wing of the one-phonon profile. In this regard, a weak shoulder is observed at  $\sim 90\text{ cm}^{-1}$  in the FLN spectra of LHC II. As for all modes constituting the high-frequency tail of the one-phonon profile it cannot be distinguished, however, whether this shoulder represents a phonon mode of the protein, a pseudo-localized or intermolecular vibration.

The low-energy  $Q_y$ -level structure and corresponding oscillator strengths as well as the parameters of electron-phonon coupling reported above were used to simulate the temperature-dependent fluorescence spectra of LHC II. Up to 120 K the calculations yield the basic features of the temperature-dependent fluorescence spectra such as thermal broadening, varying shape and, especially, the correct blue-shift of the fluorescence peak with increasing temperature. It is argued that conformational changes of the protein environment may be responsible for the red-shift of the fluorescence peak above 150 K. The lineshape of the high-energy wing of the temperature-dependent fluorescence spectra for  $T \gtrsim 80\text{ K}$  indicates that the  $Q_y$ -states are populated according to a Boltzmann distribution.

## **9 Zusammenfassung**

### **9.1 Energieniveaustruktur von LHC II**

Die niederenergetische Energieniveaustruktur des trimerischen Antennenkomplexes LHC II grüner Pflanzen wurde in der vorliegenden Arbeit durch Nichtphotochemisches Lochbrennen (Hole-Burning) bei 4.2 K sowie durch Experimente bei hohem Druck untersucht. Vergleichende Studien wurden an aggregiertem LHC II sowie am Antennenkomplex CP29 grüner Pflanzen durchgeführt.

Durch die Auswertung der Abhängigkeit der Lochspektren von Brennintensität bzw. Brennzeit sowie von Action-Spektren konnten erstmalig drei niederenergetische  $Q_y$ -Zustände des LHC II bei  $(677.1 \pm 0.2)$ ,  $(678.4 \pm 0.2)$  und  $(679.8 \pm 0.2)$  nm nachgewiesen werden. Die inhomogene Verbreiterung der zugehörigen Absorptionsbanden beträgt  $(80 \pm 10) \text{ cm}^{-1}$ . Die gesamte Oszillatorstärke der drei obigen Zustände entspricht etwa der von drei Chl *a*-Molekülen pro LHC II-Trimer. Daher ist es wahrscheinlich, daß jeder der drei niederenergetischen Zustände das jeweils tiefste Energieniveau einer Untereinheit des LHC II-Trimers darstellt und weitgehend an jeweils einem Chl *a*-Molekül lokalisiert ist. Die energetische Differenz zwischen den drei Zuständen von je etwa  $30 \text{ cm}^{-1}$  ist bei Wechselwirkungsenergien zwischen Chl-Molekülen verschiedener Untereinheiten des LHC II-Trimers von weniger als  $5 \text{ cm}^{-1}$  (Voigt et al., 1996) nur durch strukturelle Heterogenität zu erklären. Diese Interpretation ist konsistent mit Ergebnissen für den strukturell ähnlichen Antennenkomplex CP29 grüner Pflanzen. Für das letztere, monomerisch vorliegende System wurde nur ein niederenergetischer Zustand bei 678.4 nm gefunden. Weiterhin konnte eine Abhängigkeit der Lochspektren von Brennintensität bzw. Brennzeit in diesem Fall nicht festgestellt werden.

Vergleichende Untersuchungen an aggregiertem LHC II zeigen, daß unerwünschte Aggregation der verwendeten Proben zu einer Rotverschiebung der niederenergetischen Zustände um bis zu 2 nm und zum Auftreten zusätzlicher Absorption im Bereich vom  $\sim 683$  nm führen kann. In Übereinstimmung mit Vasil'ev et al. (1997b) kann jedoch geschlußfolgert

werden, daß die obigen Ergebnisse für trimerischen LHC II frei von Effekten durch Aggregation sind.

Hole-Burning im Spektralbereich der obigen niederenergetischen Zustände von LHC II erzeugt nur wenig ausgeprägte Resonanzen in energetisch höher liegenden Spektralbereichen. Die Hochdruck-Verschiebungsraten von Nullphonon-Löchern, die in die Absorptionsbanden der niederenergetischen Zustände gebrannt wurden, sind mit  $-0.08 \text{ cm}^{-1}/\text{MPa}$  vom Betrag sehr gering und vergleichbar mit denen isolierter Chromophore in amorphen Matrizen (siehe z.B. Reddy et al., 1996). Sowohl die schwache Resonanzstruktur als auch die Ergebnisse der Hochdruckexperimente weisen weiter darauf hin, daß die drei niederenergetischen Zustände in hohem Maße an jeweils einem Chl *a*-Molekül der entsprechenden Untereinheit des LHC II-Trimers lokalisiert sind.

Der Betrag der Hochdruck-Verschiebungsraten der  $Q_y$ -Absorptionsbanden des LHC II bei 650, 671 und 676 nm ist ebenfalls geringer als  $0.1 \text{ cm}^{-1}/\text{MPa}$ , d.h. ihre Größenordnung wird wesentlich durch die Chl-Protein-Wechselwirkung bestimmt. Die schwach ausgeprägten Resonanzen innerhalb der 650- und 671 nm-Absorptionsbanden sowie die Differenzen der Hochdruck-Verschiebungsraten dieser Banden können durch exzitonische Kopplung zwischen den zugehörigen Chl *a*- und Chl *b*-Molekülen erklärt werden, wie sie von T. Renger et al. (1995; 1996) auf der Grundlage des Strukturmodells von Kühlbrandt et al. (1994) gefunden wurde.

## **9.2 Energietransfer in LHC II**

Die Temperaturabhängigkeit der Breite von Nullphonon-Löchern, die im Spektralbereich des energetisch tiefsten Zustandes bei 679.8 nm gebrannt wurden, weist darauf hin, daß dessen homogene Linienbreite bei Temperaturen unter 10 K im Wesentlichen durch phasenerstörende Prozesse infolge einer Kopplung an die heterogene Proteinumgebung (pure dephasing) bestimmt wird. Insbesondere beträgt die homogene Linienbreite bei 4.7 K  $0.073 \text{ cm}^{-1}$ , was einer reinen Phasenerstörungszeit  $T_2'$  von etwa 150 ps entspricht. Dieses Ergebnis bestätigt, daß kein weiterer Energietransfer vom 679.8 nm-Zustand ausgeht, und unterstützt damit seine Identifikation als energetisch tiefsten Zustand des LHC II.

Die Breiten von Nullphonon-Löchern, die in die 650 nm Absorptionsbande gebrannt wurden, entsprechen Energietransferzeiten von 1 ps und  $\sim 240$  fs bei 4.2 K und stimmen somit gut mit zeitaufgelösten Untersuchungen des Chl  $b \rightarrow$  Chl  $a$  Energietransfers bei 12 K überein (Bittner et al., 1995). Chl  $a \rightarrow$  Chl  $a$  Energietransferzeiten in der Größenordnung von 6-10 ps, die aus Lochbreiten innerhalb der 676 nm Absorptionsbande ermittelt wurden, sind ebenfalls konsistent mit Ergebnissen zeitaufgelöster Messungen bei 13 K (Savikhin et al., 1994).

### **9.3 Elektron-Phonon-Wechselwirkung im LHC II**

Die Elektron-Phonon-Wechselwirkung im LHC II wurde sowohl durch spektrales Lochbrennen als auch durch selektive Anregung von Fluoreszenz (Fluorescence Line-Narrowing) bei 4.2 K untersucht. Weiterhin wurden Messungen der Temperaturabhängigkeit der Fluoreszenzspektren von LHC II durchgeführt. Besondere Aufmerksamkeit galt dabei der Vermeidung möglicher systematischer Meßfehler wie der Reabsorption bei Fluoreszenz-Messungen oder von Artefakten durch Lichtstreuung und unerwünschtes Lochbrennen bei selektiver Anregung von Fluoreszenz.

Die Phonon-Seitenbanden, die von Hole-Burning und Fluorescence Line-Narrowing im Spektralbereich des energetisch tiefsten Zustandes erzeugt werden, zeigen offensichtliche Unterschiede in ihrer Linienform. Bei spektralem Lochbrennen beobachtet man ein Pseudo-Phonon-Seitenband bei  $\sim 18$   $\text{cm}^{-1}$  mit einer Breite von  $\sim 25$   $\text{cm}^{-1}$ . Selektiv angeregte Fluoreszenzspektren zeigen dagegen Phonon-Seitenbanden bei  $\sim 24$   $\text{cm}^{-1}$  mit einer Breite von  $\sim 100$   $\text{cm}^{-1}$ . Aus diesem Grund wurden in einer theoretischen Betrachtung die verschiedenen Beiträge zu den Phonon-Seitenbanden bei Hole-Burning und Fluorescence Line-Narrowing separat analysiert. Es konnte gezeigt werden, daß es zu Abweichungen von der Spiegelsymmetrie zwischen Real- und Pseudo-Phonon-Seitenband kommt, wenn die Breite  $\Gamma$  des Ein-Phonon-Profiles in der Größenordnung der inhomogenen Breite  $\Gamma_{\text{inh}}$  des energetisch tiefsten Zustandes von  $80$   $\text{cm}^{-1}$  liegt ( $\Gamma \sim \Gamma_{\text{inh}}$ ). In diesem Fall wird die Linienform des Pseudo-Phonon-Seitenbandes nicht nur durch das Ein-Phonon-Profil, sondern auch wesentlich von der Inhomogenen Verteilungsfunktion (IDF) bestimmt.

Durch einen solchen Effekt kann die Diskrepanz zwischen den Ergebnissen von Hole-Burning und Fluorescence Line-Narrowing für den LHC II erklärt werden. Außerdem kann geschlußfolgert werden, daß der verlässlichste Ansatz zur Untersuchung der Elektron-Phonon-Wechselwirkung aus einer Kombination beider Techniken der hochauflösenden Laserspektroskopie besteht.

Die gleichzeitige theoretische Simulation von Hole-Burning- und Fluorescence Line-Narrowing-Spektren ergibt, daß der energetisch tiefste Zustand durch schwache Elektron-Phonon-Wechselwirkung mit einem Huang-Rhys-Faktor  $S$  von 0.9 und ein breites und stark asymmetrisches Ein-Phonon-Profil mit einem Maximum  $\omega_m$  bei  $15 \text{ cm}^{-1}$  und einer Breite von  $\Gamma = 105 \text{ cm}^{-1}$  gekennzeichnet ist. Die Anpassung des nicht-selektiv angeregten 4.2 K-Fluoreszenzspektrums bestätigt weitgehend die obigen Parameter der Elektron-Phonon-Wechselwirkung sowie die Zuordnung des energetisch tiefsten Zustandes bei  $\sim 680 \text{ nm}$  und eine inhomogene Breite von  $\sim 80 \text{ cm}^{-1}$ .

Ein Ein-Phonon-Profil mit einer Breite von  $\sim 100 \text{ cm}^{-1}$  wurde erstmals experimentell beobachtet und kann nicht mehr als eine „mittlere Phononmode“ verstanden werden, sondern stellt eher eine breite Verteilung von Phononmoden dar. Die Moden, die das Ein-Phonon-Profil bilden, können sehr wahrscheinlich mit delokalisierten Proteinschwingungen identifiziert werden (siehe z.B. Hayes et al., 1988a). In diesem Fall entspricht das Ein-Phonon-Profil im Wesentlichen der Zustandsdichte der Proteinphononen multipliziert mit einem Term, der die Frequenzabhängigkeit der Kopplungsstärke beschreibt. Es ist jedoch möglich, daß sowohl lokalisierte Moden als auch intermolekulare (Chl-Chl) Schwingungen ähnlich der Marker-Mode ( $115 \text{ cm}^{-1}$  -  $135 \text{ cm}^{-1}$ ), die man an bakteriellen Reaktionszentren beobachtet (Johnson und Small, 1989), zur hochenergetischen Flanke des Ein-Phonon-Profiles beitragen. Eine schwach ausgeprägte Schulter, die bei  $\sim 90 \text{ cm}^{-1}$  in selektiv angeregten Fluoreszenzspektren von LHC II auftritt, ist in diesem Zusammenhang von Interesse. Eine eindeutige Identifizierung dieser Mode als Proteinschwingung, lokalisierte oder intermolekulare Schwingung ist auf der Grundlage der vorliegenden Ergebnisse jedoch nicht möglich.

Die niederenergetische Energieniveaustuktur und die zugehörigen Oszillatorstärken sowie die Parameter der Elektron-Phonon-Wechselwirkung aus den zuvor genannten Untersuchungen wurden benutzt, um die Temperaturabhängigkeit der Fluoreszenzspektren von LHC II anzupassen. Bis zu einer Temperatur von 120 K beschreiben die Simulationen die wichtigsten Merkmale wie Verbreiterung und Veränderung der Linienform der Fluoreszenzspektren sowie insbesondere die Blauverschiebung des Fluoreszenzmaximums mit steigender Temperatur. Es ist möglich, daß Konformationsänderungen der Proteinumgebung für die Rotverschiebung des Fluoreszenzmaximums über einer Temperatur von 150 K verantwortlich sind. Die Linienform der hochenergetischen Flanke der temperaturabhängigen Fluoreszenzspektren für  $T \geq 80$  K weist darauf hin, daß die  $Q_y$ -Zustände nach einer Boltzmann-Verteilung besetzt werden.

## References

- Avarmaa, R. A.; Rebane K. K. (1985) *Spectrochim. Acta* 41, 1365.
- Bassi, R. (1990) *Photochem. Photobiol.* 52(6), 1187.
- Bassi, R.; Giuffra, E.; Croce, R.; Dainese, P.; Bergantino, E. (1996) in *Light as an Energy Source and Information Carrier in Plant Physiology* (Edited by R. C. Jennings), pp. 41-63. Plenum Press, New York.
- Berthold, D. A.; Babcock G. T.; Yocum, C. F. (1981) *FEBS Lett.* 134, 231.
- Bittner, T.; Irrgang, K.-D.; Renger, G.; Wasilewski, M. R. (1994) *J. Phys. Chem.* 98, 11821.
- Bittner, T.; Wiederrecht, G. P.; Irrgang, K.-D.; Renger, G.; Wasilewski, M. R. (1995) *Chem. Phys.* 194, 311.
- Chang, H. C.; Jankowiak, R.; Reddy, N. R. S.; Small, G. J. (1995) *Chem. Phys.* 197, 307.
- Connelly, J. P.; Müller, M. G.; Hucke, M.; Gatzen, G.; Mullineaux, C. W.; Ruban, A. V.; Horton, P.; Holzwarth, A. R. (1997) *J. Phys. Chem.* 101, 1902.
- Davis, B. H. (1976) in *Chemistry and Biochemistry of Plant Pigments*, 2<sup>nd</sup> edition, Vol. II (Edited by T. W. Goodwin), pp.38-165. Academic Press, London.
- den Hartog, F. T. H.; Dekker, J. P.; van Grondelle, R.; Völker, S. (1998) *J. Phys. Chem. B* 102, 11007.
- Du, M.; Xie, X.; Mets, L.; Fleming, G. R. (1994) *J. Phys. Chem.* 98, 4736.
- Emerson, R.; Arnold, W. (1932) *J. Gen. Physiol.* 16, 191.
- Förster, Th. (1948) *Annalen der Physik* 2, 55.
- Gillie, J. K.; Small, G. J.; Golbeck J. H. (1989) *J. Phys. Chem.* 93, 1620.
- Giuffra, E.; Zucchelli, G.; Sandona, D.; Croce, R.; Cugini, D.; Garlaschi, F. M.; Bassi, R.; Jennings, R. C. (1997) *Biochemistry* 36, 12984.
- Gorokhovski, A. A.; Kaarli, R. K.; Rebane, L. A. (1974) *JETP Lett.* 20, 216.
- Gradinaru, C. C.; Özdemir, S.; Gülen, D.; van Stokkum, I. H. M.; van Grondelle,

- R.; van Amerongen, H. (1998a) *Biophys. J.* 75, 3064.
- Gradinaru, C. C.; Pascal, A.; van Mourik, F.; Robert, B.; Horton, P.; van Grondelle, R.; van Amerongen, H. (1998b) *Biochemistry* 37, 1143.
- Haarer, D. (1989) in *Persistent Spectral Hole-Burning: Science and Applications* (Edited by W. Moerner), pp.79-126. Springer-Verlag, Berlin / Heidelberg.
- Hayes, J. M.; Small G. J. (1978) *Chem. Phys.* 27, 151.
- Hayes, J. M.; Jankowiak, R.; Small, G. J. (1988a) in *Persistent Spectral Hole-Burning: Science and Applications* (Edited by W. Moerner), pp.153-202. Springer-Verlag, Berlin/ Heidelberg.
- Hayes, J. M.; Gillie, J. K.; Tang, D.; Small, G. J. (1988b) *Biochim. Biophys. Acta* 932, 287.
- Hayes, J.M.; Lyle, P.A.; Small, G.J. (1994) *J. Phys. Chem.* 98, 7337.
- Hemelrijk, P. W.; Kwa, S. L. S.; van Grondelle, R.; Dekker, J. P. (1991) *Biochim. Biophys. Acta* 1098, 159.
- Henrysson, T.; Schröder, W. P.; Spangfort, M.; Åkerlund, H.-E. (1989) *Biochim. Biophys. Acta* 977, 301.
- Heukeshoven, J.; Dernick, R. (1985) *Electrophoresis* 6, 103.
- Irrgang, K.-D.; Boekema, E.J.; Vater, J.; Renger, G. (1988) *Eur. J. Biochem.* 178, 209.
- Irrgang, K.-D. (1999) in *Concepts in Photobiology and Photomorphogenesis* (Edited by G. S. Singhal, G. Renger, K. Sopory, K.-D. Irrgang, Govindjee), pp. 52-90. Narosa Publishing House, New Delhi, India.
- Jankowiak, R.; Small, G. J. (1991) *Chem. Res. Toxicol.* 4, 256.
- Jankowiak, R.; Hayes, J. M.; Small, G. J. (1993) *Chem. Rev.* 93, 1471.
- Jansson, S. (1994) *Biochim. Biophys. Acta* 1184, 1.
- Jelezko, F.; personal communication
- Johnson, S. G.; Tang, D.; Jankowiak, R.; Hayes, J. M.; Small G. J.; Tiede, D. M. (1989) *J. Phys. Chem.* 93, 5953.
- Johnson, S. G.; Small, G. J. (1991) *J. Phys. Chem.* 95, 471.
- Kehrberg, G.; Voigt, J.; Schrötter, T.; Renger, G. (1995) *Biochim. Biophys. Acta* 1231, 147.

## References

---

- Kenney, M. J.; Jankowiak, R.; Small, G. J. (1990) Chem. Phys. 146, 47.
- Kharlamov, B. M.; Personov, R. I.; Bykovskaya, L. A. (1974) Opt. Comm. 12, 191.
- Kikas, J. (1978) Chem. Phys. Lett. 57, 511.
- Kim, W.-H.; Reinot, T.; Hayes, J. M.; Small, G. J. (1995) J. Phys. Chem. 99, 7300.
- Kleima, F. J.; Gradinaru, C. C.; Calkoen, F.; van Stokkum, I. H. M.; van Grondelle, R. Biochemistry 1997, 36, 15262.
- Kühlbrandt, W.; Wang, D. N.; Fujiyoshi, Y. (1994) Nature 367, 614.
- Kühn, O.; Renger, T.; May, V.; Voigt, J.; Pullerits, T.; Sundström, V. (1997) Trends in Photochem. Photobiol. 4, 213.
- Kwa, S. L. S.; Völker, S.; Tilly, N. T.; van Grondelle, R.; Dekker, J. P. (1993) Photochem. Photobiol. 59, 219.
- Laemmlli, U. K. (1970) Nature 227, 680.
- Lee, I.; Hayes, J. M.; Small, G. J. (1989) J. Chem. Phys. 91(6), 3463.
- Lichtenthaler, H.K. (1987) Methods Enzymol. 148, 350.
- Louwe, R. J. W.; Aartsma, T. J. (1997) J. Phys. Chem. B 101, 7221.
- Lyle, P. A.; Kolaczowski, S. V.; Small, G. J. (1993) J. Phys. Chem. 97, 6924.
- Mc Colgin, W. C. (1975) Ph.D. Thesis, The University of Rochester.
- Osadko, I. S. (1983) in *Spectroscopy and Excitation Dynamics of Condensed Molecular Systems* (Edited by M. Agranovich and R. M. Hochstrasser) , pp. 437-512. Elsevier / North-Holland, Amsterdam, The Netherlands.
- Pascal, A.; Gradinaru, C.; Wacker, U.; Peterman, E.; Calkoen, F.; Irrgang, K.-D.; Horton, P.; Renger, G.; van Grondelle, R.; Robert, B.; van Amerongen, H. (1999) Eur. J. Biochem. 262, 817.
- Pascal, A.; Wacker, U.; Irrgang, K.-D.; Horton, P.; Renger, G.; Robert, B., submitted to Eur. J. Biochem.
- Paulsen, H. (1995) Photochem. Photobiol. 62, 367.
- Pearlstein, R. M. (1991) in *Chlorophylls* (Edited by H. Scheer) , pp. 1047-1078. CRC Press, Boca Raton.

- Personov, R. I.; Alshits, E. I.; Bykovskaya, L. A.; Kharlamov, B. M. (1973) JETP 65, 1825.
- Personov, R. I. (1983) in *Spectroscopy and Excitation Dynamics of Condensed Molecular Systems* (Edited by M. Agranovich and R. M. Hochstrasser) , pp. 555-620. Elsevier / North-Holland, Amsterdam, The Netherlands.
- Peterman, E. J. G.; Hobe, S.; Calkoen, F.; van Grondelle, R.; Paulsen, H.; van Amerongen, H. (1996) Biochim. Biophys. Acta 1273, 171.
- Peterman, E. J. G.; Pullerits, T.; van Grondelle, R.; van Amerongen, H. (1997) J. Phys. Chem. B. 101, 4448.
- Peterman, E. J. G.; van Amerongen, H.; van Grondelle, R.; Dekker, J. P. (1998) Proc. Natl. Acad. Sci. USA 95, 6128.
- Pieper (1996) Thesis, Humboldt-University, Berlin.
- Pieper, J.; Irrgang, K.-D.; Rätsep, M.; Schrötter, T.; Small, G. J.; Voigt, J.; Renger, G. (1997) Proceedings of the International Conference on Ultrafast Processes in Spectroscopy (UPS 97), Tartu, Estonia.
- Pieper, J.; Rätsep, M.; Jankowiak, R.; Irrgang, K.-D.; Voigt, J.; Renger, G.; Small, G. J. (1999a), Journal of Physical Chemistry A 103, 2412.
- Pieper, J.; Irrgang, K.-D.; Rätsep, M.; Jankowiak, R.; Schrötter, T.; Small, G. J.; Voigt, J.; Renger, G. (1999b), Journal of Physical Chemistry A 103, 2422.
- Pieper, J.; Irrgang, K.-D.; Rätsep, M.; Voigt, J.; Renger, G.; Small, G. J. (2000). Photochem. Photobiol. 71(5), 574.
- Porra, R. G.; Thompson, W. A.; Kriedemann, P. E. (1989) Biochim. Biophys. Acta 975, 384.
- Rätsep, M.; Blankenship, R. E.; Small, G. J. (1999) J. Phys. Chem. B 103, 5736.
- Rebane K. K. (1970) *Impurity Spectra of Solids*, Plenum Press, New York.
- Reddy, N. R. S.; Lyle, P. A.; Small, G. J. (1992) Photosyn. Res. 31, 167.
- Reddy, N. R. S.; Kolaczowski, S. V.; Small, G. J. (1993) J. Phys. Chem. 97, 6934.
- Reddy, N. R. S.; van Amerongen, H.; Kwa, S. L. S.; van Grondelle, R.; Small,

## **References**

---

- G. J. (1994) *J. Phys. Chem.* 98, 4729.
- Reddy, N. R. S.; Wu, H.-M.; Jankowiak, R.; Picorel, R.; Cogdell, R. J.; Small, G. J. (1996) *Photosyn. Res.* 48, 277.
- Renger, G. (1992) in *Topics in Photosynthesis* (Edited by J. Barber), pp. 45-99. Elsevier: Amsterdam.
- Renger, G. (1999) in *Concepts in Photobiology and Photomorphogenesis* (Edited by G. S. Singhal, G. Renger, K. Sopory, K.-D. Irrgang, Govindjee), pp. 52-90. Narosa Publishing House, New Delhi, India.
- Renger, T. (1995) Thesis, Humboldt-University, Berlin.
- Renger, T.; Voigt, J.; May, V.; Kühn, O. (1996) *J. Phys. Chem. B* 100, 15654.
- Renger, T.; May, V. (2000) *Phys. Rev. Lett.*, in press
- Rogl, H.; Kühlbrandt, W. (1999) *Biochemistry* 38, 16214.
- Ruban, A. V.; Young, A. J.; Horton, P. (1996) *Biochemistry* 35, 674.
- Savikhin, S.; van Amerongen, H.; Kwa, S. L. S.; van Grondelle, R.; Struve, W. S. (1994) *Biophys. J.* 66, 1597.
- Schödel, R.; Hillmann, F.; Schrötter, T.; Voigt, J.; Irrgang, K.-D.; Renger, G. (1996) *Biophys. J.* 71, 3370.
- Schrötter, T.; Voigt, J.; Kehrberg, G. (1994) *Photosynthetica* 30 (4), 567.
- Seydack, M.; Redlin, H.; Voigt, J. (1995) in *Photosynthesis: from light to biosphere*, Proc. Xth Intern. Photosynthesis Conf., Vol.I (Edited by P. Mathis), p. 335. Kluwer Academic Publishers, Dordrecht.
- Shu, L.; Small, G.J. (1990) *J. Opt. Soc. Am. B* 9, 724.
- Siefermann-Harms, D. (1987) *Physiol. Plantarum* 69, 561.
- Towbin, H.; Staehelin, T.; Gordon, J. (1979) *Proc. Natl. Acad. Sci. USA* 76, 4350.
- Trinkunas, G.; Conelly, J. P.; Müller, M. G.; Valkunas, L.; Holzwarth, A. R. (1997) *J. Phys. Chem. B*, 101, 7313.
- Van Grondelle, R.; Dekker, J. P.; Gillbro, T.; Sundstrom, V. (1994) *Biochim. Biophys. Acta* 1187, 1.
- Vasil'ev, S.; Irrgang, K.-D.; Schrötter, T.; Bergmann, A.; Eichler, H.-J.; Renger, G. (1997a) *Biochemistry* 36, 7503.

- Vasil'ev, S.; Schrötter, T.; Bergmann, A.; Irrgang, K.-D.; Eichler, H.-J.; Renger, G. (1997b) *Photosynthetica*, 33, 553.
- Visser, H. M.; Kleima, F. J.; van Stokkum, I. H. M.; van Grondelle, R.; van Amerongen, H. (1996) *Chem. Phys.* 210, 297.
- Voigt, J.; Macy, K.; Schrötter, T. (1994) *Photosynthetica* 30(4), 567.
- Voigt, J.; Renger, T.; Schödel, R.; Schrötter, T.; Pieper, J.; Redlin, H. (1996) *Phys. Stat. Sol. (b)* 194, 333.
- Voigt, J.; Schrötter, T. (1999) *Z. f. Physikalische Chemie Z* 11, 181.
- Völker, M.; Ono, T.; Inoue, Y.; Renger, G. (1985) *Biochim. Biophys. Acta* 806, 25.
- Völker, S. (1989) in *Relaxation Processes in Molecular Excited States* (Edited by J. Fünfschilling), pp.113-242. Kluwer Academic Publishers, Dordrecht.
- Wellburn, A. R.; Lichtenthaler, H. (1984) in *Advances in Photosynthesis Research*, Vol. II (Edited by C. Sybesma), pp.9-12. Martinus Nijhoff Publ., The Hague, The Netherlands.
- Wu, H.-M.; Rätsep, M.; Lee, I.-J.; Cogdell, R. J.; Small, G. J. (1997) *J. Phys. Chem. B* 101, 7654.
- Wu, H.-M.; Small, G. J. (1998) *J. Phys. Chem. B* 102, 888.
- Wu, H.-M.; Rätsep, M.; Jankowiak, R.; Cogdell, R. J.; Small, G. J. (1998) *J. Phys. Chem. B* 102, 4023.
- Zucchelli, G.; Dainese, P.; Jennings, R. C.; Breton, J.; Garlaschi, F. M.; Bassi, R. (1994) *Biochemistry* 33, 8982.

## ***Publications***

1. Voigt, J.; Renger, T.; Schödel, R.; Schrötter, T.; Pieper, J.; Redlin, H. (1996) Excitonic Effects in the Light-Harvesting Chl *a/b*-Protein Complex of Higher Plants, *Phys. Stat. Sol. (b)* 194, 333.
2. Pieper, J.; Irrgang, K.-D.; Rätsep, M.; Schrötter, T.; Small, G. J.; Voigt, J.; Renger, G. (1997) Hole Burning Study of Solubilized and Aggregated LHC II Complexes, *Proceedings of the International Conference on Ultrafast Processes in Spectroscopy (UPS 97)*, Tartu, Estonia.
3. Pieper, J.; Rätsep, M.; Jankowiak, R.; Irrgang, K.-D.; Voigt, J.; Renger, G.; Small, G. J. (1999)  $Q_y$ -Level Structure and Dynamics of Solubilized Light-Harvesting Complex II of Green Plants: Pressure and Hole Burning Studies, *Journal of Physical Chemistry A* 103, 2412.
4. Pieper, J.; Irrgang, K.-D.; Rätsep, M.; Jankowiak, R.; Schrötter, T.; Small, G. J.; Voigt, J.; Renger, G. (1999) Effects of Aggregation on Trimeric Light-Harvesting Complex II of Green Plants: A Hole Burning Study, *Journal of Physical Chemistry A* 103, 2422.
5. Pieper, J.; Voigt, J.; Small, G. J. (1999) Chlorophyll *a* Franck-Condon Factors and Excitation Energy Transfer, *Journal of Physical Chemistry B* 103, 2319.
6. Pieper, J.; Voigt, J.; Renger, G.; Small, G. J. (1999) Analysis of Phonon Structure in Line-Narrowed Optical Spectra, *Chemical Physics Letters* 310, 296.
7. Pieper, J.; Irrgang, K.-D.; Rätsep, M.; Voigt, J.; Renger, G.; Small, G. J. (2000) Assignment of the Lowest  $Q_y$ -State and Spectral Dynamics of the Chlorophyll *a/b* Antenna Complex CP29 of Green Plants: A Hole-Burning Study, *Photochem. Photobiol.* 71(5), 574.
8. Pieper, J.; Schödel, R.; Voigt, J.; Irrgang, K.-D.; Renger, G. Electron-Phonon Coupling in Trimeric Light-Harvesting Complex II of Green Plants: Line-Narrowed and Temperature-Dependent Fluorescence Spectra, in preparation.

## Lebenslauf

Jörg Pieper, geboren am 12.10.1968 in Zossen (Land Brandenburg)

Eltern: Vater: Wolfgang Pieper, geboren am 05.12.38

Mutter: Inge Pieper (geborene Görmer), geboren am  
03.10.39

1975 - 1985 Besuch der Allgemeinbildenden Oberschule in  
Rangsdorf

1985 - 1987 Besuch der Erweiterten Oberschule in Ludwigsfelde

11.1987 - 01.1990 Wehrdienst

02.1990 - 08.1990 EDV-Bediener im Automobilwerk Ludwigsfelde

09.1990 - 06.1996 Physikstudium an der Humboldt-Universität zu Berlin

04.1995 - 06.1996 Diplomarbeit (Betreuer: Prof. Dr. J. Voigt) zum Thema:

*„Untersuchungen zur Exziton-Phonon-Wechselwirkung  
am lichtsammelnden Komplex II des Photosynthese-  
apparates höherer Pflanzen“*

09.1996 - 12.1996 Iowa State University, Ames (USA)

01.1997 Beginn der Promotion (Betreuer: Prof. Dr. J. Voigt)

01.1997 - 03.1998 Humboldt-Universität zu Berlin

04.1998 - 03.1999 Iowa State University in Ames (USA)

seit 04.1999 Humboldt-Universität zu Berlin

Berlin, den 13. Juli 2000

Jörg Pieper



## **Danksagung**

Zu besonderem Dank bin ich meinem Betreuer Prof. Dr. Joachim Voigt verpflichtet, der mir ermöglichte, die vorliegende Dissertation in der Arbeitsgruppe „Molekulare Biophysik und Spektroskopie“ anzufertigen. Er hat meine Arbeit in vielen fachlichen Diskussionen stimuliert, aber auch den nötigen Freiraum für die Entwicklung eigener Ideen zugelassen. Weiterhin gilt mein Dank allen Mitgliedern der Arbeitsgruppe „Molekulare Biophysik und Spektroskopie“, insbesondere Herrn Dr. René Schödel, für die vielfältige Unterstützung beim Zustandekommen meiner Arbeit.

Einen wesentlichen Anteil am Gelingen meiner Arbeit hatte die konstruktive Zusammenarbeit mit Prof. Dr. Gernot Renger und Dr. Klaus Irrgang vom Max-Volmer-Institut der Technischen Universität Berlin, die sich keineswegs nur auf die Bereitstellung der für meine Experimente wichtigen Proben beschränkte. Vielmehr möchte ich mich auch für die anregenden Diskussionen und die vielfältige Unterstützung bedanken.

Einen bedeutenden Teil meiner Ergebnisse konnte ich bei einem Forschungsaufenthalt an der Iowa State University in Ames (Iowa, USA) erzielen. Ich danke hier vor allem Prof. Gerald J. Small für die Einladung zur Mitarbeit in seiner Arbeitsgruppe. Seine langjährige Erfahrung auf dem Gebiet der hochauflösenden Laserspektroskopie, seine Ideen, aber auch seine Bereitschaft zur Auseinandersetzung mit neuartigen Problemen waren von unschätzbarem Wert für den Erfolg meiner Arbeit. Die erfolgreiche Zusammenarbeit mit der Arbeitsgruppe von Prof. Small wäre jedoch undenkbar ohne die Unterstützung von Dr. Ryszard Jankowiak, der den Aufenthalt in Ames für mich vorbereitete und stets offen für Fragen oder Diskussionen war.

Weiterhin danke ich allen Mitgliedern der Arbeitsgruppe von Prof. Small, vor allem aber Dr. Margus Rätsep, Dr. Hsing-Mei Wu, Dr. Tonu Reinot und Kenneth Roberts, für ihre vielfältige Hilfe beim Gelingen meiner Experimente. Ich danke außerdem Dr. John M. Hayes für seine stete Bereitschaft, mir bei Problemen bei der theoretischen Beschreibung meiner Ergebnisse weiterzuhelfen.

Meine Arbeit wurde durch Stipendien nach dem Nachwuchsförderungsgesetz (NaFöG), des Deutschen Akademischen Austauschdienstes (DAAD) und der FAZIT-Stiftung Frankfurt/Main gefördert. Weiterhin danke ich der Deutschen Forschungsgemeinschaft (DFG) für ihre finanzielle Unterstützung.

Bei meinem Forschungsaufenthalt in Ames wurde ich außerdem vom International Institute of Theoretical and Applied Physics der Iowa State University unterstützt. Ich danke hier vor allem dem Direktor Dr. James Vary für die Einladung nach Ames und der Besuchskordinatorin Frau Rosslyn Scheideman, durch deren Hilfe viele organisatorische Probleme gelöst werden konnten.



## **Erklärung**

Hiermit erkläre ich, die Dissertation selbständig und ohne unerlaubte Hilfe angefertigt zu haben.

Ich habe mich anderwärts nicht um einen Doktorgrad beworben und besitze einen entsprechenden Doktorgrad nicht.

Ich erkläre die Kenntnisnahme der dem Verfahren zugrunde liegenden Promotionsordnung der Mathematisch-Naturwissenschaftlichen Fakultät I der Humboldt-Universität zu Berlin.

Berlin, den 13. Juli 2000

Jörg Pieper